The Dissertation Committee for Daniel Robert Moser
certifies that this is the approved version of the following dissertation:

Multi-Scale Computational Modeling of Selective Laser Melting for Process Improvements

Committee:

Michael Cullinan, Supervisor

Jayathi Murthy, Co-Supervisor

Joseph Beaman

David Bourell

Carolyn Seepersad

Sreekanth Pannala

Multi-Scale Computational Modeling of Selective Laser Melting for Process Improvements

by

Daniel Robert Moser, B.S.E.

Dissertation

Presented to the Faculty of the Graduate School of

The University of Texas at Austin

in Partial Fulfillment

of the Requirements

for the Degree of

Doctor of Philosophy

The University of Texas at Austin

August 2017

Multi-Scale Computational Modeling of Selective Laser Melting for Process Improvements

by

Daniel Robert Moser, Ph.D.
The University of Texas at Austin, 2017
SUPERVISORS: Michael Cullinan, Jayathi Murthy

Selective Laser Melting (SLM) is an additive manufacturing technique able to rapidly create parts directly from a CAD model using a laser to selectively fuse successive layers of powder. However, defects can arise in SLM parts due to incomplete fusion of the powder layers or thermal stresses introduced by large temperature gradients during the part build. Accurate models of the SLM process have the potential to reduce testing and experimentation required when using new materials or part designs. By predicting part properties directly from the process inputs, problems such as incomplete melting or thermal stresses introduced by large temperature gradients can be identified and corrected.

Simulating the complete build of an SLM part is challenging, however, due to the difference in scale between the size of particles being melted and the size of the part being produced. Because of this, bed-scale continuum models, in which the powder bed is represented as a continuous medium, are typically used as the computational cost of resolving individual particles in a full-scale

bed is prohibitive. However, continuum models require as inputs volume-averaged, effective properties of the powder which are often unknown and difficult to measure or obtain by experimental means. This thesis develops a multi-scale modeling approach in which particle-scale models, where individual particles are resolved in a small, representative, domain, are used to predict the effective optical properties, thermal conductivity, and melt behavior of a powder which are then used in a part-scale continuum model to predict temperature history, melt percentage, and thermal stresses in an SLM build.

First, a transient, three-dimensional, finite volume thermal model is developed and implemented in ANSYS Fluent. A domain of cells representing multiple layers of a build is initialized, some with the properties of air and some with the properties of powder, depending on cell location. A Gaussian heat source representing the laser is applied to the top layer of powder cells. The center of the Gaussian is varied with time along an established path to simulate the motion of the laser along the powder bed. The three-dimensional unsteady heat equation is solved to produce a temperature profile of the powder bed. When the laser completes a full scan of the powder layer, the air cells directly above the powder layer are re-initialized as powder cells and re-set to an initial temperature, representing the addition of a new powder layer. The process is repeated for each new layer. Temperature history results from the model are validated against experimental data available in the literature and good agreement is obtained. However, uncertainty quantification reveals large uncertainties in the temperature prediction due to the uncertainty in the effective

properties of the powder needed as model inputs. Effective thermal conductivity, absorptivity and extinction coefficient, and specific heat (incorporating latent heat due to melting) are found to be the largest sources of uncertainty and are therefore investigated further using detailed, particle-scale modeling.

Particle-scale modeling is accomplished using the Discrete Element Method (DEM). The DEM represents particles in a domain as spherical control volumes which interact with each other via constitutive models for contact mechanics and heat transfer. The effective absorptivity and extinction coefficient of an SLM powder bed is calculated using a Monte Carlo ray tracing algorithm in conjunction with the DEM. Random, loose packed, particle bed structures are generated using the DEM and rays representing laser irradiation are traced through the structures, tracking their interactions with particles. By examining how energy is deposited in the bed, effective absorptivity and extinction coefficients are calculated. Results are compared against previous computational and experimental measurements for free, monodisperse, and deep powder beds and good agreement is obtained. The effects of various parameters relevant to SLM, such as laser spots size, particle emissivity, bed depth, and polydispersity on extinction and absorption coefficients are explored computationally and quantified. Bed depth and particle emissivity are found to have the most significant effect and thus correlations along with uncertainties are developed for these parameters to allow the effective absorptivity and extinction coefficient to be accurately set in SLM bed-scale models.

The effective thermal conductivity of a powder bed is calculated by

generating random particle packing structures using the DEM and calculating the heat transfer between the particles. A particle-particle contact conduction model, a particle-fluid-particle conduction model, and a view factor radiation model using ray-tracing for calculation of view factors and assuming optically thick particles are used. A non-linear solver is used to solve for the particle temperatures that drive the net heat transfer to zero for a steady state solution. The effective thermal conductivity is then calculated from the steady state temperature distribution. Results are compared against previously published experimental measurements for powder beds and good agreement is obtained. The impacts of very high temperatures, finite bed depth, consolidation, Young's modulus, emissivity, gas conductivity, and polydispersity on effective thermal conductivity are investigated. Bed temperature and gas conductivity are found to have the largest effect on thermal conductivity and thus an empirical relation for the effective conductivity as a function of these parameters is developed. Uncertainties quantification is performed to estimate uncertainty in thermal conductivity from all uncertain inputs, thus allowing thermal conductivity to be accurately set in SLM bed-scale models.

The melt fraction-temperature relationship for a powder undergoing laser melting is calculated using a hybrid continuum-discrete methodology to model the powder melting process. The DEM is used to generate random packing structures of spherical particles. These structures are then placed on top of a background mesh. The radiation transport, heat transfer, and fluid flow equations are solved for on the mesh to simulate the melting behavior of

the powder. The resulting total melt pool depth and width is calculated and results compared against previously published experimental results for various materials. Experimental results are shown to fall within a 90% confidence interval of the simulation results given uncertainty estimates. Relations, with uncertainty, are developed for the average melt fraction of the powder as a function of the average temperature of the powder. The utility of these melt fractiontemperature relations is established by using them to model phase change using a continuum bed-scale model of the SLM process. It is shown that the use of the developed relations captures partial melt behavior of the powder that a simple melting model cannot. Furthermore, the model accounts for both uncertainty in material properties as well as packing structure in the final melt fraction-temperature relationship, unlike simple melting models.

Finally, a transient, three-dimensional, bed-scale coupled finite volume thermal-mechanical model is developed using the particle-scale sub-models and implemented in OpenFOAM. As with the ANSYS Fluent model, the laser is represented as a time-varying Gaussian heat source applied to the top layer of powder cells. The unsteady heat equation is solved to produce a temperature profile of the powder bed. This temperature field is then used to generate a thermal stress term in an elastic-plastic model. The elastic-plastic model uses an iterative linear elastic relationship with a plastic corrector based on the von Mises yield criterion to calculate the stress and displacement field in the domain at each time step. Once the laser source completes its scan pattern, the temperature, stress and displacement fields are evolved further without

a heat source term until the domain is completely cooled in order to predict residual stress development.

It is found that the convection coefficient of the thermal boundary condition imposed on the bottom of the domain has a significant impact on the resulting residual stress in a part. As this boundary condition depends in part on the contact resistance between a part being built and the metal base plate on which it is being built on, which is unknown, no simple mechanism exists with which to set this simulation parameter. Therefore, a parameter sweep is conducted and the convection coefficient calibrated based on the results. Uncertainty quantification is performed based on the variability of the powder bed porosity and results compared to experimental data for a single layer build. Although porosity variability is able to account for some of the differences seen between the predicted and experimental values, some experimental results are found to lie outside the uncertainty bounds. This indicates that a more precise calibration technique for the convection coefficient is needed. However, it is seen that the expected variation in porosity results in large uncertainties in residual stress, limiting the precision in such predictions.

The multi-scale modeling framework developed by this thesis presents a novel way of using detailed, particle-scale simulations to predict effective properties for bed-scale simulations of powder-based additive manufacturing processes. Additionally, rigorous uncertainty quantification is applied to all predictions, a practice that has generally been lacking in prior works simulating additive manufacturing. Importantly, the framework developed here

introduces a mechanism by which uncertainties can be propagated between modeling scales. When particle-scales models are used to predict effective properties with uncertainty, the resulting probability distributions can then be used as inputs to uncertainty quantification routines at the bed-scale. This thesis provides already developed correlations with the necessary uncertainty estimates for the effective thermal conductivity, absorptivity and extinction coefficient of metal powders and the temperature-melt fraction relationship for 316 stainless steel powder. Finally, variation in powder packing structure is identified as a significant source of uncertainty in all models, a factor that is often overlooked in existing work.

Much works still remains to be done in the modeling of powder-based additive manufacturing processes. As powder packing structure has been identified as a significant source of uncertainty, particle-scale modeling of powder deposition processes could provide further insight into how to characterize powder bed structures and possibly reduce the modeling uncertainty inherent in them. Computational time remains a challenge as well. The builds modeled in this work, even at the bed scale, are small compared to parts that are typically built using these processes, but still consume significant computational resources. Improving model performance and developing fast, reduced-order models will be key to simulating larger part builds and incorporating models into control and optimization routines. Also, phenomena such as microstructure formation, which can influence part material properties, have not been considered as part of this work but are important considerations and op-

portunities for future modeling work in order to fully understand the possible variability in these processes.

Table of Contents

List of Tables

List of Figures

Chapter 1

Introduction

1.1 Background

Free-form fabrication techniques reduce the cost of creating prototypes or small batch parts by producing parts directly from CAD models without part-specific tooling. Selective Laser Melting (SLM) is a promising free-form fabrication process as it works with a wide variety of materials, particularly metals. SLM produces a solid object by selectively fusing successive layers of powder. A thin layer of powder is deposited on top of a piston. The surface of the powder is then scanned by a laser with a modulated power, fusing the powder to itself and the layer below where the cross-section is intended to be solid and leaving it loose where it is not. When the scan of the layer is complete, the piston holding the part is lowered, a new layer of powder is deposited on top and the process repeats. A schematic of the process is shown in Figure 1.1. After the build is complete, the loose powder is removed, leaving the final part [42].

SLM, along with other additive manufacturing technologies, have led to the creation of an entirely new manufacturing space that stands to have enormous impact across a variety of industries. As SLM can produce metal

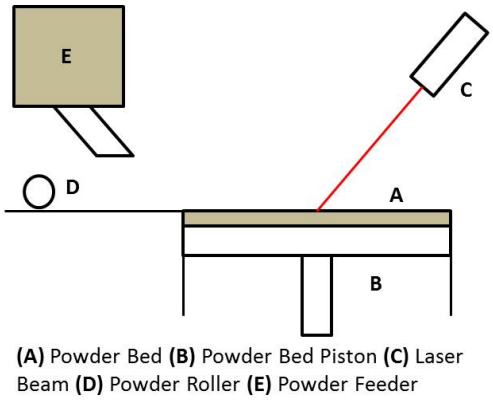

Figure 1.1: Illustration of SLM Process

parts directly from a CAD model, manufacturing setup costs are reduced, bringing down the cost of small-batch manufacturing for everything from replacement parts for military aircraft to components for rocket engines. Similarly, increased customization is possible for things like medical implants and prosthetics. SLM is also able to produce geometries which conventional manufacturing techniques cannot, enabling the fabrication of everything from more effective heat exchangers for turbine blade cooling to more lightweight aircraft parts [56].

Despite its current wide use, SLM is a process still in its infancy and suffers from a number of limitations. Control of SLM processing parameters, such as laser power, laser speed, scanning pattern, and powder pre-heating temperature is critical for the creation of a high-quality part. Improper control of these parameters can lead to geometric errors, incomplete melting, where layers are not melted all the way through and do not adequately fuse to the layer below, and over melting, where material is vaporized by the laser, creating

pores. Furthermore, large thermal stresses can cause deformation, reduce part performance, and even result in build failure [36]. However, it is difficult to determine what the optimum processing parameters should be for a given part geometry and material. Thus, experimentation is often required when using new materials or geometries in order to determine the parameters needed to produce an acceptable part (eg. [44]).

Also, no technique currently exists to predict whether or not produced parts will meet imposed quality standards. Variability in geometric accuracy, material properties, and defect formation is often observed in parts produced with the same processing parameters between machines, between builds on the same machine, and even between different regions of a powder bed in the same build. This lack of consistency creates a challenge for the adoption of SLM in critical applications such as medical devices or aerospace parts [15, 56]. Builds must often be individually validated, and certification is frequently done on a per-machine or per-build basis as opposed to per-process [56].

Comprehensive and accurate computational modeling of the SLM process has the potential to reduce the amount of manual experimentation and testing required when producing and certifying a part. Models could theoretically be used to determine optimum processing parameters for a new material or geometry, predict the quality of a part produced using a given set of parameters, and to inform control schemes [29].

1.2 Bed-Scale Thermal Modeling of SLM

Numerous bed-scale models of laser-powder additive manufacturing processes have already been developed [7, 11, 23, 30, 42, 45, 51, 58, 61, 66, 77]. These models approximate a powder bed as a continuous medium. The heat equation, along with a laser source term, is discretized across the domain using a finite element or finite volume mesh and the resulting set of algebraic equations solved to yield a prediction of the temperature and, in some cases, stress distribution in the domain.

The first models developed of the laser melting process were 1D. Nelson et al. [42] developed and implemented a 1D, unsteady model considering only the variation of temperature with depth into the bed. When compared to experimental data, the model was able to predict the general trend of melt depth as a function of laser beam radius. While simple and easy to implement, the 1D model is of limited utility as it cannot account for spatial variations along the surface of the powder bed such as already consolidated material or previously heated powder.

More recently, three dimensional models of the SLM process have been introduced. Sun et al. [58] used a 3D finite element model implemented in ANSYS to predict the temperature profile and melting of an aluminum alloy. The 3D model is capable of predicting interactions with previously scanned areas of the bed as well as the building of complex geometries. However, the model relies upon a correlation for the effective thermal conductivity of the powder whose uncertainty is not quantified, and does not consider laser penetration

into the powder bed. Additionally, although experiments are conducted to verify the model results, no systematic uncertainty quantification is performed, meaning the results can only be said to have qualitative agreement.

Various improvements to 3D models have been proposed. For example, Zeng et al. [77] used an adaptive meshing technique to resolve the thermal solution in greater detail near the laser than in the rest of the powder bed in order to reduce computational time. While they were able to reduce computational time and results were consistent with those predicted using a uniformly refined mesh, no uncertainty quantification or comparison to experimental results was performed.

All of these models suffer from two shortcomings. First, bed-scale continuum models use volume averaged, bulk, material properties to represent the behavior of the powder in the domain, thus avoiding the need to resolve every powder particle individually [28]. This approach is advantageous as it saves computational expense over resolving every individual particle but current models have relied upon simple approximations to provide these bulk properties [23], and the uncertainty introduced by these approximations is difficult to quantify.

Second, uncertainty quantification is not performed, meaning that model predictions do not have uncertainty bounds attached to them indicating how precise the prediction is estimated to be. Thus, even when simulations are performed alongside experiments for validation purposes (e.g. [23]), only qualitative comparison to experimental results is possible. Without an estimate of the

probability distribution of a model prediction, it is impossible to say whether an experimental results is consistent with the prediction in any meaningful way. Not only has a lack of uncertainty quantification prevented systematic model validation, but it also makes predictions of process variability impossible, a capability that is needed in order for produced parts to be certified to a given specification.

1.3 Particle Scale Modeling of SLM

More recently, particle-scale modeling of the SLM process has become more common [20, 27, 28, 31] Unlike bed-scale models, particle-scale models resolve individual particles in the domain. While using a particle-scale model to simulate a full-scale part build would be too computationally expensive, particle-scale models of small portions of SLM powder beds have had success in qualitatively explaining some phenomena occurring at the particle level [28].

Gurtler et al. [20] developed a volume of fluid (VOF) based model of the laser melting processing including melt flow and solidification. However, only regular, monodisperse packing structures were considered. Additionally, no uncertainty quantification was performed, meaning only qualitative correlation with experimental data was possible.

Khairallah et al. [28] developed a detailed model of the laser-powder melting process including complex physics such as recoil pressure and Marangoni convection. A sensitivity analysis was performed, but only a single parameter, absorptivity, was considered. Model predictions for melt depth were shown to

be consistent with experiments for the sensitivities considered. The model was successful in explaining the phenomena of material spatter and denudation.

However, aside from this single-parameter sensitivity analysis [28], systematic uncertainty quantification has been absent from these detailed models as well, making quantitative validation impossible. Additionally, these models currently present no clear mechanism by which their results could be used to inform a prediction about a domain on the order of a full-scale part.

1.4 Bed-Scale Stress Modeling of SLM

Models for predicting residual stress have begun to be reported in the literature with varying degrees of complexity and resolution. Mercelis and Kruth [36] proposed a simple analytical model for predicting the residual stress in rectangular geometries.

Zaeh and Branner [76] developed a computational model for predicting residual stress relying on effective heat sources, in which the detailed motion of the laser is neglected and replaced with a lower-resolution effective heat source approximating it in order to achieve faster computational time.

Li et al. [32] developed a multi-scale approach in which a detailed stress simulation, resolving the laser motion fully on a small domain, was performed and used to compute an effective stress profile for use in predicting the residual stress in a full-size part.

Hodge et al. [23] developed a coupled thermal-mechanical model for the

prediction of temperature and stress profiles during an SLM build with fully resolved laser motion.

However, none of these works presented a quantitative uncertainty analysis and made only qualitative comparisons to experimental data.

1.5 Uncertainty Quantification

A focus of this thesis is uncertainty quantification. Many parameters required as inputs to SLM process models are not known precisely and thus have an uncertainty attached to them. For example, the emissivity of a metal can vary greatly depending on surface properties such as polish and oxidation that cannot be easily controlled. Thus, there is generally a known range of emissivity values for a given material, not a single value. As emissivity greatly effects how much laser energy is absorbed and reflected by a powder bed, this can translate into large uncertainties in predicted temperature profiles across the emissivity range. Other input parameters, such as laser powder, laser spot size, specific heat capacity, and porosity are similarly only known imprecisely and thus can lead to an uncertainty in the outputs. Additionally, SLM powder beds are generally only 1-3 particle diameters thick, so the specific configuration of the particles in particle-scale models can have a significant impact on the result of a simulation. As the powder bed configuration is not generally known, this also leads to an uncertainty on model outputs. Unless the magnitude of these uncertainties on model outputs are quantified, it is impossible to say quantitatively whether an experimental result agrees with

the model prediction.

While uncertainty quantification is already being performed in fields such as heat transfer [70] and fluid flow, it's application to SLM modeling is relatively new. The goal of uncertainty quantification is to represent the stochastic relationship between the inputs and outputs of a model. The inputs are represented as probability density functions and the goal is to determine the probability density function of the output.

There are a number of techniques by which the probability density function of a model output can be obtained. The simplest class of these are sampling techniques, in which samples are drawn from known input probability distributions and used as model inputs [1]. The most basic of these techniques is Monte Carlo sampling. In Monte Carlo sampling, input samples are randomly drawn from the probability distributions of the model inputs. The specific values drawn are used as inputs to the model and the model output calculated. The process is repeated for a new set of randomly drawn inputs and the model output values collected in order to construct a probability density function. Monte Carlo sampling generally requires a large number of samples in order to accurately calculate the output probability distribution [24]. For a computationally expensive model, this can mean an unacceptably high number of model runs.

The Monte Carlo technique can be improved upon by selecting samples systematically instead of randomly. In Latin Hypercube sampling, samples are generated that are evenly spaced in terms of probability [24], allowing an

input distribution to be accurately sampled using fewer samples as each yields more information than a random sample. Latin Hypercube sampling generally outperforms Monte Carlo sampling in terms of number of model runs need to reconstruct the output distribution for most cases [24].

Sampling techniques are advantageous because they are the most broadly applicable. They can be used to calculate the output probability density function for any model given any type of input density functions. However, even with more advanced techniques such as Latin Hypercube, large numbers of samples are needed to accurately reconstruct an output distribution, making direct sampling generally unfeasible for computationally expensive models.

Another class of uncertainty quantification techniques are reliability methods. Reliability methods approximate the output probability distribution of a model using gradients and, in some cases, optimization techniques [1]. The simplest reliability method, the mean value method, approximates the mean of the output distribution as the value of the model evaluated at the mean values of all of the inputs and the variance as the sum of each of the input variances multiplied by the square of the partial derivative of the model with respect to that input [1]. This method requires relatively few model evaluations and scales well with the number of random inputs. However, the results will only be accurate for models that are close to linear and distributions that are nearly Gaussian. Multi-modal distributions cannot be captured at all [1].

This simple reliability method can be improved upon in a variety of ways. Optimization techniques can be used to minimize the distance between

the computed mode of the model output distribution and the true mode. Second derivatives of the model with respect to the inputs can be used to integrate around the mode to more accurately reproduce the surrounding distribution. Adaptive sampling can be used to improve the estimate further. Multi-modal distributions can be approximated by optimizing in multiple regions of input space to locate multiple modes and integrating around each one [1].

Reliability methods generally require the fewest model evaluations of any of the uncertainty quantification techniques and may be the only option for models with very large numbers of uncertain inputs. However, their ability to accurately calculate a model output distribution is dependent on the properties of the model and the input distributions. Convergence can also be an issue if optimization techniques are being employed. Finally, there is not clear mechanism to assess how accurately an output distribution is being calculated.

Another class of uncertainty quantification techniques are stochastic expansion techniques. The general idea with these techniques is to use model evaluations to build an easy to evaluate interpolant of the quantity of interest as a function of the model inputs and sample it instead of the model [1]. Stochastic expansion techniques generally require many fewer model evaluations than direct sampling techniques and are much more flexible than reliability methods. The error in the interpolant fit can also be used as an indication of how well the true output distribution is being calculated. However, the number of model evaluations required to build the interpolant can increase rapidly with an increasing number of uncertain model inputs.

In this thesis, a stochastic expansion technique called the generalized polynomial chaos (gPC) framework [69,70] is employed to perform uncertainty quantification due to the flexibility of the technique and the ease with which its accuracy can be assessed. Physical intuition and parameter sweeps are used to identify inputs which have the largest impact on the uncertainty of the output in order to keep the number of random inputs low. Smolyak sparse grids [55] are also used to reduce the number of model evaluations required.

The model output is expressed as a polynomial expansion in the input random variables with unknown coefficients as given in Equation 1.1 [70].

$$X(\theta) = \Sigma_{j=0}^{\infty} a_j \Phi_j(\zeta(\theta)) \tag{1.1}$$

X is the quantity of interest, θ is a vector of model inputs, a_j are the coefficients of the expansion, Φ_j are the basis polynomials, and ζ is a vector of random variables representing the input probability distributions. Φ_j are a tensor product basis of Legendre polynomials for uniform random inputs and Hermite polynomials for Gaussian inputs [69].

A stochastic collocation technique [16,68] is used in which the model is solved deterministically at selected collocation points, sparsely distributed in the space of possible input parameters [55]. These collocation points are then used in interpolation schemes to reconstruct the coefficients of the polynomial expansion. In this thesis, a Smolyak sparse grids are employed [55].

Once the coefficients of the expansion are known, the resulting response surface may be sampled by drawing samples from the input distributions to

predict a probability density function of the output. The standard deviation of the output is a measure of the overall uncertainty in the model prediction resulting from uncertainties in the inputs.

For particle-scale models, an additional source of uncertainty, packing uncertainty is present. Packing uncertainty is due to the randomness inherent in the generation of the powder packing structures. Since the initial positions of the DEM particles in the domain are random, the resulting packing structure of the settled particles is also random.

In this thesis, packing uncertainties are estimated by generating a number of different random powder bed configurations and using the average values of the input parameters to run simulations on them. The resulting standard deviation of the output quantities of interest is then a measure of the uncertainty in the model prediction due to the randomness of the powder bed. To estimate the overall uncertainty in the model prediction for models involving powder, the standard deviation due to packing uncertainty is added to the standard deviation due to input uncertainty in quadrature. Agreement with experimental results can then be quantitatively assessed based on the predicted distribution functions.

1.6 Goals of Thesis

The goal of this thesis is to develop a multi-scale modeling framework with uncertainty quantification that addresses the need for systematic uncertainty estimation in additive manufacturing modeling and provides a mech-

anism for using results and uncertainties from particle-scale models in larger bed-scale models. The thesis has the following important components:

Sensitivity Analysis of Bed-Scale Continuum Models. In order to improve the current state-of-the-art of bed-cale modling, it is important to understand what are the most important parameters governing model accuracy. To this end, this work seeks to implement a simple, bed-scale, finite volume heat transfer model of the SLM process using ANSYS Fluent [2]. Unlike in previous bed-scale modeling, uncertainties in the model output, temperature, will be systematically quantified using the Generalized Polynomial Chaos (gPC) framework [69, 70], and its sensitivity to various input parameters assessed. This model, described in Chapter 2, identifies absorption and extinction coefficient, effective thermal conductivity, and melt behavior are identified as the largest sources of uncertainty and thus further investigated using particle-scale modeling.

Development of Discrete Element Model to Yield Powder Properties. Another important goal of the thesis is to improve the modeling at the bed scale through the use of particle scale models for optical interactions, heat transfer, and melting. In order to calculate absorption and extinction coefficients for powders, the DEM will be used to represent a powder bed as a series of spherical particles. A ray-tracing method, similar to that used by Zhou and Zhang [79] will be used to predict how laser energy is deposited in

the powder bed. The method will be extended by examining the effects of a number of input parameters encountered in SLM and developing a correlation with uncertainty.

Effective thermal conductivity will be calculated using the DEM through techniques used previously by a number of groups [12, 62, 65, 78] involving constitutive models for particle to particle heat transfer. The approach will be extended with the addition of ray-tracing based radiation heat transfer to handle the high temperatures normally encountered in SLM. The effects of a number of SLM parameters will be considered and correlations with uncertainty developed.

Particle-scale melt behavior will be examined using a hybrid DEM-continuum technique with volume of fluid interface tracking as is done by Gurtler et al. [20]. Gurtler, however, only considers mono-disperse, regular packing structures, making the quantification of uncertainty due to random, polydisperse packing impossible. This work will consider random, polydisperse packing structures, as well as other SLM input parameters and, for the first time, develop a temperature-melt fraction relationship with uncertainty that can be used in bed-scale simulations.

Coupled Thermo-Mechanical Model of SLM. The final goal of the thesis is to combine particle and bed-scale models to achieve a complete thermo-mechanical model of the SLM process. A coupled thermal-mechanical model will be implemented building upon the work of Hodge et al. [23]. This will

be extended by leveraging the correlations for effective parameters developed previously in this work and the application of uncertainty quantification to identify the impact of the uncertain model inputs on the predicted residual stress.

1.7 Outline of Thesis and Its Contributions

The goal of this thesis is to develop a model of the SLM process that is capable of predicting a temperature and stress history with uncertainty of a part produced using a given set of processing parameters. A multi-scale modeling framework with uncertainty quantification is introduced that applies systematic uncertainty estimation to identify the largest sources of uncertainty in bed-scale models and uses particle-scale modeling to predict and estimate uncertainties on input parameters that have the largest impact. In so doing, this thesis introduces a mechanism for using results and uncertainties from particle-scale models in larger bed-scale models.

The thesis is laid out as follows.

Chapter 1: Extended Abstract The chapter provides a brief summary of the thesis and the primary results.

Chapter 2: Introduction This chapter introduces SLM, SLM process modeling, and uncertainty quantification. The current state of SLM process modeling is described along with existing shortcomings. The goals of this

thesis in addressing some of those shortcomings are laid out along with the approach that will be taken.

Chapter 3: Bed-Scale Thermal Model This chapter describes the of bed-scale thermal model equations and the initial implementation using ANSYS fluent. It describes the uncertainty quantification and model validation process and identifies the effective parameters that are the largest sources of uncertainty and thus targets for particle-scale modeling.

Chapter 4: Particle-Scale Models This chapter describes the particle-scale modeling approach, the DEM, and the generation of particle packing structures. It details the specifics of the constitutive models used to predict absorption and extinction coefficients, effective thermal conductivities, and temperature-melt fraction relationships. It discusses the model validation done for each particle-level model, the correlations developed, and the sources of uncertainty in each of the predictions.

Chapter 5: Bed-Scale Stress Model This chapter describes the bed-scale coupled thermal-mechanical model equations and their implementation in OpenFOAM. It discusses model calibration necessary and the impact of inherent uncertainties on the precision of residual stress predictions.

Chapter 6: Conclusions Describes results of the thesis as well as suggestions for future work.

The primary contributions of this thesis are:

- Coupled, bed-scale thermal-mechanical model of SLM process including systematic uncertainty quantification and use of powder effective properties calculated from detailed models not previously reported
- Experimentally validated particle-scale laser-particle interaction model predicting absorption and extinction coefficients of a powder. Quantification of uncertainty sources and development of correlations for SLM-specific scenarios not previously reported
- Experimentally validated particle-scale thermal conductivity model predicting effective thermal conductivity of a powder. Quantification of uncertainty sources and development of correlations for SLM-specific scenarios not previously reported
- Experimentally validated particle-scale melt model. Not previously reported use of melt model to predict temperature-melt fraction relationships of a powder with uncertainty
- New multi-scale framework for using results and uncertainties from particle-scale simulations to bed-scale models

Chapter 2

Bed-Scale Thermal Model

In this chapter, the governing differential equations for the thermal model at the bed scale are introduced. The finite volume discretization scheme, used for all bed-scale models, for solving the governing equations is described. An initial implementation of the model in ANSYS Fluent is done and the peak temperature rise after the laser irradiation of a powder bed is predicted. Bed-scale effective properties are estimated based on the literature and uncertainty bounds for these properties estimated. Uncertainty quantification is performed and the resulting output probability distribution is compared to experimental data from Wiria et al. [67]. The prediction is found to agree with the experiment given the uncertainty bounds, but large uncertainties are found to exist. The effective properties contributing the most to the uncertainty are identified and will be the targets for particle-scale modeling in Chapter 3.

2.1 Governing Equations

Heat transfer within the SLM powder bed is governed by the enthalpy equation [60].

$$\frac{\partial H_p}{\partial t} = \nabla \cdot (k_p \nabla T) + f(x, y, z, t) \tag{2.1}$$

k_p is the thermal conductivity, $T(x, y, z, t)$ is the temperature, $H_p(x, y, z, t)$ is the total enthalpy of the powder and $f(x, y, z, t)$ is the heat source.

Enthalpy and temperature are coupled through the relationship [60]

$$H_p = (1 - g_p(T)) \int_{T_{ref}}^{T} \rho c_s dT + g_p(T) \int_{T_{ref}}^{T} \rho c_l dT + g_p(T)\rho L \tag{2.2}$$

$g_p(T)$ is the melt fraction, ρ is the density, c_s and c_l are the specific heats of the solid and liquid phases, and L is the latent heat of fusion. In order for the equations to be closed, the melt fraction function of the powder, $g_p(T)$, must be specified. Commonly, the lever rule is used as a simple relation between melt fraction and temperature, $g(T) = \frac{T-T_s}{T_l-T_s}$, for T between T_s, the solidus temperature, and T_l, the liquidus temperature. For materials with a single melting temperature, T_s and T_l can be made arbitrarily close together. This method assumes a homogeneous material and uniform melting within a sample. As powdered materials are not homogeneous, finite rate transport effects are critical in determining the rate of powder melting and thus the $g_p(T)$ relation. It is part of this work to develop an appropriate $g_p(T)$ relationship for SLM.

The laser heat source is modeled as a Gaussian [42, 57].

$$f = \alpha I_0 \beta exp\left(-2\frac{(x - x_l)^2 + (y - y_l)^2}{\omega^2} - \beta z\right) \tag{2.3}$$

α is the optical absorptivity of the powder bed, I_0 is the laser intensity, x_l and y_l are the x and y positions of the laser, ω is the laser characteristic radius and β is the extinction coefficient.

The boundary of the domain, Ω is divided into Ω_1, the top surface of the powder bed, and Ω_2, the remaining surfaces. This is illustrated in Figure 2.1.

Adiabatic boundary conditions, $\left(\frac{\partial T}{\partial n}\right)\Big|_{\Omega_2} = 0$, are applied along Ω_2. A mixed

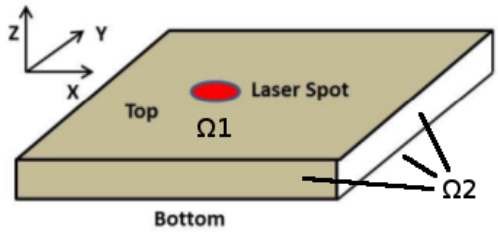

Figure 2.1: Illustration of Computational Domain

convective-radiative boundary condition, $k\left(\frac{\partial T}{\partial n}\right)\Big|_{\Omega_1} = h(T - T_\infty) + \alpha\sigma_b(T^4 - T_\infty^4)$, is applied on Ω_2.

For the thermal model, T and H are the output quantities of interest, I_0, $x_l(t)$, $y_l(t)$, and ω are controllable process inputs, and ρ, c_s, c_l, $g_p(T)$, k_p, α, and β are properties of the material.

2.2 Implementation Details

The bed-scale thermal model is a multi-phase system consisting of powder, consolidated (solid) material and a background gas (generally air). Additionally, the composition of the domain changes over time as new powder layers are added during the build. In order to model this, domains are initialized with an initial layer height. Material properties are then assigned in the domain based on location. Cells that lie entirely below the layer height are considered purely powder and those that lie entirely above it are considered purely air. Cells that cross the layer height are assigned a partial volume fraction of air and powder based on their position. As powder melting occurs

a new phase, consolidated material, is introduced. Based on results calculated from the thermal model, powder volume fractions are converted to solid volume fractions in cells that have undergone melting. When a new layer is added, the layer height is increased and the material properties of the cells are re-computed to reflect the change. Material properties of cells that contain a mixture of materials are computed using volume averaging as given in Equation 2.4.

$$\zeta_{total} = \alpha_{powder}\zeta_{powder} + \alpha_{solid}\zeta_{solid} + (1 - \alpha_{powder} - \alpha_{solid})\zeta_{air} \tag{2.4}$$

α is the volume fraction of each component and ζ is a given material property.

The solution to the thermal model is essentially an iteration between the temperature and enthalpy variables as Equation 2.1 involves both of these quantities. Since enthalpy is a function of temperature, a simple solution procedure would be to use values of enthalpy from the previous iteration to update the temperature field and iterate until the fields are consistent. However, this exhibits poor convergence and may not converge for cases when the enthalpy-temperature curve is sufficiently steep [60]. A more robust method, as suggested by Voller and Swaminathan [60], instead uses a Taylor series expansion to approximate the current iteration enthalpy from known values and the current iteration temperature.

$$H^{m+1} = H^m + \left.\frac{dH}{dT}\right|_{H^m} \left[T^{m+1} - H^{-1}\big|_{H^m}\right] \tag{2.5}$$

m+1 indicates values at the current iteration while m indicates values at the previous iteration. H^{-1} is the enthalpy inverse function which, given an en-

thalpy, returns the temperature value that produces that enthalpy. The term involving T^{m+1} is added to the matrix diagonal while the remaining terms are added to the right hand side. The equation is iterated until the temperature and enthalpy fields are consistent.

2.3 Numerical Method

The governing equations discussed previously are discretized using a finite volume discretization scheme. The domain is divided into polyhedral cells. In the case of SLM powder beds, the domain is regularly shaped and thus regular, hexahedral cells are used. The variable of interest (temperature) is stored at each of the cell centroids. The thermal governing equation is integrated over the cell control volumes to provide cell balances of energy for each cell (a description of the stress calculation is given in Chapter 4). This results in a system of N linear, algebraic equations with N unknowns, where N is the number of cells in the domain, for each governing equation. The resulting systems of equations are solved in matrix form and iterated until convergence is reached between the systems.

2.4 Results

In order to validate the thermal model, results from the model are compared to temperature measurements taken inside a build chamber using infrared thermography by Wiria et al [67]. A stationary laser was applied to a powder bed of poly(vinyl alcohol) (PVA) for 0.2ms and then a temperature

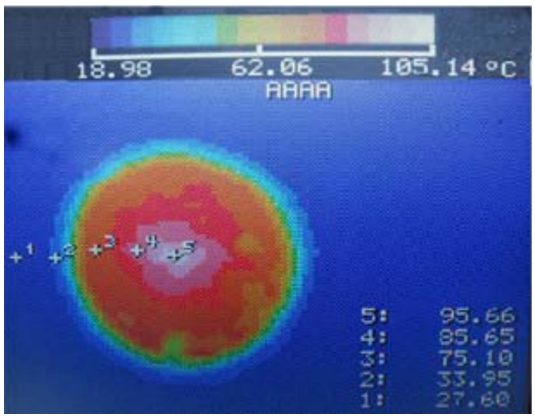

Figure 2.2: Temperature Profile Measured by Wiria et al [67]

measurement of the bed surface was taken approximately 1ms later using an infrared camera. The image is shown in Figure 2.2.

No pre-heating of the powder bed was used, and a peak temperature of 368.66 K (70.66 K above ambient) was observed. Although no error bounds on this measurement are given in the paper, the manufacturer or the infrared camera used (TVS-2300ST by Avio Nippon Avionics Co., Ltd) reports their instruments accurate to +/- 2K. The objective of the validation exercise is to predict this maximum temperature, to quantify the uncertainty in the prediction, and to identify the inputs which influence the outputs to the greatest degree. The material properties of poly(vinyl alcohol) are widely available in the literature. The properties of the laser used have been described by Wiria et al [67]. Thus, the properties needed for the model are set as per Table 2.1.

For the validation, a solution domain of 1mm x 1mm x 0.5mm is used and discretized into 100 x 100 x 50 hexahedral cells, for a total of 500,000

Property	Nominal Value
Laser Power	4 W [67]
Laser Beam Diameter	0.4 mm [67]
Laser Velocity	0 m/s [67]
Powder Density	1290 kg/m^3
Powder Conductivity	0.15 W/mK [33]
Powder Specific Heat	$0.0041T^2 + 3.7367T + 38.0621$ J/kgK [33]
Reflectivity	0
Average Particle Diameter	0.15 mm [67]
Simulation Time	1.2 ms [67]
Time Step	0.00005 s

Table 2.1: Properties for Thermal Model Validation

cells. Since the measurement was taken with a stationary laser applied to a powder bed of fixed height, the entire domain is initialized as powder cells and the heat source applied to the top of the domain; the addition of layers throughout the simulation is not needed.

A systematic quantification of the uncertainties in the simulation is performed using the generalized polynomial chaos method to allow validation against experimental data, along with sensitivity analysis to identify input parameters whose uncertainties matter the most. The input parameters investigated are powder density, powder conductivity, powder specific heat, average particle diameter, and simulation time. Laser power, beam diameter, and laser velocity are assumed to have been well-determined by the experimental setup and the effects of the reflectivity on the final peak temperature are considered small.

The density of PVA in the literature is given as 1270-1310 kg/m^3, de-

pending on the degree of crystallization. Therefore, the distribution of powder density is taken as uniform with minimum 1270 and maximum 1310 kg/m^3. The conductivity of solid PVA at ambient temperature is measured at 0.2 W/mK in the literature [33]. However, the conductivity of a powder will be lower than that of the solid due to the air gaps between particles. Furthermore, PVA conductivity increases as temperature increases. To account for these uncertainties, an effective powder bed conductivity is estimated to lie between 0 (as conductivities must be positive) and 50% above the value for the solid conductivity at ambient temperature. Therefore, a uniform distribution for thermal conductivity is assumed, spanning the range 0-0.3 W/mK.

The specific heat of PVA is given at various temperatures in [33] between 60 K and 300 K. A second degree polynomial is fitted to this data in MATLAB using a least squares algorithm. The polynomial is used to calculate the predicted specific heat for each temperature for which data is available and is compared to the measured specific heat. The standard deviation of the misfit is calculated at approximately 5%. However, we are primarily interested in the value of the specific heat at temperatures above 300 K, for which no data is available to calibrate a model. Additionally PVA undergoes a glass transition between 348 K and 358 K, during which a spike in specific heat over a narrow temperature range is typical for polymers [13], similar to a latent heat of fusion observed in metal alloys. As no data is available for the magnitude of this spike in specific heat for PVA, the standard deviation is doubled (to 10%) to account for possible error. Finally, the polynomial is used to evaluate the

specific heat at the measured peak temperature (368.66 K) and 10% of this value is taken as the standard deviation (200 J/kgK). Therefore, a random variable with mean 0 J/kgK and standard deviation 200 J/kgK is added to the specific heat calculation to account for errors in the curve fitting procedure as well as uncertainties on the impact of glassification on specific heat. Furthermore, errors in the specific heat data from which the curve fit was obtained are considered. The error in the specific heat measurements are reported to be less than 0.5% [33]. Given that this is an order of magnitude less than the curve fit error, it is neglected.

The average particle diameter of the powder used in the experiment is reported to be 0.15 mm [67]. As no error bounds or method of measurement were reported, a normal distribution is assumed with 10% of the measured value being one standard deviation. Particle diameter is not used directly in the model. However, as no method had yet been developed for estimating the absorption coefficient, β, of a powder at the time the validation was conducted, it is approximated as the inverse of the average particle diameter. Thus, this uncertainty in particle diameter is meant to incorporate not only the uncertainty in the particle diameter measurement, but also the uncertainty in the approximation of β.

As the temperature measurement in the experiment was taken after applying the laser to the powder bed for 0.2ms and then waiting approximately 1ms after the laser was turned off, some uncertainty is present as to at what the final simulation time should be. To capture the approximate nature of the wait

Input	Distribution
Powder Density	Uniform (1270-1310 kg/m^3)
Powder Conductivity	Uniform (0.0-0.3 W/mK)
Specific Heat Error	Normal ($\mu = 0$ $\sigma = 200$ J/kgK)
Particle Diameter ($\frac{1}{\beta}$)	Normal ($\mu = 0.15$ $\sigma = 0.015$ mm)
Simulation Time	Normal ($\mu = 1.2$ $\sigma = 0.25$ ms)

Table 2.2: Thermal Model Input PDFs

time, a standard deviation of 0.25 ms is assumed. The simulation time is thus assumed normally distributed with a mean of 1.2 ms and a standard deviation of 0.25 ms. The uncertain parameters and their probability distributions are summarized in Table 2.2.

Using these probability distributions, collocation points based on the Smolyak sparse grid [55] are generated, and used as inputs to the model. The peak temperature rise is calculated for all cases and a 3rd order polynomial response surface is fit to the results. Sensitivities are calculated using the elementary effects method, in which a single input is chosen and all other input are held constant at their mean values. The value of the derivative of the quantity of interest with respect to the chosen input is obtained at each of the collocation points using finite difference with respect to the input at its mean value. The values of the derivatives at all of the collocation points are then averaged to create a mean sensitivity with respect to the input as well as a standard deviation. These sensitivities are a measure of how much the quantity varies with each input. The mean and standard deviations resulting

Input	Sensitivity Mean	Sensitivity Standard Deviation
Powder Density	1.99 $K/(kg/m^3)$	0.4 $K/(kg/m^3)$
Powder Conductivity	12.0 $K/(W/mK)$	5.66 $K/(W/mK)$
Specific Heat Error	47.8 $K/(J/kgK)$	15.2 $K/(J/kgK)$
Particle Diameter	43.8 K/m	14.5 K/m
Simulation Time	7.56 K/ms	4.64 K/ms

Table 2.3: Thermal Model Sensitivities

from this procedure are shown in Table 2.3. The results indicate that the largest sensitivities of the peak temperature rise are with respect to the specific heat.

Additionally, the PDF of the quantity with respect to each individual input is obtained by holding all other inputs at their mean values and sampling the response surface across the probability range of each individual input. The standard deviation of the resulting quantity is a measure of the global sensitivity of the quantity to the specific random input. The means and standard deviations of the peak temperature rise generated by sampling the response surface along one parameter while holding all other parameters at their mean values are shown in Table 2.4. These results are in agreement with the results of the sensitivity derivatives, as the most sensitive parameter, given by the largest standard deviation, is the specific heat.

The probability distributions of the response surface sampled by varying each of the parameters individually are given in Figure 2.3. These distributions show the probability of each temperature increase achievable within in the input range of the random variable being sampled. The probability of a

Input	Mean	Standard Deviation
Powder Density	76.0 K	0.555 K
Powder Conductivity	76.2 K	3.18 K
Specific Heat Error	76.6 K	7.33 K
Particle Diameter	76.6 K	6.66 K
Simulation Time	76.0 K	1.28 K

Table 2.4: Means and Deviations of Temperature Rise with Respect to Individual Parameters

temperature value is calculated as the probability of the input variable taking the value needed to produce the given temperature.

The overall probability distribution generated by sampling the response surface over the entire input parameter space is given in Figure 2.4. The mean is 77.4 K and the standard deviation is 10.7 K, some 14% of the mean. Thus, significant uncertainty in the output temperature prediction exists.

Thus far, we have quantified the uncertainty in the quantity of interest resulting from input uncertainties. However, error is also introduced into the model due to numerical discretization. The accuracy of the model may be improved and the discretization error estimated using mesh refinement and Richardson extrapolation [49]. However, this approximation only holds if the discretized solution is asymptotically approaching the true value. To assess the validity of the approximation, the peak temperature is calculated using grid sizes of h/1.5 and h/2 (the number of cells in each dimension multiplied by 1.5 and 2, respectively). In the asymptotic regime, the difference between the peak temperatures calculated on finer and finer grids should be decreasing.

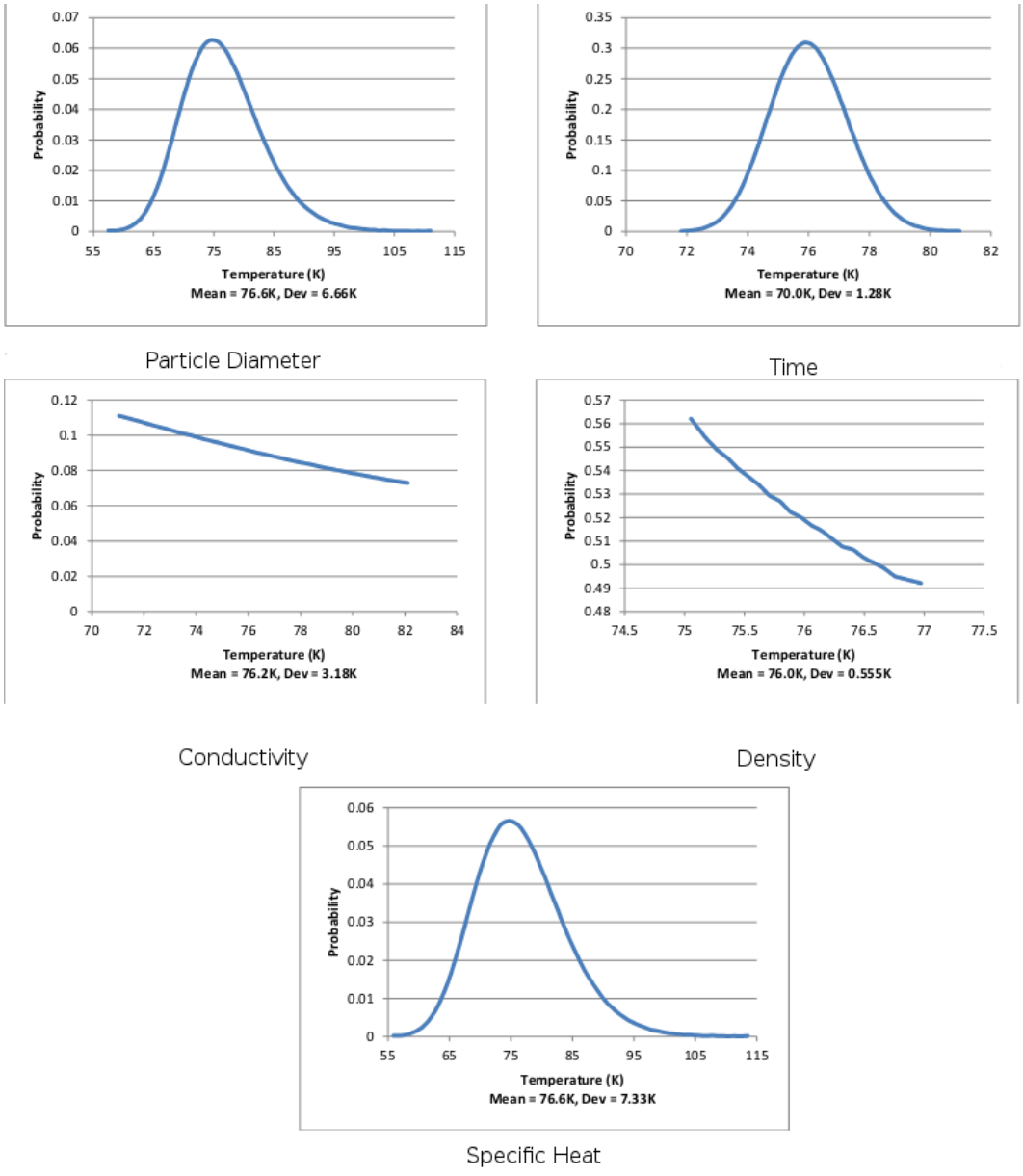

Figure 2.3: PDF of Peak Temperature With Respect to Individual Inputs [37]

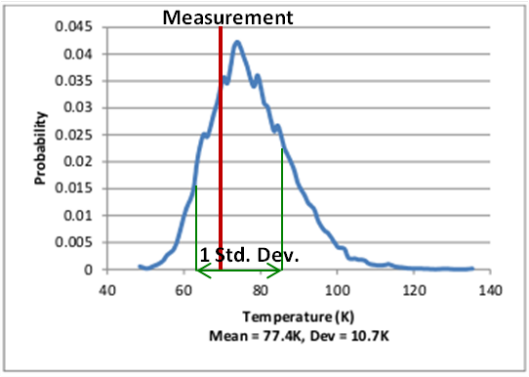

Figure 2.4: PDF of Peak Temperature Rise With Respect to All Inputs [37]

Mesh Size	Peak Temperature Rise
100 x 100 x 50	80.624 K
150 x 150 x 75	81.005 K
200 x 200 x 100	80.926 K

Table 2.5: Mesh Refinement Study

The results of the mesh refinement study using the nominal property values listed in Table 2.1 are shown in Table 2.5.

As can be seen, the difference between T_1 and $T_{1.5}$ is approximately 0.4 K and the difference between $T_{1.5}$ and T_2 is approximately 0.1 K, indicating both that the solution is asymptotically approaching a single value and that the discretization error is small compared to the standard deviation calculated in the sensitivity analysis. Thus, the discretization error is neglected for this calculation. The predicted maximum temperature is then obtained from Figure 2.4, giving a value of 77.4 K with a standard deviation of 10.7 K. Comparing this with the value measured in [67], it can be seen that the measured

peak temperature rise (70 K +/- 2 K) is within one standard deviation of the mean predicted by the model. However, the relatively large standard deviation compared to the magnitude of the temperature increase suggests that the uncertainty in model inputs must be reduced to improve prediction accuracy and to reduce the standard deviation of the predicted quantity. The results of the sensitivity analysis provide directions for future improvements. The largest sensitivities were calculated on the specific heat, particle diameter (and thus the absorption coefficient), and effective thermal conductivity. Therefore, reducing the uncertainty in these inputs is expected to have the largest effect on improving the predictions of the model as a whole. These quantities will thus be the targets for uncertainty reduction using particle-level modeling in Chapter 3.

2.5 Conclusions

A bed-scale thermal model of the SLM process is developed and implemented in ANSYS Fluent. The model is validated against experimental data available in the literature for a stationary laser. In order to quantitative assess agreement between the model prediction and experimental result, a systematic uncertainty analysis is performed. The model prediction is found to agree with the experimental result, given the calculated uncertainty. However, the uncertainty on the model prediction is found to be large due to the uncertainty on the effective thermal conductivity, specific heat (including heat of melting), and absorption coefficient. In the following chapter, detailed, particle-scale

models will be developed and implemented to allow these properties to the calculated more exactly.

Chapter 3

Particle-Scale Models

The bed-scale thermal model, described in the previous chapter, treats the heat transfer in the SLM powder bed using the enthalpy formulation of the heat conduction equation given in Equation 2.1. While density can be easily measured, and is often provided by the powder manufacturer, specific heat does not change when the solid material is powderized, and laser properties are either known or controllable, bulk properties such as extinction coefficient, effective optical absorptivity, effective thermal conductivity, and temperature-melt fraction relationships cannot be so easily inferred, and were identified as large sources of uncertainty for the bed-scale thermal model. While these properties may be available for the solid material, there is no assurance that they will not change significantly when the material is in powdered form. Thus, particle scale models are used to determine these properties. In this chapter, the development of particle scale models to compute absorption and extinction coefficients, effective thermal conductivities and temperature-melt fraction relationships using the DEM is described.

Particle-scale models generally use domain sizes on the order of 100 microns and simulation times of no more than a few milliseconds, as shown

in Figure 3.1. Thus, they are generally not suited for modeling the build of entire parts. However, by using particle-scale models on small, representative, domains of a powder bed, powder effective properties can be calculated for use in bed-scale models.

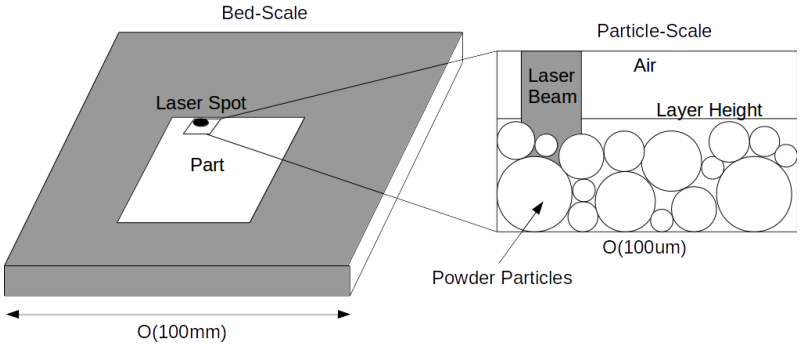

Figure 3.1: Schematic of SLM process at bed scale, and inset showing particle-scale domain

The Discrete Element Method (DEM), as implemented in the open source software MFiX [17], is used in all of the particle-scale models. An SLM powder bed is represented as a series of spherical particles, each with a position and radius [17, 40]. As the particles are made up of solid material, the known properties of the solid materials, not the powderized material, can be used as inputs. Particle packings are generated by inserting particles at a random location on the top of the domain and allowing them to interact with other particles and respond to gravitational forces. Particles with different sizes and material properties can be inserted with a user-specified distribution [40]. Particles interact with each other using a spring-dashpot model in which contact forces are generated based on the degree overlap a particle has with

its neighbors (described in detail by Garg et al. [17]). Once the particles settle, their positions and properties can be used as inputs to other constitutive models.

In this thesis, mono-disperse and Gaussian particle size distributions are used. Log-normal particle size distributions are also commonly encountered in real powders. King et al. [29] found that the powder used in their single track melt experiments was best characterized using a log-normal distribution. However, for small enough standard deviations, the porosity of a powder bed generated using a Gaussian size distribution is found to be similar to that of a powder bed generated using a log-normal distribution. For example, the stainless steel powder used by King et al. [29] was log-normal with a mean of 27 μm and a standard deviation of 4.25 μm. The average porosity of a powder bed generated with the DEM using this distribution is found to be 0.66 with a standard deviation of 0.05. The average porosity of a bed generated using a Gaussian distribution with the same mean and standard deviation is found to be 0.63 with a standard deviation of 0.05. Thus, it is concluded that log-normal particle distributions can be reasonably approximated using Gaussian particle distributions in the particle-scale models.

3.1 Optical Model

The optical model is used to determined effective extinction and absorption coefficients for a powder bed. Since randomly packed beds contain openings, laser radiation applied to the surface is not all absorbed at the

surface, but can penetrate into the bed through multiple reflections from particle surfaces. The extinction coefficient is a measure of how far the radiation can reach into the bed and is a function of bed geometry, particle size, and particle absorptivity/reflectivity. Additionally, the complex geometry of the powder bed surface means that the bulk absorptivity of the bed as a whole (the ratio of total power absorbed by the bed to incident power) can be less than or greater than the absorptivity of the smooth solid material.

Several studies have used Monte Carlo methods to determine the extinction coefficient in packed beds by measuring the fraction of emitted rays that are able to travel a given distance inside the bed [10,74]. Others have proposed theoretical models and compared them to Monte Carlo results [26,52]. Zhou et al. [79] used a Monte Carlo approach to apply a random uniform distribution of rays to the top of a bed of packed spheres and calculate how the flux diminishes with depth into the bed. However, none of these works consider scenarios encountered in the SLM process. Specifically, the polydispersity of powdered materials, a thin bed with a solid, partially reflective, lower boundary, and the presence of a small laser spot size were not considered. In this work, all of these effects are considered and their impacts on the extinction coefficient and effective absorptivity quantified, thus allowing the accurate calculation of these quantities for use in SLM bed-scale models. Considering all these effects enable critical parameters to be set correctly as the beam encounters various depths of powder due to build complexity, corners, overhangs, and the like.

3.1.1 Modeling Approach

The powder bed is represented using the DEM as a series of spherical particles, each with a position, radius, and optical absorptivity. The extinction and effective absorption coefficient of a powder bed are calculated using a ray tracing technique. Ray tracing is only valid in the geometric optic limit in which the ratio of the characteristic length to the wavelength of the laser is much greater than one [79]. For a spherical particle, this means that Equation 3.1 must be satisfied.

$$\frac{\pi D_p}{\lambda} \gg 1 \tag{3.1}$$

D_p is the particle diameter and λ is the laser wavelength. As all results in this work are calculated using the geometric optic assumption, it must be verified that this assumption is valid for any specific laser and powder before these results can be used.

Rays, each with a power of 1, are fired into the domain downwards from the top boundary. Each ray originates from a random x and y location and 10^6 rays are fired in each calculation to approximate the effects of a continuous radiation source. 10^6 was selected as it results in an uncertainty due to the randomness of the ray generation that is an order or magnitude less than uncertainties due to the randomness of the powder bed geometries. For each ray, a ray tracing algorithm [18] is used to determine which particle sphere the ray intersects first. The location of the ray-particle interaction is recorded, along with the amount of energy deposited, which is determined as the product

of the ray power and the particle absorptivity. The remaining power is then reflected, either specularly or diffusely.

For specular reflection, the direction of the reflected ray is found using the laws of reflection, namely, the incident ray, surface normal, and reflected ray are all in the same plane at the point of intersection, and the angle of incidence is equal to the angle of reflection. Thus, the reflected direction is given by Equation 3.2 [79].

$$u_{i,2} = u_{i,1} + 2n_i cos(\theta) \tag{3.2}$$

$u_{i,2}$ is the direction vector of the reflected ray, $u_{i,1}$ is the direction vector of the incident ray, n_i is the unit vector normal to the surface of the sphere the ray intersected at the point of intersection and θ is the angle between the incident ray and the surface normal, given by Equation 3.3 [79].

$$\theta = arcos(-[u_{1,1}n_1 + u_{2,1}n_2 + u_{3,1}n_3]) \tag{3.3}$$

For diffuse reflection, each ray is reflected in a random direction in the outward facing hemisphere from the point of intersection to capture the diffuse nature of the reflection. In this case, a coordinate shift centered about the point of intersection is performed to calculate the direction of the reflected ray. The unit vectors, i_2, j_2, and k_2 of the shifted coordinate system are given by Equations 3.4, 3.5, and 3.6 [79].

$$k_2 = n_i \tag{3.4}$$

$$i_2 = \frac{k_2 \times k_1}{|k_2 \times k_1|} \tag{3.5}$$

$$j_2 = k_2 \times i_2 \tag{3.6}$$

k_1 is the z-aligned direction vector in the primary coordinate system. A random point on the unit sphere centered at the point of intersection is chosen in the new coordinate system using the Marsaglia rejection method [34]. An additional rejection criterion is applied that the chosen point must have a non-negative k_2 component to ensure that a point on the outward facing hemisphere from the intersection is chosen. Finally, the vector determined by connecting the intersection point with the point chosen by the Marsaglia method is shifted back to the original coordinate system by multiplying by the matrix in Equation 3.7 [79].

$$\begin{vmatrix} i_{2,1} & j_{2,1} & k_{2,1} \\ i_{2,2} & j_{2,2} & k_{2,2} \\ i_{2,3} & j_{2,3} & k_{2,3} \end{vmatrix} \tag{3.7}$$

$i_{2,i}$, $j_{2,i}$, and $k_{2,i}$ are the vector components of the i_2, j_2, and k_2 unit vectors in the original coordinate system. Reflected rays continue to be traced until they either exit the domain or their power falls below 1% of their initial value.

3.1.2 Results and Discussion

In order to demonstrate the capability of the model in calculating optical properties of powders, the model is applied to free (bed depth much greater than laser penetration depth), monodisperse powder beds and the results are compared to existing experimental and computational results from

the literature. All units of length are non-dimensionalized by the radius of the particles in order to maintain generality. The beds generated have dimensions 20Rx20Rx20R. In order assess the impact of the randomness of the bed generation on the calculated quantities, 30 different powder beds are generated with the same dimensions and results are averaged across them. Average properties for the powder beds generated are shown in Table 3.1. These properties are in

Property	Mean Value	Deviation
# of Particles	1098	4.4
Porosity	0.425	0.002
Avg Coordination Number	5.13	0.1

Table 3.1: Average Powder Bed Properties

general agreement with those of Zhou et al [79], who used a gravitational minimization technique to generate packing structures computationally. A sample packing structure is shown in Figure 3.2.

Previous works have examined the transmittance of powder beds of specularly reflecting spheres with solid absorptivity of 0.4, which is defined as the incident radiative flux at a given depth in the bed divided by the incident flux at the surface of the bed. Transmittance is related to the extinction coefficient by the Beer-Lambert law, given by Equation 3.8.

$$T = I/I_0 = e^{-\beta z} \tag{3.8}$$

In order to validate against the existing literature, the transmittance is measured at various bed depths using the current specular model with a solid

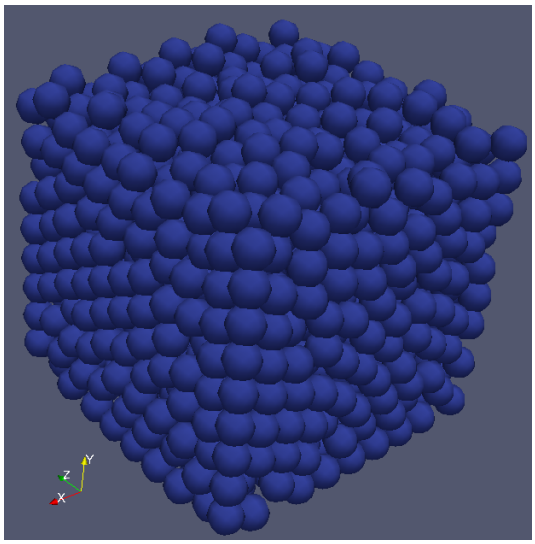

Figure 3.2: Sample Packing Structure

absorptivity of 0.4 by tracking the number of rays that are incident to the horizontal plane at the given depth divided by the total number of rays fired. Uncertainties are due to the random nature of the packing structures generated and are estimated by calculating the transmittance across all 30 different packing structures and taking the standard deviation of the result. The results are shown in Figure 3.3. Error bars represent two standard deviations for a 96% confidence interval. As no uncertainty estimates were given by the works used for comparison, it is difficult to quantitatively assess agreement. However, values from this study show good general agreement, particularly for shallower depths. As depth increases, uncertainties begin to dominate as the transmittance becomes more and more sensitive to differences in powder bed geometry. As few rays are able to penetrate to larger depths, slight differences in geometry (i.e., a pore extending from the surface to the given depth) can

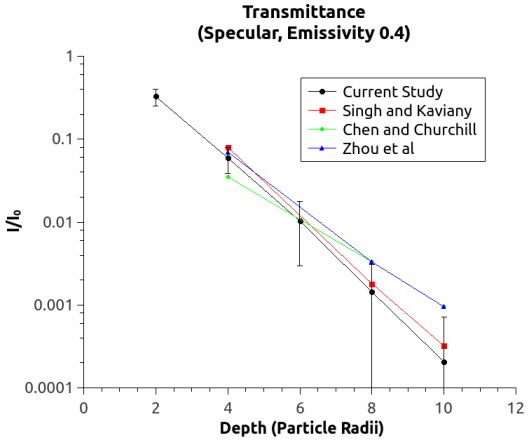

Figure 3.3: Comparison of Transmittance Measured/Calculated by Previous Works and Current Model [8, 52, 79]

have a large impact on the number of rays that can reach that depth. The extinction coefficients (normalized by the particle radius) calculated using the Beer-Lambert law from each of these sets of data are given in Table 3.2. As

Data	βR	Deviation
Singh & Kaviany	0.7	0.1
Chen & Churchill	0.75	0.08
Zhou et al	0.70	0.02
Current	0.7	0.1

Table 3.2: Comparison of Extinction Coefficients

can be seen, all studies are within range of each other given the error.

In SLM calculations, generally it is not the transmittance of a powder bed that is needed, but rather the amount of energy absorbed below a given depth. This is given by Equation 3.9.

$$\int_z^\infty \epsilon I_0 e^{-\beta\zeta}\,\mathrm{d}\zeta = \frac{1}{\beta}\epsilon I_0 e^{-\beta z} \tag{3.9}$$

This allows the amount of energy absorbed between two depths in the bed to be calculated as a simple difference. This quantity is calculated by recording the location of every ray-particle interaction in which energy is absorbed by a particle and the amount of energy absorbed. The amount of energy absorbed below a certain depth can then be determined by summing up the energy absorbed in all interactions below a given depth. This quantity is plotted in Figure 3.4 for both specular and diffusely reflecting particles with solid absorptivity of 0.4. The error bars indicate two standard deviations.

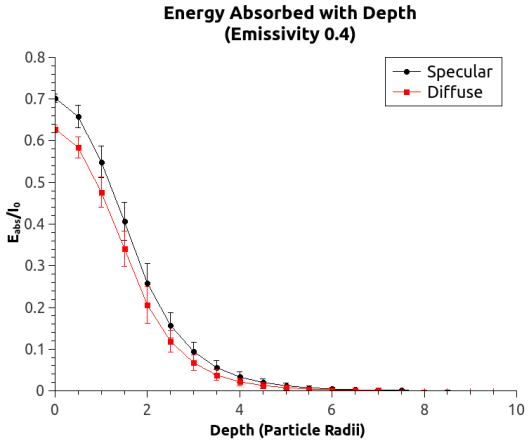

Figure 3.4: Energy Absorbed with Powder Bed Depth

The extinction coefficient can be calculated from this data by curve fitting an exponential decay function using a Levenberg-Marquardt least squares minimization algorithm [47] and taking the negative of the exponential factor. This gives an extinction coefficient of 0.58/R with a standard deviation of 0.02/R for specular particles and 0.61/R with a standard deviation of 0.02/R for diffuse particles. The total powder effective absorptivity (ratio of energy

absorbed by the powder bed to energy incident on the powder bed) can then be calculated as the value of the absorption profile at a depth of zero times the extinction coefficient. This gives an effective absorptivity of 0.46 with a standard deviation of 0.01 for specular and 0.43 with a standard deviation of 0.01 for diffuse. As can be seen, assuming specular or diffuse reflections has little difference on the calculated optical properties. Extinction coefficients are identical to within the uncertainty and absorptivities differ only by 6%. Thus, all particles will be assumed to be specular for the remainder of this work. The extinction coefficients calculated by this method differ somewhat from those calculated using the transmittance. This can be explained by the fact that both the Beer-Lambert law (equation 3.8) and the formula for energy absorption with depth given by equation 3.9 apply to continuous media and thus their application to powder beds is an approximation. However, since it is usually the energy absorption profile and not the transmittance that is used in SLM simulations, the absorption profile method will be used to calculate extinction coefficients for the remainder of this work.

In order to examine the effect of various parameters on extinction and absorption coefficients, absorption profiles are calculated for powder beds that are not free (i.e., beds that are not infinitely deep). These are encountered in SLM applications when a fresh layer of powder is spread on top of an already sintered layer. This situation is simulated by considering a very thin domain with a bottom boundary that has the same optical properties as the powder particles. That is, rays intersecting the bottom boundary will be par-

tially absorbed (with solid absorptivity equal to that of the powder particles) and the remainder reflected back up into the domain to possibly interact with additional particles. The same packing configurations already generated are used for these scenarios by simply discarding all particles that extend above a certain cutoff. The resulting absorption profile, averaged over all packing configurations, for powder beds with solid, partially reflecting bottom boundaries 2, 4, 6, 8, 10, and 20 particle radii from the bed surface is shown in Figure 3.5. Error bars indicate two standard deviations.

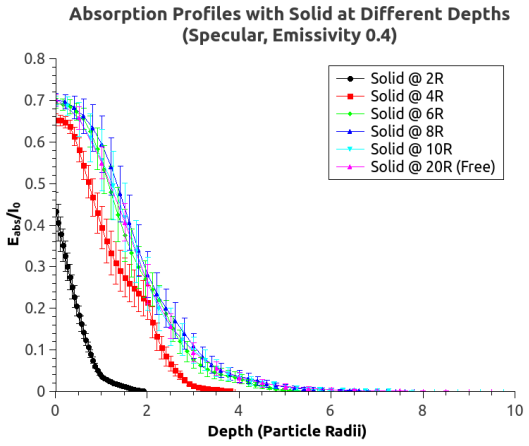

Figure 3.5: Energy Absorbed with Powder Bed Depth (Specular)

As can be seen in Figure 3.5, the presence of a solid bottom boundary has a large impact on the absorption profile at shallow depths, but this effect diminishes quickly as the boundary is moved deeper into the bed and by a depth of 6 particle radii the results are indistinguishable from the results for a free bed given the uncertainties. Also note the presence of a kink in the absorption curve for a solid boundary at 4R that occurs at a depth of approx-

imately 2R. This is due the fact that rays are bouncing off of the solid bottom boundary and being absorbed primarily by particles in the very bottom layer, as these are the closest to the boundary. Thus, the rate at which energy is being deposited with depth for the bottom layer of the bed (a depth of 2R-4R in this case) is larger than for the depths just above it, leading to a kink in the absorption profile. Beds with only 2R of depth do not experience this effect as there is only a single layer and for beds with depths greater than 4R, not enough energy is reaching the bottom boundary to have the reflections off of it make a significant impact. The calculated values for the extinction and absorption coefficients are plotted against the depth of the solid boundary in Figure 3.6.These results indicate that absorption depends a lot on the part geometry and the presence of powder versus solid layers and is not just a function of powder or bulk properties. This can have tremendous implications on the part quality and part certification.

As a reflecting boundary at shallow depths reflects energy back into the upper layers of the particle bed that would otherwise be transmitted deeper, it is expected that the extinction coefficient would be increased for these cases, which is indeed what is shown in Figure 3.6. It also shows that the absorption coefficient is increased by the presence of a shallow reflecting boundary, meaning that more total energy is absorbed by the bed for these cases as well.

Next, the effect of solid absorptivity is examined. Solid absorptivity is the ratio of the amount of radiation absorbed by a solid surface to the amount incident on it. Solid absorptivity enters the calculation whenever there is a ray-

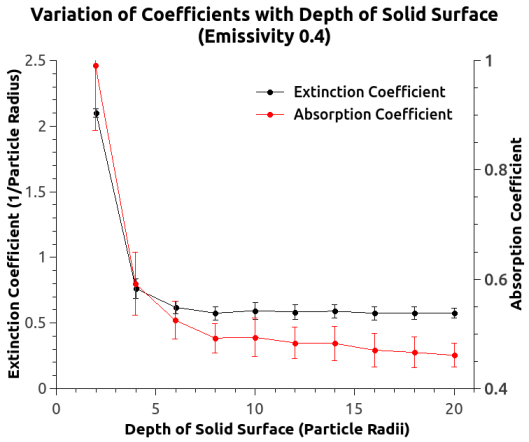

Figure 3.6: Variation of absorption and extinction coefficients as a function of depth of the solid boundary

particle interaction. The amount of the ray's energy that is absorbed by the particle is determined by the solid absorptivity and the remainder is reflected. In general, solid absorptivity is a function of the wavelength of the incident radiation, which is determined by the properties of the laser being used in SLM, and can vary from 0 (no absorption) to 1 (complete absorption). Figure 3.7 shows the absorption profiles for beds with solid absorptivities ranging between 0.1 and 0.9. In all previous scenarios, the solid absorptivity was set to 0.4. Again, uncertainties are the result of averaging over 30 different randomly packed beds and error bars represent two standard deviations.

As can be seen, very low solid absorptivities have an impact on the absorption profile of the powder bed, but the magnitude of this impact decreases as the absorptivity approaches 1. The resulting bed extinction and absorption coefficients are plotted against solid absorptivity in Figure 3.8. Although both

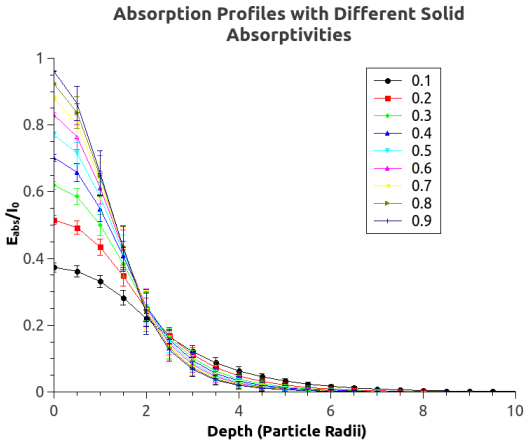

Figure 3.7: Absorption Profiles for Different Solid Absorptivities

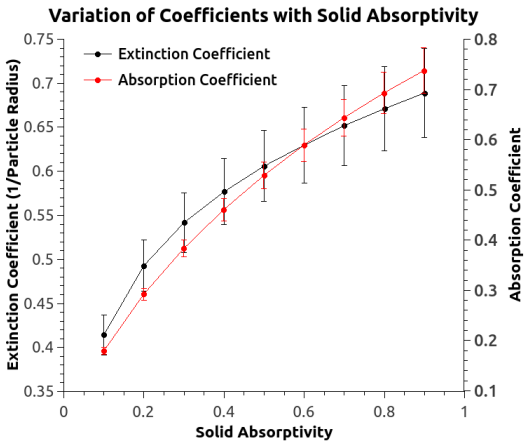

Figure 3.8: Variation of absorption and extinction coefficients as a function of solid absorptivity

the extinction and absorption coefficients vary with the solid absorptivity, the variations are smaller than those observed due to a shallow bed depth. For example, across the range of solid absorptivities, the extinction coefficient varies by about 50%, whereas it changed by almost a factor of 4 for shallow depths. This is consistent with findings of other groups [52] that the extinction coefficient is a function mostly of geometry as opposed to the properties of the solid material.

The size of the laser spot can also have an impact on the absorption profile of a powder bed. All previous calculations have assumed that radiation is incident over the entire surface of the domain. However, in SLM this is not the case. Radiation is due to a laser spot applied to a small portion of the domain. If the radius of the laser is small compared to the particle radius, this may have an impact on the calculated optical properties. Thus, calculations are run with the area on the top surface of the domain in which rays are fired restricted. Instead of rays originating from anywhere on the top surface, a spot on the surface is randomly chosen and rays are fired over a square of fixed dimension. The square dimensions can be varied to approximate different laser spot sizes relative to the particle size. The center of the simulated laser is placed in 5 different random locations on each of the 30 packing structures to estimate the uncertainties. The absorption profiles calculated for different laser sizes are shown in Figure 3.9.

Although the absorption profiles are not significantly altered by the laser spot size, what is most notable is the change in the uncertainties. The

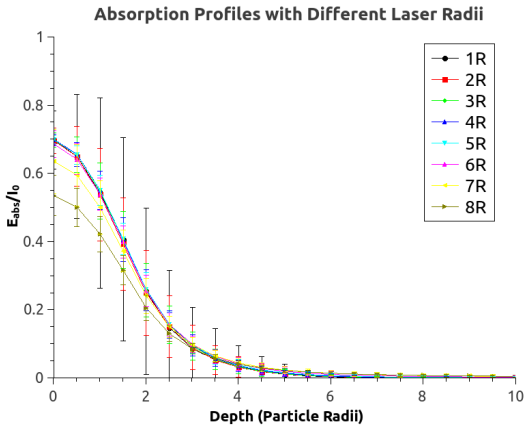

Figure 3.9: Absorption Profiles for Different Laser Spot Sizes

smaller spot sizes have very large uncertainties which diminish as the spot size grows. This is due to the fact that for small spot sizes, the results are high geometry dependent. The way in which energy is absorbed when a laser spot the size of a particle diameter is placed directly over a particle will be very different than if it were placed directly over a gap between two particles.

To emphasize this, Figure 3.10 shows the variation of the extinction and absorption coefficients with different laser spot sizes along with the uncertainties. This indicates that for more predictable part quality, one needs to use wider laser beams relative to the particle size. As can be seen, for small laser radii, the uncertainties in the extinction and absorption coefficients are so large as to make the calculation nearly useless. For such scenarios, approximating a powder bed as a continuum for purposes of calculating energy absorption from laser radiation is invalid and individual powder particles must be resolved in order to combat uncertainties in powder bed geometry. It is not until the laser

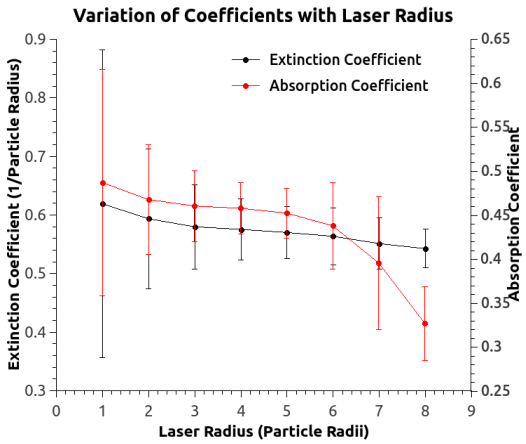

Figure 3.10: Variation of absorption and extinction coefficients as a function of laser spot size

radius reaches 5R that the uncertainties drop to values comparable to what was seen with rays fired from everywhere in the domain.

Finally, the previous calculations have not considered the fact that powders are generally not monodisperse (all particles the same size), but rather contain a distribution of particle sizes. In order to study the effects of polydisperse powder beds, packings are generated with particles of different sizes. When a particle is added to the domain, it is added not only at a random location, but also with a random diameter. For simplicity, a Gaussian particle size distribution is assumed, although the process can be used to simulate other distributions as well. The Gaussian assumption simplifies the analysis significantly as these distributions are completely determined by only two parameters (mean and standard deviation), thus reducing the parameter space to explore. The Gaussian distribution is split into nine bins, each with a

representative diameter and a fraction of the total number of particles determined by the Gaussian. Particles entering the domain then get assigned one of the nine possible diameters based on the probability of each. Once the beds are generated, rays are fired and traced through the domain to calculate the optical properties exactly as was done for the monodisperse cases, with uncertainties being calculated by averaging over 30 different beds all with the same size distribution. All distributions have a mean diameter of 1, but the standard deviations of the distribution is varied and the resulting absorption profiles shown in Figure 3.11.

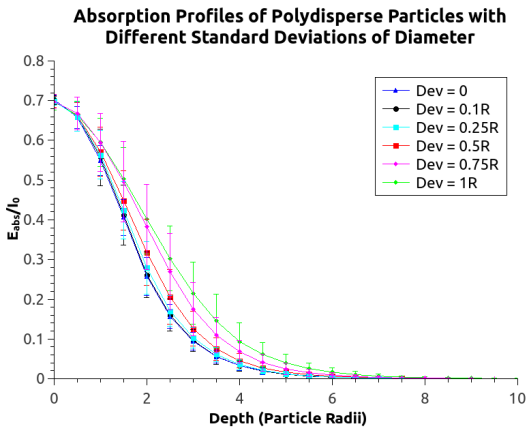

Figure 3.11: Absorption Profiles for Different Size Distributions

Small standard deviations of mean particle diameter have almost no measurable effect on the absorption profile. It is only for standard deviations closer to 1R that the impacts can be clearly seen. Uncertainties also increase with larger standard deviations as there are now additional sources of geometric uncertainties, particle sizes as well as particle positions. The variation

of extinction and absorption coefficient with the standard deviation of the particle diameter distribution is shown in Figure 3.12.

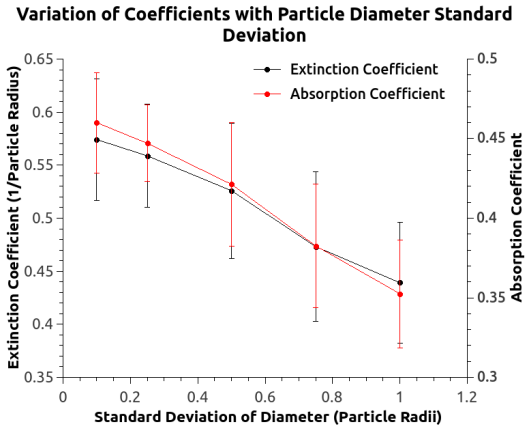

Figure 3.12: Variation of absorption and extinction coefficients as a function of particle size distribution

The largest variations of both extinction and absorption coefficient come from the presence of a solid boundary at a shallow depth relative to the particle radius. In order to provide easy calculation of these coefficients for SLM modeling applications, exponential decay functions are fit to the data from Figure 3.6 for specular particles with a solid absorptivity of 0.4 and a solid boundary between 2 and 8 particle radii in depth. Equation 3.10 shows the developed relation for the extinction coefficient,

$$\beta = 12.64e^{-1.06z} + 0.58 \tag{3.10}$$

where z is the depth of the solid boundary, and both z and β are normalized by the particle radius. Comparison of the empirical relation with the calculated

data shows that the maximum error committed by using the relation is 0.02/R. Equation 3.11 shows the relation developed for the absorption coefficient,

$$\alpha_{eff} = 2.48e^{-0.81z} + 0.50 \tag{3.11}$$

where z is the depth of the solid boundary and is normalized by the particle radius. Comparison of the empirical relation with the calculated data shows that the maximum error committed by using the relation is 0.01. For solid boundaries greater than 8 particle radii in depth, the results from the calculations without a solid boundary can be used. This gives a quantitative value for the range of the influence of overhangs and edges on parts produced.

The extinction and absorption coefficients also vary significantly with the solid absorptivity of the particles. Empirical relations are developed for these results as well using the data from Figure 3.8 for specular particles with solid absorptivity between 0.1 and 0.9. The relation developed for the extinction coefficient is given by Equation 3.12,

$$\beta = 0.325 + 1.03\alpha - 1.22\alpha^2 + 0.587\alpha^3 \tag{3.12}$$

where α is the solid absorptivity and β is normalized by the particle radius. Comparison to the calculated data shows that the error in the relation is at most an order of magnitude less than the uncertainty due to the random packings, so a standard deviation of 0.02/R can be used. The relation for the absorption coefficient is given by Equation 3.13,

$$\alpha_{eff} = 0.053 + 1.37\alpha - 1.04\alpha^2 + 0.399\alpha^3 \tag{3.13}$$

where α_{eff} is the bulk absorptivity coefficient and α is the solid absorptivity. Comparison to the calculated data shows that the error in the relation is at most an order of magnitude less than the uncertainty due to the random packings, so a standard deviation of 0.02 can be used.

The effect of particles being specularly or diffusely reflective has been shown to be small, meaning that the results shown here for specular particles can be used for diffuse particles as well, with the error introduced being less than 6%. These results also apply for laser diameters greater than 5 particle radii. For smaller laser diameters, uncertainties dominate the calculations and individual geometries must be considered. Additionally, these relations for monodisperse powders are applicable to Gaussian polydisperse ones as well, as long as the standard deviation of the particle diameter is less than 0.5R, the error committed is less than 8%. For larger standard deviations, or non-Gaussian particle size distributions, results need to be calculated directly using the ray tracing model.

3.2 Conductivity Model

The conductivity model is used to determine the effective thermal conductivity of a powder bed. Numerous works have investigated, experimentally, analytically, and computationally the effective thermal conductivity of powdered materials [63]. Masamune and Smith [35], Cheng and Vachon [9], Gusarov et al. [21], and Slavin et al. [53,54] all developed analytical models of conductivity of powder beds. Xue and Barlow [71,72] and Yuan et al. [75] both

measured the effective thermal conductivities in Nylon-12 powder beds and developed empirical relations from this for SLM applications. Sih [50] measured the effective thermal conductivities, as well as other bulk powder properties, of a variety of metals for use in SLM. Vargas and McCarthy [64] used a particle dynamics simulation to predict the effective conductivity of granular media. Zhang et al. [78], Tsory et al. [62], Widenfeld et al. [65], and Feng et al. [12] all used Discrete Element Models (DEM) to calculate the thermal conductivity of powder beds. However, none of these works consider powder bed scenarios commonly found when performing SLM, specifically, finite bed depths, when a thin layer of powder is present on top of a solid, already sintered, surface, and temperatures close to the melting temperature where radiation effects become increasingly important. This thesis uses DEM to examine the impact of these, as well as other, effects on the effective thermal conductivity of a powder bed.

3.2.1 Modeling Approach

Each DEM particle is modeled as a lumped capacitance control volume with a single, uniform temperature. Temperature gradients within particles are not resolved. Heat can be exchanged between particles via particle-particle conduction ($\dot{Q}_r$), particle-fluid-particle conduction ($\dot{Q}_{pfp}$), and radiation ($\dot{Q}_{rad}$). The net heat source in a particle is then given by the sum of all the heat being exchanged with all other particles across all three mechanisms as illustrated in Figure 3.13. Heat transfer between the particles and the background gas is neglected as the gas conductivity is an order or magnitude less

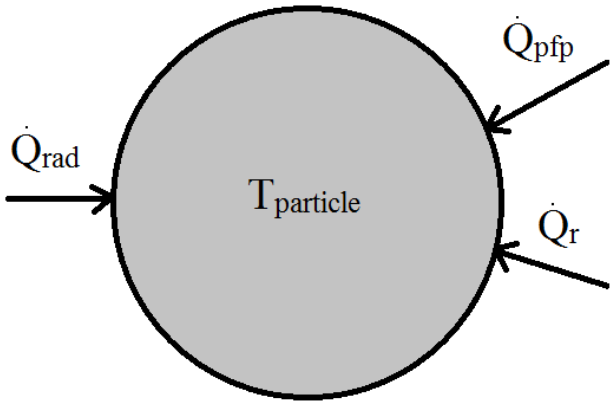

Figure 3.13: Particle Model

than the calculated effective thermal conductivities. Scoping calculations have been performed which establish that this approximation has negligible impact on results.

Fixed temperatures are set at two opposite walls of the domain, as shown in Figure 3.14. All particles are given an initial temperature and net heat sources are calculated for each particle. Powell's method [46], with Jacobians calculated by finite differencing, is then used to determine a temperature for each particle such that $\dot{Q}_r + \dot{Q}_{pfp} + \dot{Q}_{rad} = 0$, thus putting the particle bed in steady state. Once the steady state particle temperatures are known, the heat fluxes from the walls are calculated and from these the effective thermal conductivity is determined using Fourier's law.

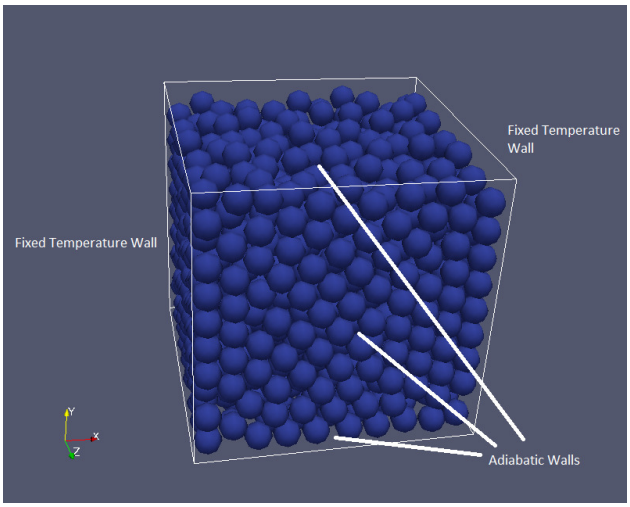

Figure 3.14: Particle Bed

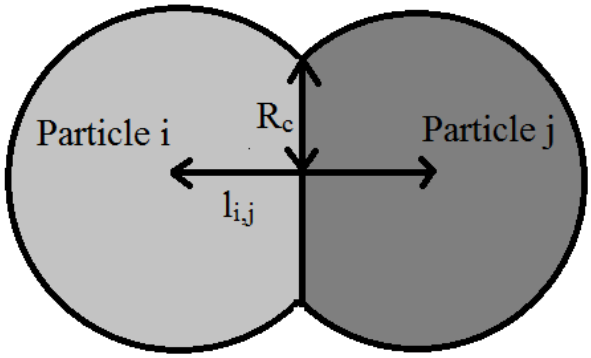

Figure 3.15: Particle-Particle Conduction

3.2.1.1 Particle-Particle Conduction

The particle-particle conduction model accounts for the heat transfer due to particles being in direction contact. The MFiX-DEM particle-particle conduction model uses a modified Batchelor and O'Brien [4] method. Batchelor and O'Brien drew a comparison between the temperature distribution inside two spherical particles in contact via a contact circle, as shown in Figure 3.15, and the velocity potential in an incompressible, irrotational flow through a circular hole in a plate wall. The heat flux at a radius r in the contact circle between two particles, i and j, is thus given by Equation 3.14 [4]. The radius of the contact circle between the particles is given by Equation 3.15.

$$q(r) = \frac{k(T_j - T_i)}{\pi\sqrt{R_c^2 - r^2}} \tag{3.14}$$

$$R_c = \sqrt{R_i^2 - \left(\frac{R_i^2 - R_j^2 + l_{i,j}^2}{2l_{i,j}}\right)^2} \tag{3.15}$$

Integrating Equation 3.14 along the contact circle from 0 to R_c and setting k equal to the harmonic average of the individual particle conductivities, k_i and k_j, yields Equation 3.16 for the total heat transfer between the two particles [40].

$$\dot{Q}_r^{(i,j)} = \frac{4k_ik_j}{k_i + k_j} R_c(T_j - T_i) \tag{3.16}$$

Gusarov et al. [21] and Vargas and McCarthy [64] use a similar model in their efforts. A similar equation applies for a particle in contact with a wall, which is modeled as a flat plane. In that case, $l_{i,j}$ is defined as the distance between the particle center and the wall and the contact radius becomes $R_c = \sqrt{R_i^2 - l_{i,j}^2}$

When using the MFiX-DEM spring-dashpot model to generate bed packing structures, the size of the time step that the explicit solver can take is governed by the value of the particle spring constant used in the model [17]. Thus, if spring constants were set to values reflective of the actual material Young's modulus, the necessary time step size would be prohibitively small. To counteract this, particles are generally modeled as being softer than they actually are in order to reduce the computational cost. Reducing spring coefficients to 10^5 N/m is found to have little impact on the resulting packing structures as compared to much stiffer coefficients and results in greatly reduced computational times.

However, when using the heat transfer models, this leads to an overestimation of the overlap between particles and thus an overestimation of particle-particle conduction. Therefore, a correction is applied to R_c by equating the normal contact force calculated by the spring-dashpot model ($F_n = k_n \delta_s$) with the contact force calculated using Hertzian contact theory ($F_n = \frac{4}{3} E_e R_e^{1/2} \delta_h^{3/2}$), where δ_s is the particle overlap predicted by the spring-dashpot model. The equation is solved for δ_h, the overlap predicted by Hertzian theory, and that is used to calculate a new radius of contact to use in the heat transfer model. [78].

$$R_{c,e} = \left(\frac{3 k_N l_{i,j} R_e}{4 E_e} \right)^{1/3} \tag{3.17}$$

$$\frac{1}{R_e} = \frac{1}{R_i} + \frac{1}{R_j} \tag{3.18}$$

$$\frac{1}{E_e} = \frac{1 - \nu_i^2}{E_i} + \frac{1 - \nu_j^2}{E_j} \tag{3.19}$$

Thus, while softer particles are used for bed generation, true particle material properties are used by the heat transfer model.

In this analysis, the contacts between particles are assumed to be perfectly smooth. Thus, while contact resistance is modeled using the contact radius, the effect of surface roughness, which can reduce the effective contact radius further, is not included. By its nature, the DEM approximates particles as perfectly spherical and is not expected to yield good predictions for non-spherical particles or particles with highly irregular surfaces. As is discussed in sections 3.1 and 3.2, the smooth, spherical particle model outlined here yields good results for metal powders, but ceramic powders require calibration.

3.2.1.2 Particle-Fluid-Particle Conduction

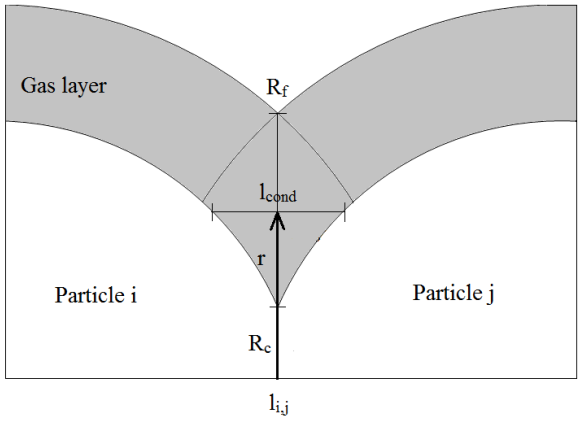

Figure 3.16: Particle-Fluid-Particle Conduction

The particle-fluid-particle model accounts for the heat transfer between the particles through the gas layer around the particles which occurs when

two particles are close by. This is illustrated in Figure 3.16. This mechanism differs from the conduction of heat from a particle or wall to a background gas and then back to a particle or wall some distance later. The particle-fluid-particle mechanism accounts for heat transfer directly between particles close to each other across a small interstitial gas path. The MFiX-DEM particle-fluid-particle conduction model uses a modified Rong and Horio [48] method.

Rong and Horio modeled the heat transfer through the gas layer by envisioning conduction pathways parallel to the centerline connecting two particle centers. For each conduction pathway, the distance between the surfaces of the particles is calculated and the heat transfer computed using Fourier's law with the thermal conductivity of the gas and the particle temperatures [48]. The total heat transfer between the particles is then calculated by integrating across all conduction pathways, giving Equation 3.20.

$$\dot{Q}_{pfp}^{(i,j)} = k_g(T_j - T_i) \int_{R_c}^{R_f^{(i,j)}} \frac{2\pi r}{l_{cond}} dr \tag{3.20}$$

$$l_{cond} = l_{i,j} - \left(\left(R_i^2 - r^2\right)^{1/2} + \left(R_j^2 - r^2\right)^{1/2} \right) \tag{3.21}$$

l_{cond} is the conduction distance between the two particles at a given r value, and R_f is the fluid radius, the radius of the circle formed by the overlap of the two particle's fluid lenses. A fluid lens is a layer of fluid surrounding a particle in which particle-fluid-particle heat transfer can occur. By default, MFiX-DEM uses a value of 0.2R for this parameter [40]. Equation 3.20 contains a singularity at the point of contact between two particles as the conduction

distance goes to zero. This is remedied in MFiX-DEM by imposing a minimum conduction distance, which is set to $1\mu m$ by default [40].

3.2.1.3 Radiation

In this paper, the heat transfer models of MFiX-DEM are extended by the addition of a view factor radiation model. The view factor model is only valid in the geometric optic limit, so $\frac{\pi D_p}{\lambda} \gg 1$ must be satisfied for it to be used, where D_p is the average particle diameter and λ is the peak wavelength emitted by the particles at the temperature of interest. Additionally, the model assumes all particles to be completely opaque, so it cannot be applied to transparent or partially transparent materials.

The radiation heat transfer between two particles is given by the equation for re-radiating surfaces.

$$\dot{Q}_{rad}^{(i,j)} = \frac{\sigma \left(T_i^4 - T_i^4\right)}{\frac{1-\epsilon_i}{\epsilon_i A_i} + \frac{1}{A_i F_{i\to j}} + \frac{1-\epsilon_j}{\epsilon_j A_j}} \tag{3.22}$$

A similar equation applies for heat transfer between a particle and a wall due to radiation.

The view factors between the particles and other particles and particles and walls are determined using a Monte Carlo method. For every particle, a number of rays are fired from the particle from a random location on its surface in a random direction and the first particle or wall they intersect with is recorded. The view factors between a particle and any other particle or wall are then given by the ratio of the number of rays fired from the first particle

that intersect the second particle or wall to the total number of rays fired from that particle.

The Marsaglia rejection method [34] is used to pick a random point on the surface of a particle from which to fire a ray. This method allows a point on a sphere to be randomly selected without the use of trigonometric functions. Two uniform random numbers, x_1 and x_2, between -1 and 1, are selected and the sum of their squares computed. If the sum of squares is greater than 1, the set is discarded and two new numbers are selected. If it is less then 1, x, y, and z coordinates of a random point on the sphere can be calculated from the pair using algebraic manipulations [34].

$$x = 2x_1\sqrt{1 - x_1^2 - x_2^2} \tag{3.23}$$

$$y = 2x_2\sqrt{1 - x_1^2 - x_2^2} \tag{3.24}$$

$$z = 1 - 2\left(x_1^2 + x_2^2\right) \tag{3.25}$$

Once a point on a particle is chosen, a coordinate shift is then applied and centered about that point to align the z-direction with the outward facing normal. Then, the direction of the fired ray is selected by choosing a random point on the unit sphere centered at the point chosen on the particle. The Marsaglia rejection method [34] is used again with an additional rejection criterion applied that the chosen point must have a non-negative z-component to ensure that a point on the outward facing hemisphere is chosen. Finally, the vector determined by connecting the chosen point on the surface of the

particle with the chosen point on the outward facing unit hemisphere is shifted back to the original coordinate system [79].

3.2.1.4 Uncertainty Quantification:

Uncertainty in the model prediction is due to three different sources: input uncertainty, bed generation uncertainty, and consolidation uncertainty. Input uncertainty is due to the uncertainties in the material properties passed to the model as inputs. These are gas conductivity, solid particle conductivity, Young's modulus, Poisson Ratio, and solid density. Bed generation uncertainty is due to the inherent randomness in the process used to generate the powder beds. Since the initial positions of the particles when they enter the domain are random, the final resulting powder bed structure once the particles settle is also random. Consolidation uncertainty occurs because the degree of consolidation in a given real powder bed is unknown. Consolidation occurs when particles in a powder bed are re-arranged to give a more compact structure and commonly occurs as the result of a pressure being applied to the bed and then released or the bed being shaken. Consolidation results in a decrease in the porosity of a powder bed and thus changes the effective thermal conductivity.

In order to assess the impact of input uncertainties, the generalized polynomial chaos framework, as discussed previously, is employed to estimate the probability distributions of the model outputs due to the uncertainties in the inputs. Bed generation uncertainties are estimated by generating multiple different random powder bed configurations and averaging the calculated

effective thermal conductivity across all of them. The resulting standard deviation is then a measure of the uncertainty in the model prediction due to the randomness of the powder bed.

Consolidation uncertainties are estimated by lowering the top boundary of a powder bed to the point where it overlaps with the top layer of particles by a small amount (on the order of the particle radius). The resulting forces then cause the powder bed to re-arrange itself into a more compact structure. Finally, the top boundary is raised again to relieve any stresses that could not be relieved by particle re-arrangement. The effective thermal conductivity is then calculated for the unconsolidated powder bed as well as for four different consolidated beds produced by lowering the top boundary by different amounts. Results are averaged across all five beds and a standard deviation calculated. This standard deviation is an estimate of the uncertainty due to the unknown degree of bed consolidation, or, equivalently, the unknown porosity.

3.2.2 Model Validation

3.2.2.1 Model Validation for Metal Powders

In order to assess the impact of finite bed depth, polydispersity, and high temperatures on the effective thermal conductivity of powder beds, the model is first validated against data available in the literature for metal particles. Cheng and Vachon [9] obtained experimental data for both steel of an unknown alloy and lead particles at room temperature, Bala et al. [3] measured the effective thermal conductivity of copper particles at room temperature, and

Widenfeld et al. [65] presented data for steel particles of an unknown alloy at approximately 30°C. Monodisperse particle beds are generated for each material in a cubic domain 10D on each side. This is determined to be large enough that further increasing the size of the domain has negligible effect on the results. Table 3.3 shows the data from these three sources compared against the predictions of the current model. k_{model} is the effective thermal conduc-

Table 3.3: Comparison of Model Predictions with Experimental Data

Material	D_p (mm)	k_{model} (W/m.K)	σ_{model} (W/m.K)	k_{exp} (W/m.K)
Copper	0.25	0.627	0.051	0.652 [3]
Copper	0.15	0.576	0.061	0.546 [3]
Lead	1.6	0.457	0.022	0.418 [9]
Steel	1.0	0.333	0.022	0.34 [65]
Steel	3.2	0.397	0.022	0.4-0.6 [9]

tivity predicted by the model, σ_{model} is the standard deviation of the model prediction and k_{exp} is the reported experimental effective thermal conductivity.

Table 3.4 shows the material properties used for the three different metals and Table 3.5 shows how many particles are in the beds generated for each of the five cases along with the corresponding average porosity across the different levels of consolidation. The standard deviation of the porosity is included to show the degree of uncertainty in the porosity as a result of consolidation. In each case, particles are added to completely fill the domain. Young's modulus, particle conductivity, and gas conductivity are represented

as uniform probability density functions for the purposes of calculating input uncertainty. Uniform probability density functions are chosen to capture the high degree of uncertainty in the steel alloys being used and the exact temperature experiments are run at.

The other inputs (density and Poisson ratio) are either well known or determined to have little impact on the calculated effective thermal conductivity and thus are assumed to be fixed values.

Table 3.4: Model Input Parameters

Material	k_s (W/m.K)	k_g (W/m.K)	E (GPa)	ν	ρ (g/cm^3)
Steel	12.11-45.0	0.025-0.027	190-206	0.28	7.7
Copper	393-409	0.025-0.027	110-128	0.34	8.96
Lead	34.24-36.36	0.025-0.027	13.8-16	0.44	11.36

Table 3.5: Particle Count and Porosity

Material	Num. of Particles	Avg. Porosity	Std. Dev.
Steel (1mm)	1039	0.41	0.01
Steel (3.2mm)	1090	0.418	0.009
Copper (0.25mm)	1095	0.415	0.009
Copper (0.15mm)	1091	0.416	0.008
Lead (1.6mm)	1093	0.416	0.009

Table 3.6 shows the input and consolidation uncertainties calculated for each material. Input uncertainties represent the standard deviation in the output due to all uncertain inputs. Bed generation uncertainty is calculated for 1 mm steel particles averaged across eight powder beds, and the resulting standard deviation is 0.002 W/m.K. As this is an order of magnitude less than the largest source of uncertainty, bed generation uncertainty is neglected for the remaining cases. The input and consolidation uncertainties are added in

Table 3.6: Input and Consolidation Uncertainties

Material	D_p (mm)	σ_{input} (W/m.K)	σ_{cons} (W/m.K)
Copper	0.25	0.009	0.05
Copper	0.15	0.008	0.06
Lead	1.6	0.008	0.02
Steel	1.0	0.01	0.02
Steel	3.2	0.02	0.01

quadrature to yield the values shown in Table 3.3 for the total uncertainty. As can be seen from Table 3.3, the model shows good agreement with the experimental results as all but one case is within one standard deviation of the predicted value and all cases are within two.

Figure 3.17 shows the variation of the particle bed temperature between the two fixed temperature walls for 1mm steel particles. Since particles are modeled using a lumped capacity method, no temperature gradient is maintained in the particles. Thus, the temperature variation in the bed is calculated using a binning method. The domain is divided into ten bins based on loca-

tion. All particles whose centers lie within a given bin have their temperatures averaged together to give an average temperature for the bin. These average temperatures are then plotted against bin location to give a temperature profile. As can be seen, this bin-averaged temperature profile is approximately linear.

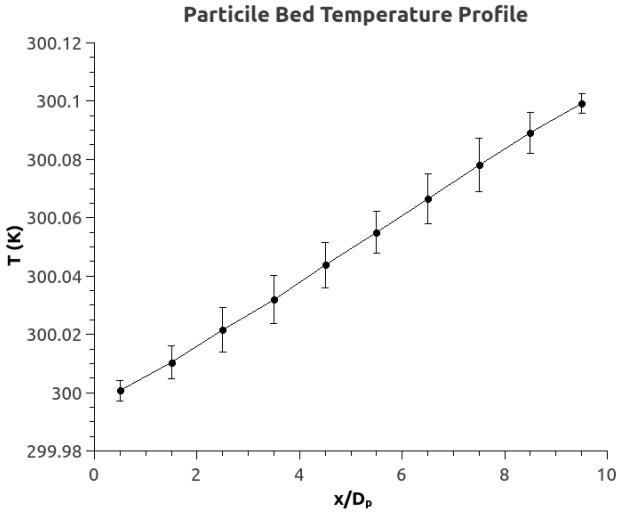

Figure 3.17: Particle Bed Temperature Profile

3.2.2.2 Model Validation for Ceramic Powders:

Model predictions are also validated for ceramic particles against the data of Slavin et al. [54] for packed alumina particles in helium. We find that if the procedure described for metallic particles is used for ceramic particles, predicted effective thermal conductivity deviates from the measurements by 30%. This is likely due to either the actual particles not being near-spherical, as is assumed in the model, the importance of surface roughness, or the as-

sumed Hertzian contact mechanics not being a good approximation of the actual contact behavior in ceramic beds. Therefore, calibration parameters are introduced. The first parameter allows the contact area between two particles to be adjusted by scaling Equation 3.17. The new contact radius is then given by Equation 3.26.

$$R_{c,e} = A_c \left(\frac{3 k_N l_{i,j} R_e}{4 E_e} \right)^{1/3} \tag{3.26}$$

The second parameter is the minimum conduction distance, l_{min}, which impacts Equations 3.20 and 3.21. It removes the singularity that occurs when particle-fluild-particle conduction is calculated. For metals, the default MFiX value of $1\mu m$ works well, but for ceramics it is used as a calibration parameter.

Taken together, A_c and l_{min} allow the relative importance of particle-particle and particle-fluid-particle conduction to be adjusted. These parameters are calibrated using the data of Slavin et al. [54] for temperatures up to 550K by means of a Levenberg-Marquardt least squares algorithm [47]. The calculated parameter values are $A_c = 5.981$ and $l_{min} = 2.419 \times 10^{-5} m$. Since A_c is larger than 1 and l_{min} is larger than $1\mu m$, this means that particle-particle contact conduction plays a larger role in the heat transfer than is predicted by the default MFiX-DEM model parameters.

The calibrated model is then validated against the alumina data for the remaining temperatures measured by Slavin et al. [54], 550-750K. At the first temperature, 337K, model input uncertainty is estimated using the same method as for metals, with the material properties of alumina given by Ta-

ble 3.7. The calculated standard deviation due to input uncertainty is 0.02

Table 3.7: Alumina Material Properties

Property	Value
k_s (W/m.K)	22.7-26.0
E (GPa)	344.8-409
k_g (W/m.K)	0.160-0.166
ν	0.21
ρ (g/cm^3)	3.95

W/m.K. Averaging across different random powder bed structures produced a bed generation uncertainty of 0.02 W/m.K and averaging across consolidated and unconsolidated beds yielded an average porosity of 0.403 with a standard deviation of 0.008 and a consolidation uncertainty of 0.5 W/m.K. Therefore, since consolidation uncertainties are an order of magnitude greater than other uncertainties, only consolidation uncertainty is considered at all other temperatures. The predicted conductivities and the experimental results are shown in Figure 3.18, where the uncertainty bars represent two standard deviations. As can be seen, the measurements fall within the model uncertainties for all data points. Thus, the model can be used to predict the thermal conductivity of ceramic powder beds as well as metal ones, but calibration is necessary.

3.2.3 Model Predictions

The model is then used to assess the effect of several parameters on the thermal conductivity of metal powder beds. Monodisperse, 1 mm steel par-

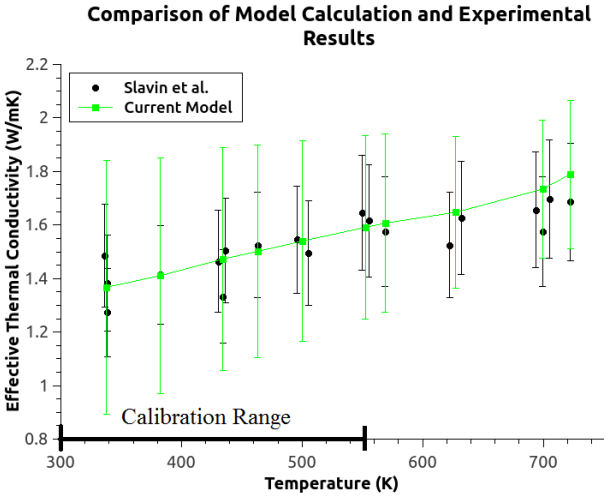

Figure 3.18: Comparison of Model Predictions with Experimental Results of Slavin et al. [54]

ticles with a bed height of 10 particle diameters, a bed temperature of 300K ($\frac{\sigma T^3 D_p}{k_g} = 0.06$), and properties given in Table 3.4 are used as an example material in all the following investigations unless otherwise indicated. Uncertain properties are taken to be exactly at the mean value and uncertainties in the outputs are thus due entirely to consolidation uncertainty.

3.2.3.1 Effect of Bed Temperature

First, the effect of bed temperature is examined. In SLM builds using metal powders, temperatures greater than 1000K are common and radiation heat transfer is expected to play a large role in the effective conductivity. In order to assess this, the bed temperature is increased while all other inputs except the gas conductivity are held constant. As gas conductivity varies with

temperature and most SLM builds are done in air, the gas conductivity is set to be the conductivity of air at the operating temperature. The relation $k_g(W/m.K) = 6.566\times10^{-12}T^3 - 3.386\times10^{-8}T^2 + 9.426\times10^{-5}T + 7.505\times10^{-4}$, obtained from curve fitting a cubic polynomial to the thermal conductivity of air for temperatures ranging from 175-1900K, is used. The effective thermal conductivity is then calculated for each case. At each temperature, the model is also run with the radiation module switched off for comparison. The results are shown in Figure 3.19. Radiation begins to play a significant role in the

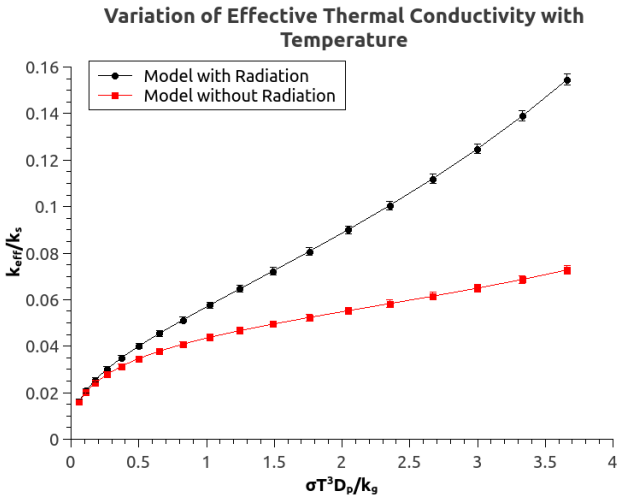

Figure 3.19: Variation of Effective Thermal Conductivity with Temperature

heat transfer for ratios of $\frac{\sigma T^3 D_p}{k_g}$ greater than 0.5. For the steel particles used in the model, this corresponds to a temperature of about 1000K. For particles on the order 0.1 mm this will be around 1300K in air and for 0.01 mm particles this will be almost 3000K. Thus, radiation heat transfer will need to be considered in the effective thermal conductivity when performing SLM

with metals or other similarly high melting point materials with particle sizes on the order 0.1 mm or above. For smaller particles, the material will likely melt before radiation heat transfer becomes significant. Additionally, even at higher temperatures, the conductivity of the powder is one to two orders of magnitude smaller than that of the solid, indicating that conduction is limited by the contact between the particles and may thus be significantly increased because of the parallel path provided by radiation at higher temperatures.

3.2.3.2 Effect of Gas Conductivity

The model is then similarly used to examine the effect of interstitial gas conductivity. Although some SLM builds may be performed in a vacuum or near vacuum, most commonly they are conducted in air or nitrogen at atmospheric pressure. Thus, the gas conductivity contributes to the overall effective thermal conductivity through the particle-fluid-particle ($\dot{Q}_{pfp}$) conduction pathway. Particle-gas interactions are neglected. All other model inputs are held constant and the gas thermal conductivity is increased across a broad range of values and the effective thermal conductivity calculated. The thermal conductivity of the beds with the gas conductivity switched off is also calculated for comparison. The results are shown in Figure 3.20. As can be seen, the conductivity of the gas begins to have a significant effect around a $\frac{k_g}{k_s}$ ratio of 0.001 and becomes dominant as the ratio goes to 0.1. As most metals have a thermal conductivity on the order of 10-100 W/m.K and air and nitrogen have conductivity on the order to 0.01 W/m.K, gas conductivity will

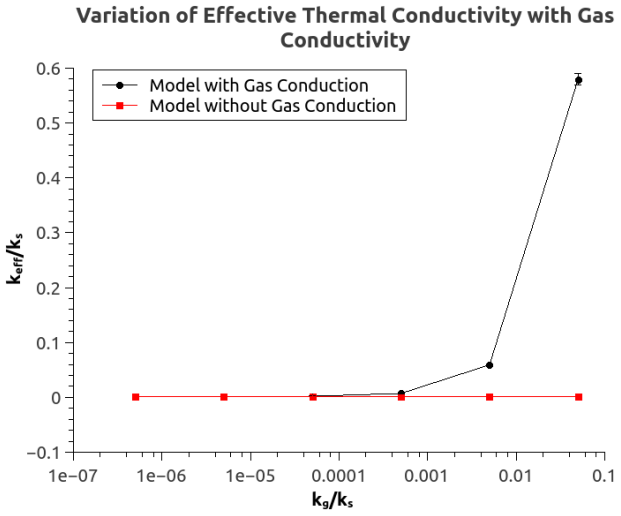

Figure 3.20: Variation of Effective Thermal Conductivity with Gas Conductivity

have to be considered when determining the effective thermal conductivity of SLM powder beds for some cases.

3.2.3.3 Effect of Young's Modulus

Next, the effect of the material's Young's modulus is considered by varying the Young's modulus while holding all other model inputs constant. The results are shown in Figure 3.21. The effective thermal conductivity is relatively insensitive to changes in Young's modulus, even when varied by several orders of magnitude. As most metals have a Young's modulus on the order of 100 GPa, variations in Young's modulus between materials would generally not have to be taken into account when determining the effective thermal conductivity of an SLM powder bed.

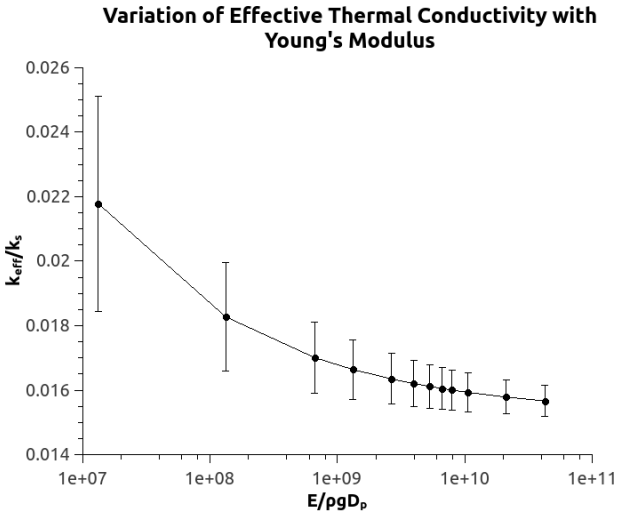

Figure 3.21: Variation of Effective Thermal Conductivity with Young's Modulus

3.2.3.4 Effect of Emissivity

The effect of emissivity is also considered by varying the emissivity between 0.1 and 1 while holding all other inputs constant. As emissivity only plays a role in the radiation calculation, the model is run at a temperature of 1000K, which corresponds to an $\frac{\sigma T^3 D_p}{k_g}$ of about 0.7, so that the impact of emissivity variations can be seen. The results are shown in Figure 3.22. As can be seen, the effective thermal conductivity is also not particularly sensitive to emissivity, even at temperatures where radiation heat transfer is significant. This can be explained by examining Equation 3.22. Since view factors between particles that can see each other are generally order 0.1, varying emissivity between 0.1 and 1.0 causes the radiative flux to vary at most by a factor of 3. As radiative flux only accounts for about 30% of the total flux at this

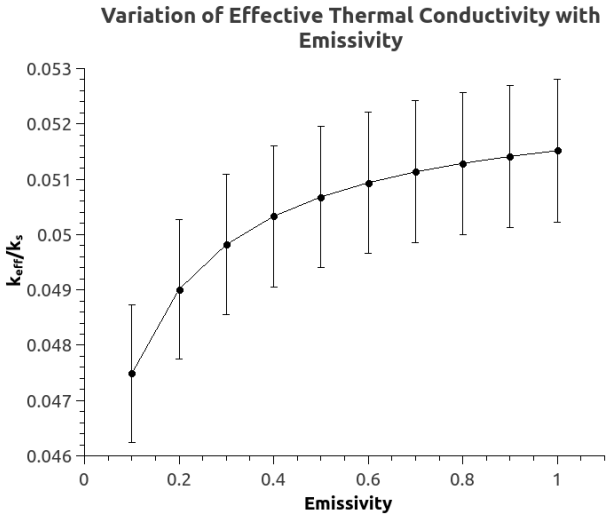

Figure 3.22: Variation of Effective Thermal Conductivity with Emissivity

temperature, the overall sensitivity to emissivity is low.

3.2.3.5 Effect of Bed Height

The effect of bed height is also examined as SLM machines use very thin layers during a part build and thus it is possible for a thin single powder layer to be spread on top of an already formed solid surface, resulting in a thin powder bed. In the model, this is simulated by discarding all particles which extend above a certain height in each powder bed geometry and then calculating the effective thermal conductivity while holding all other parameters constant. The results are shown in Figure 3.23. For very thin beds, on the order of a particle diameter, the effective thermal conductivity can be almost cut in half. However, this effect diminishes quickly and by bed heights of 6-8 particle diameters the conductivity is within the uncertainty of the infinitely deep

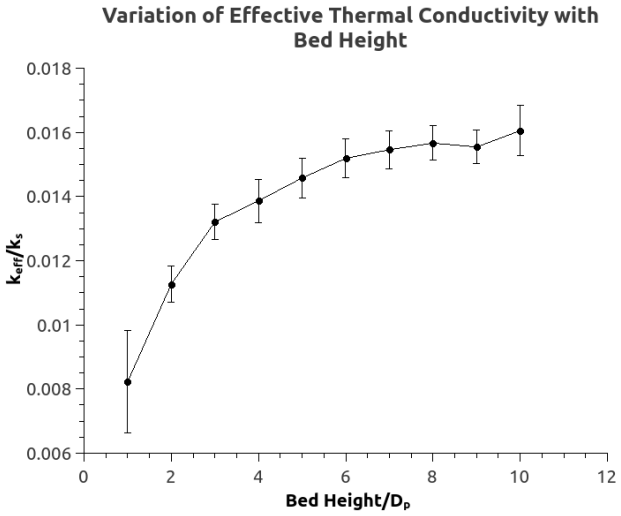

Figure 3.23: Variation of Effective Thermal Conductivity with Bed Height

bed value. Depending on the ratio of SLM layer thickness to powder particle diameter, bed height may play a role in the thermal conductivity of the powder for some applications.

3.2.3.6 Effect of Polydispersity

Finally, the effect of powder polydispersity is examined. In all previous simulations, the powder particles were assumed to have a uniform diameter. For real powder particles, however, this will generally not be the case and there will be some variation of particle diameter within the powder bed. In order to simulate the effect of powder polydispersity, packings are generated with particles of different sizes. When a particle is added to the domain, it is added at a random location with a random diameter. Although the model can be used to simulate other distributions, Gaussian particle size distributions

are assumed as only one additional input parameter (standard deviation) is introduced. The Gaussian distribution is split into nine bins, each with a representative diameter and a fraction of the total number of particles determined by the Gaussian. Particles entering the domain are then assigned one of the nine possible diameters based on the probability of each. Table 3.8 shows the average porosity and standard deviation due to consolidation on the polydisperse powder beds.

Table 3.8: Porosity of Polydisperse Beds

σ	Avg. Porosity	Std. Dev.
$0.05D_p$	0.423	0.007
$0.125D_p$	0.419	0.007
$0.25D_p$	0.421	0.007
$0.375D_p$	0.415	0.007
$0.5D_p$	0.428	0.007

Once the polydisperse beds are generated, the effective thermal conductivity of each is calculated using the same method as for monodisperse beds. The effect of polydispersity on the calculated conductivity can be seen in Figure 3.24, with the x-axis being the standard deviation of the particle diameter distribution normalized by the average particle diameter. There is about a 30% increase in the effective conductivity across the investigated range of standard deviations. This is likely due to the fact that the smaller particles in the distribution are able to fill in the gaps in the packing structure, leading

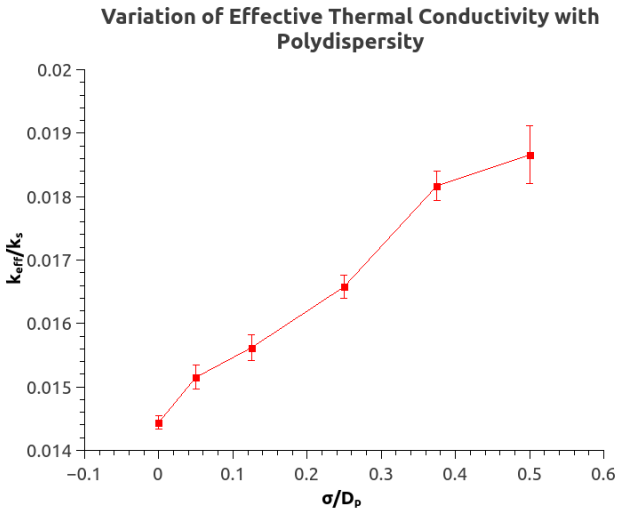

Figure 3.24: Variation of Effective Thermal Conductivity with Particle Size Standard Deviation

to more contact between particles. Thus, polydispersity can impact the conductivity of a powder bed, even for small deviations, although the impacts are not as large as those caused by gas conductivity or temperature. The uncertainties due to consolidation also increase with increasing standard deviation as the variation in particle size adds extra degrees of freedom to the powder bed layout.

3.2.4 Discussion and Empirical Relation

Of the parameters investigated, effective thermal conductivity is most dependent on temperature and gas conductivity. At low temperatures and low gas conductivities, conduction is primarily through the particle-particle path and thus is contact controlled. However, as temperature increases or gas

conductivity increases (either as a result of temperature increase or due to the use of a higher conducting gas), parallel paths are provided for heat transfer through radiation and particle-fluid-particle conduction. Temperature and gas conductivity, therefore, have the largest impact of the effective conductivity as they control the availability of these parallel pathways. Thus, an empirical correlation is developed to estimate the effective conductivity based on these quantities. A 2nd order polynomial expansion is developed and the coefficients determined using collocation points calculated from a Smolyak sparse grid [55]. Temperature and gas conductivity are non-dimensionalized as $\theta = \frac{\sigma T^3 D_p}{k_s}$ and $\kappa = \frac{k_g}{k_s}$. The correlation is then given by Equation 3.27.

$$\frac{k_{eff}}{k_s} = -2.44\theta^2 + 15.2\theta\kappa + 3.57\theta - 25.2\kappa^2 + 11.7\kappa + 0.001 \tag{3.27}$$

The correlation is developed for a θ range of 0.00035-0.023 (representing 500K-2000K for 1mm steel particles) and a κ range of 0.00125-0.006. Material properties for monodisperse 1mm steel particles were used for all other inputs. However, since variations in emissivity between 0.1 and 1.0 only lead to approximately an 8% change in conductivity even at high temperatures and variations in Young's modulus across several orders of magnitude only produce a 2% change in conductivity, the correlation should be applicable to a wide range of metals. Polydispersity up to $0.5D_p$ can lead to a change in conductivity of 30% and bed heights less than $6D_p$ lead to 100% changes. Therefore, for highly polydisperse powders and very thin beds this correlation cannot be used and the full model must be employed directly. Degree of bed consol-

idation is found to be the dominate uncertainty in calculating the effective thermal conductivity, leading to a model uncertainty of up to 11%.

3.3 Melt Model

For closure in the bed-scale thermal model (Equation 2.1), a relationship between the enthalpy of the powder and the temperature is given by Equation 2.2, which introduces the temperature-melt fraction function of the powder, $g_p(T)$.

$g(T)$ relations are typically calculated for bulk materials by measuring the temperature-enthalpy relationship for the material, $H(T)$. Sharp changes in the slope of the $H(T)$ curve are used to identify the temperatures at which phase change begins and ends [5], and linear relations used to estimate the melt fraction when the temperature is between the two [60]. This method assumes a homogeneous material and uniform melting within a sample. As powdered materials are not homogeneous, finite rate transport effects are critical in determining the rate of powder melting and thus the $g_p(T)$ relation. By simulating the melting of a powder at the particle scale, the $g_p(T)$ relation can be calculated and applied in the bed-scale thermal model.

A number of groups have modeled the SLM process on the particle scale. Korner et al. [31] developed a 2D lattice Boltzmann model of the melting of metal powder in SLM. Gurtler et al. [20] used a 3D volume of fluid method to model the melting process capable of simulating multiple laser passes. Khairallah and Anderson [27] developed a high resolution SLM model considering a

number of phenomena. However, to our knowledge no groups have used the results from a particle-scale SLM simulation to calculate a temperature-melt fraction relationship for use in a bed-scale model.

3.3.1 Bed Generation

Powder bed melt behavior is modeled using a hybrid continuum-discrete approach. The initial positions of the powder particles before the laser is applied are determined using the discrete element method (DEM), as described in Section 3. Once the particles settle, their positions and properties are used as an input for the melting model. The particle packing structure is placed on top of a finite volume mesh. For each mesh cell, the volume of overlap with each of the particles is calculated. The total volume of intersection with all the particles determines the volume faction, β, of solid material in that cell. Cells that are completely contained within a particle have solid volume fractions of 1.0. Cells not overlapping with particles at all have solid volume fractions of 0.0 and cells partially overlapped with particles have solid volume fractions between 0.0 and 1.0. In this way, the DEM representation of the particle bed is converted to a mesh representation that serves as an initial condition for the melting model. Figures 3.25 and 3.26 show a packing structure in both the DEM and mesh representations.

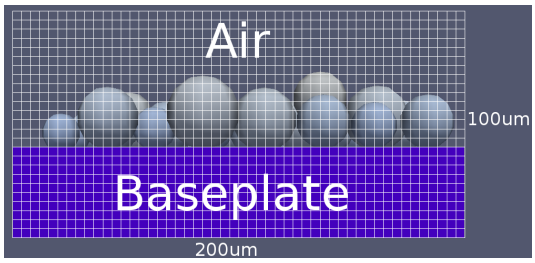

Figure 3.25: DEM particles placed on background mesh

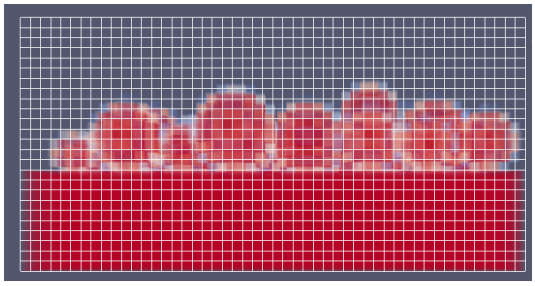

Figure 3.26: Particle volume fractions on background mesh corresponding to DEM particles. Particles, base plate and air are included in the simulation

3.3.2 Fluid Model

The melting model is a multiphase system consisting of three components: solid metal, liquid metal due to the melting of the particles from the laser, and a background gas. The motion of the system is modeled using a modified volume of fluid (VOF) method. The VOF method considers each mesh cell to contain a mixture of solid, liquid, and gas moving at a single mixture velocity. The mixture velocity is calculated using a form of the Navier-Stokes equations [25].

$$\frac{\partial \gamma \rho_m}{\partial t} + \nabla \cdot (\gamma \rho_m u_m) = S \tag{3.28}$$

$$\frac{\partial \gamma \rho_m u_m}{\partial t} + \nabla \cdot (\gamma \rho_m u_m u_m) = -\gamma \nabla P + \nabla \cdot (\gamma \tau) + \rho_m g + F_s - \epsilon \frac{(1-\gamma)^2}{\gamma^3} u_m \tag{3.29}$$

Here, γ is the volume fraction of the fluid, defined as 1.0-β, u_m is the mixture velocity, ρ_m is the mixture density, S is the source term due to melting, P is the pressure, τ is the fluid stress tensor, g is the gravitational acceleration and F_s is the surface tension force. The $\epsilon \frac{(1-\gamma)^2}{\gamma^3} u_m$ term is a momentum sink that drives the velocity of the mixture to zero in cells that are fully solid.

The fluid volume fraction, γ is calculated explicitly based on the initial distribution of solid material and the melting process discussed later. γ represents the volume fraction of each cell that is empty of solid material and thus available to contain gas or liquid metal. An additional variable, α, is necessary to track the fraction of this available volume that contains liquid metal. The remaining fraction (1-α) contains gas. The distribution of α in the mesh is

evolved using the VOF advection equation [59].

$$\frac{\partial \gamma \alpha}{\partial t} + \nabla \cdot (\gamma u_m \alpha) = S \tag{3.30}$$

F_s, the surface tension force in Equation 3.29, is calculated using the curvature of the liquid meniscus, using the volume fraction [59].

$$F_s = -\sigma \nabla \cdot \left(\frac{\nabla \alpha}{|\nabla \alpha|} \right) \nabla \alpha \tag{3.31}$$

σ is the surface tension coefficient between the air and liquid metal. σ is calculated per cell based on the temperature, allowing for the Marangoni effect due to gradients in surface tension to be simulated.

Equations 3.28, 3.29, and 3.30 are solved sequentially at each time step using the OpenFOAM finite volume solvers [43] to evolve the mixture velocity and liquid volume fraction fields. The mixture properties required for the equations (ie. ρ_m) are calculated by volume averaging using the liquid volume fraction field and the properties of the pure materials: $\rho_m = \alpha \rho_l + (1.0 - \alpha)\rho_g$, where ρ_l and ρ_g are the densities of the pure liquid and gas respectively.

3.3.3 Thermal and Melting Model

Heat transfer is accomplished using the enthalpy formulation of the energy equation.

$$\frac{\partial H_m}{\partial t} = \nabla \cdot (k_m \nabla T) + f(x, y, z, t) \tag{3.32}$$

This equation is the same as the one used in the bed-scale continuum model of the process (Equation 2.1), except that now the mixture enthalpy is used.

Similar to how mixture properties are determined for the fluid flow equations, H_m may be calculated using the solid, fluid, and liquid volume fraction fields: $H_m = (\beta + \gamma\alpha)H_{metal} + \gamma(1.0 - \alpha)H_{gas}$. The relation may now be closed using known relationships between the temperature and enthalpy of the metal and gas.

$$H_{metal} = (1 - g_{metal}(T)) \int_{T_{ref}}^{T} \rho_{metal} c_{metal,solid} dT + g_{metal}(T) \int_{T_{ref}}^{T} \rho_{metal} c_{metal,liquid} dT + g_{metal}(T) \rho_{metal} L_{metal} \quad (3.33)$$

$$H_{gas} = \int_{T_{ref}}^{T} \rho_{gas} c_{gas} dT \quad (3.34)$$

A similar relationship is used for the enthalpy due to vaporization of the solid material.

Note that Equation 3.33 is similar to Equation 2.1 for the volume-averaged enthalpy of the powder. Here, however, $g_{metal}(T)$ is a property of the bulk metal, not a volume averaged effective property of a powder. Unlike for powders, the temperature-melt fraction relationship for bulk metals can be accurately approximated using a step function for pure elements or a lever rule between a solidus and liquidus temperature for alloys [60].

The energy equation is solved iteratively using the enthalpy method outlined by Swaminathan and Voller [60] in the OpenFOAM finite volume solver until the temperature and enthalpy fields are consistent. Finally, those cells containing metal whose temperatures cross the melting point of the metal

are converted to solid or liquid, as appropriate, by explicitly updating the solid and fluid volume fraction fields (γ and β) and generating a source term for the VOF equation to update α, the liquid volume fraction field. For cells undergoing vaporization, sink terms are generated for the VOF and energy equations to remove the vaporized material and associated enthalpy. However, as vaporization is assumed to occur quickly in comparison to the melt flow dynamics, the location of vaporized material is not tracked and is assumed to immediately exit the domain.

3.3.4 Radiation Model

Radiation is modeled using the radiation transport equation (RTE).

$$\nabla \cdot (I(\vec{x}, \vec{s})\vec{s}) + a_m I(\vec{x}, \vec{s}) = a_m \frac{\sigma T^4}{\pi} \tag{3.35}$$

$I(\vec{x}, \vec{s})$ is the radiation intensity field, a_m is the mixture absorptivity, and σ is the Stefan-Boltzman constant. The mixture absorptivity is calculated using the volume fraction fields: $a_m = (\beta + \gamma\alpha)a_{metal} + \gamma(1.0 - \alpha)a_{gas}$.

The RTE requires additional discretization within the finite volume mesh, as the intensity field is a function of not only spatial location, but also direction. This discretization is done using the discrete ordinates method [39] in which the unit sphere is divided into a finite number of solid angles. The intensity field for each solid angle is solved for sequentially using the OpenFOAM finite volume solver and iterated until the fields are consistent. Once the intensity field is calculated, a source term is generated for the energy

equation.

$$f(x, y, z, t) = a_m(G - 4\sigma T^4) \tag{3.36}$$

G is the sum of the irradiation field over all of the solid angles.

The irradiation due to the laser is handled as a boundary condition to the RTE at the topmost boundary of the domain. The irradiation due to the laser is given by Equation 3.37.

$$I = \frac{2\epsilon P}{\pi\omega^2} e^{\frac{-2r^2}{\omega^2}} \tag{3.37}$$

ϵ is the emissivity of the metal, P is the laser power, ω is the characteristic radius, and r is the distance between the center of the laser and a given point on the boundary. The laser intensity is integrated over each cell on the boundary and applied as a fixed-value boundary condition in the RTE. As the laser beam is taken to be entering straight downwards into the domain, the boundary condition is applied only to those solid angles for which $\vec{s} \cdot \vec{n}$ is approximately -1. The causes the laser intensity to propagate down into the domain.

3.3.5 Results

In order to assess the ability of the melting model to accurately predict SLM melt pool geometries, simulation results are compared to experimental results for 316L stainless steel and Ti-6Al-4V for both flat plates and powders.

For all simulations, a domain size of $200\mu m$ x $200\mu m$ x $100\mu m$ is used consisting of 50x50x25 mesh cells, for a total of 62,500 cells. In order to assess mesh independence, a simulation is run for $27\mu m$ average diameter 316

stainless steel particles for one packing structure under a 200W, $54\mu m$ beam diameter laser on a 50x50x25 mesh and a 100x100x50 mesh. Material properties used are given in Table 3.9. Calculated melt pool heights and widths differed by less than 1% between the two meshes and calculated maximum temperatures differed by less than 5%. As these uncertainties are smaller than other sources of uncertainty in the simulation, the 50x50x25 mesh is considered sufficient resolution. Also, as $54\mu m$ is the smallest beam diameter used and $27\mu m$ the smallest average particle diameter, this resolution is deemed sufficient for all cases.

Simulations are run for enough time to allow the laser to move in the x-direction from an initial x-position of $25\mu m$ to a final x-position of $175\mu m$. Thus, simulation times are given by $150\mu m/v_l$, where v_l is the laser speed. Time-stepping is controlled dynamically. At each time step, the Courant number is calculated at the face of each mesh cell using the fluid velocity field and the current time step size. The time step size is then adjusted such that the maximum Courant number in the domain does not exceed 0.5. Time step sizes are limited to a maximum of $1\mu s$ to adequately resolve the laser motion when no melt is present and thus the Courant number is zero everywhere. Once melt begins to form, time step sizes are forced down into the nanosecond range to limit the Courant number.

3.3.5.1 Laser Irradiation of Stainless Steel Plate

Gusarov et al. [22] measured the melt pool depth and width on a 316L stainless steel plate due to laser irradiation. They used an SLM machine to run a laser with different powers and speeds over a flat, stainless steel, plate with no powder. The resulting melt pool geometry was measured by observing the change in micro-structure in the melted and re-solidified regions.

In order to compare to Gusarov's results, simulations are conducted using a domain consisting of only blocks of air and solid stainless steel, with no super-imposed particles. Material properties for 316 stainless steel are given by Khairallah et al. [27, 28] and summarized in Table 3.9. The emissivity of

Table 3.9: 316 Stainless Steel Material Properties

Property	Value
Density	7.43 g/cm^3
Viscosity	6.42 g/s m
Surface Tension	3.282-8.9e-4T N/m (T in K)
Thermal Conductivity	20.0 W/m K
Specific Heat	320.3 + 0.379T J/kg K (T in K)
Emissivity	0.3-0.6 (uniform random)
Latent Heat	270 KJ/kg
Solidus Temperature	1648 K
Liquidus Temperature	1673 K

the plate is given as a uniform probability distribution as opposed to a fixed value, as this is an uncertain input. Surface impurities and finish have a large

impact on the emissivity of metals and this range represents the set of possible values for stainless steel.

Table 3.10: Laser Properties for Stainless Steel Plate Calculations [22]

Property	Case 1	Case 2
Power	25 W	50 W
Speed	15 cm/s	30 cm/s
Beam Diameter (FWHM)	50-60 μm (uniform random)	50-60 μm (uniform random)

Table 3.10 shows the laser parameters used by Gusarov in the two cases simulated. In both cases, the laser beam diameter is given as a uniform probability distribution based on the uncertainties Gusarov measured on the laser used [22].

Using material emissivity and laser beam radius as the uncertain inputs, simulations are conducted to compute the probability distributions of the output melt pool width and depth. Once the PDFs are determined, a 90% confidence interval is calculated. This is done by integrating the PDFs from highest probability density to lowest probability density until a total probability of 90% is reached. The 90% confidence interval thus represents the region in which the true value is most likely to lie given the uncertainty in the inputs.

Figures 3.27, 3.28, 3.29, and 3.30 show the calculated PDFs of the melt pool width and depth for the two different laser power and speed combinations along with the 90% confidence interval and the value measured by Gusarov.

As can be seen, the measured value falls within the 90% confidence interval for all the cases, indicating that the model is able to account for measurements taken given the uncertainties. However, uncertainties in the simulation are fairly large due mainly to a large uncertainty on the emissivity of the plate. A measurement of the emissivity of the plate taken before an experiment would reduce that uncertainty significantly and thus enable a better comparison.

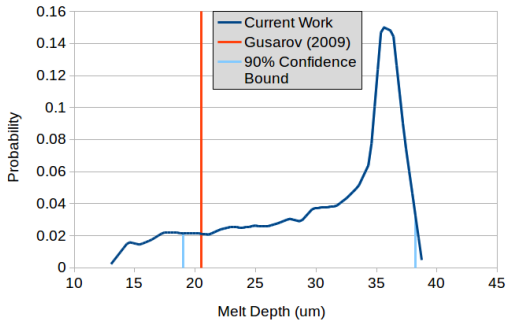

Figure 3.27: PDF of Predicted Melt Pool Depth for P = 25W and Speed = 15 cm/s

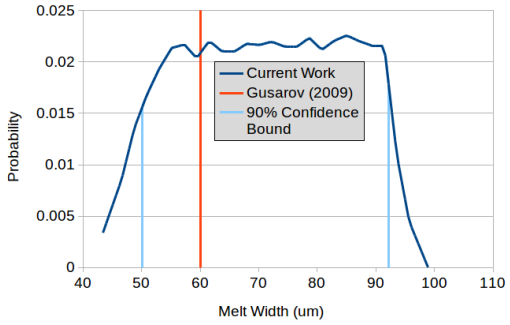

Figure 3.28: PDF of Predicted Melt Pool Width for P = 25W and Speed = 15 cm/s

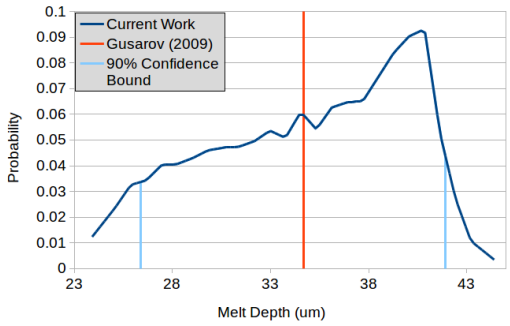

Figure 3.29: PDF of Predicted Melt Pool Depth for P = 50W and Speed = 30 cm/s

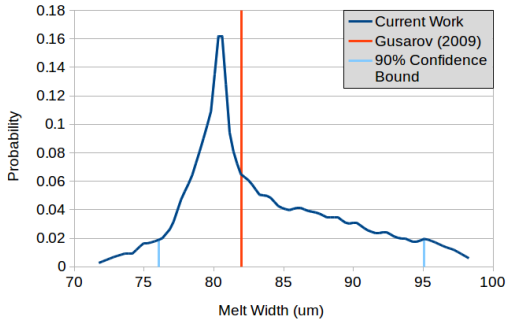

Figure 3.30: PDF of Predicted Melt Pool Width for P = 50W and Speed = 30 cm/s

3.3.5.2 Laser Irradiation of Stainless Steel Powder

Khairallah et al. [27] measured the height and width of a single melt track caused by a single laser scan line on a single layer of 316L stainless steel particles on top of a 316 stainless steel plate. In order to compare to Khairallah's results, a domain is initialized consisting of a stainless steel block and a block of air. The air block is filled in with a random packing of stainless steel particles using the method described in section 3. A laser scan is then simulated and the resulting melt track height and width calculated. The powder bed parameters used by Khairallah are a layer height of 40 μm and a Gaussian particle size distribution with average particle diameter of 27 μm and a standard deviation of 4.25 μm. The laser parameters are given in Table 3.11. The material properties of stainless steel are given in Table 3.9.

Table 3.11: Laser Properties for Stainless Steel Powder Calculations [27]

Property	Value
Power	200 W
Speed	2 m/s
Beam Diameter (4σ)	49-59 μm (uniform random)

Unlike in Gusarov [21], Khairallah specifies no uncertainty in the laser beam diameter, thus an error similar to Gusarov (10%) is assumed due to the similarity in the process. Additionally, since the material being irradiated is a powder and not a flat plate, the bulk material emissivity is converted to a

powdered material emissivity using the equation developed with the particle-scale optical model and given in Equation 3.38.

$$\epsilon_{eff} = 0.053 + 1.37\epsilon - 1.04\epsilon^2 + 0.399\epsilon^3 \tag{3.38}$$

Thus, the 0.3-0.6 emissivity uncertainty range transforms to a 0.38-0.59 range which is no longer uniformly distributed because of the non-linearity of Equation 3.38.

Using powder emissivity and laser diameter as uncertain inputs, simulations are conducted to compute the probability distributions of the output melt pool width and depth and a mean and standard deviation is calculated for each. However, an additional packing uncertainty is present due to the random nature of the powder bed packing structure. This is estimated by running 10 simulations at the mean value of emissivity and beam diameter with different powder bed structures. The standard deviations due to packing and inputs are summed in quadrature to produce an overall standard deviation. The calculated mean and standard deviations due to the different sources of uncertainty are shown in Table 3.12 along with Khairallah's measured values.

Table 3.12: Mean and Standard Deviations for Melt Track Height and Width of Stainless Steel Powder

Quantity	μ	σ_{input}	$\sigma_{packing}$	σ_{total}	Khairallah [27]
Width	$68.9\mu m$	$3.5\mu m$	$4.5\mu m$	$5.7\mu m$	$75\mu m$
Height	$25.9\mu m$	$2.8\mu m$	$4.7\mu m$	$5.5\mu m$	$26\mu m$

Assuming a Gaussian distribution for the result of the combined PDFs due to input and packing uncertainty, a 90% confidence interval is computed for both width and height and plotted along with Khairallah's measurements in Figures 3.31 and 3.32. As can be seen, the measurements fall within the

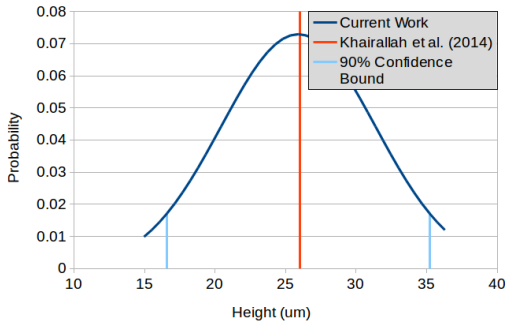

Figure 3.31: PDF of Predicted Melt Track Height for Stainless Steel Powder

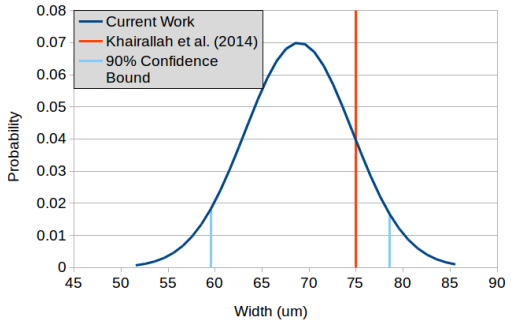

Figure 3.32: PDF of Predicted Melt Track Width for Stainless Steel Powder

model 90% confidence interval for both width and height. Also of note is the large uncertainty due to the powder packing. For both width and height, it is the dominant source of uncertainty. As the exact packing structure of a powder bed within an SLM machine cannot easily be determined, this indicates the

presence of a large uncertainty that cannot be eliminated. However, certain factors, such as compaction, may impact the magnitude of the uncertainty.

As powder in an SLM bed may be compacted as a result of the powder spreading process, the effects of compaction on packing structure uncertainty are examined. To do this, powder bed structures are generated using DEM as discussed previously. Then, after a structure is generated, a force is applied to the top boundary, lowering it until it contacts the top of the powder bed, thus applying a pressure to it. Once the powder particles stop moving in response to the applied pressure, it is released. The compacted structure is considered stable if the particles do not move significantly after the pressure is released. As SLM powder beds are not constrained from the top during a build, the maximum applied pressure which still generates a stable compacted structure is found and the resulting structure considered to be the most compacted that could realistically exist in an SLM machine. Ten of these structures are then generated, simulations conducted, and the variation in melt track width and height calculated. It is found that, for these compacted structures, the standard deviation of melt track width and height is reduced by almost half.

Thus, it can be concluded that the details of the powder packing can have a significant effect on the results and uncertainty estimate of a melting simulation. As Khairallah [27] only reports the results of a single experiment, it is impossible to determine the variation in the measured results due to packing and other uncertainties. A measurement of the powder bed emissivity directly prior to the experiment to reduce the uncertainty in emissivity and

multiple experimental runs to assess the effect of powder packing would allow a better comparison between simulation and experimental results.

3.3.5.3 Laser Irradiation of Ti-6Al-4V

Gong et al. [19] measured the melt pool geometry and melt track geometry for both a Ti-6Al-4V titanium alloy plate and a single track, single layer of powder due to a laser. The experimental and simulation set up for both the plate and powder titanium cases are similar to those used previously for stainless steel plates and powders.

The material properties of Ti-6Al-4V are given in [5] and summarized in Table 3.13. The laser parameters used for both the flat plate and powder are

Table 3.13: Ti-6Al-4V Material Properties

Property	Value
Density	4.47 g/cm^3
Viscosity	4.38 g/s m
Surface Tension	2.492-4.7e-4T N/m (T in K)
Thermal Conductivity	7.2 W/m K
Specific Heat	$573.7 + 0.157$T J/kg K (T in K)
Emissivity	0.1-0.475 (uniform random)
Solidus Temperature	1648 K
Liquidus Temperature	1673 K

given in Table 3.14. Like Khairallah, Gong gives no uncertainties on the laser beam diameter, so a 10% uncertainty similar to that of Gusarov is assumed.

Table 3.14: Laser Properties for Ti-6Al-4V Calculations [19]

Property	Value
Power	75 W
Speed	60 cm/s
Beam Diameter (4σ)	90-110 μm (uniform random)

Figures 3.33 and 3.34 show the calculated PDFs of the melt pool width and depth on a titanium flat plate along with the computed 90% confidence intervals and the measurements of Gong et al. [19]. Both measured values fall within the model's 90% confidence interval.

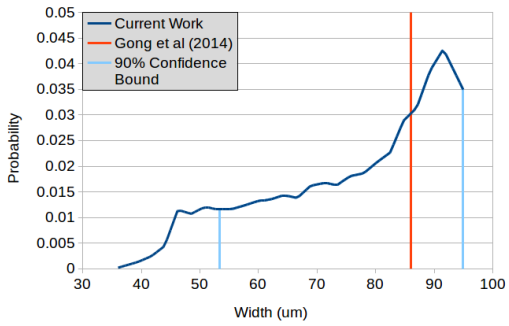

Figure 3.33: PDF of Predicted Melt Pool Width for Titanium Plate

For the powder case, Gong uses titanium powder with a Gaussian size distribution with a mean diameter of 38 μm and standard deviation of 7.9 μm. The layer thickness is 30 μm and the laser parameters the same as those used for the flat plate. Again, equation 3.38 is used to convert the emissivity of the solid titanium to that of a powder.

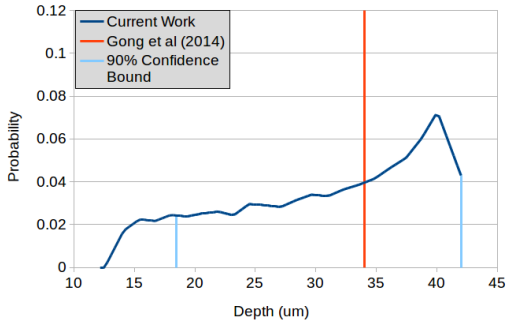

Figure 3.34: PDF of Predicted Melt Pool Depth for Titanium Plate

Table 3.15 shows the calculated mean and standard deviation of the melt track height and width due to the uncertainty in the emissivity, beam diameter, and the packing structure. Assuming a Gaussian distribution for

Table 3.15: Mean and Standard Deviations for Melt Track Height and Width of Titanium Powder

Quantity	μ	σ_{input}	$\sigma_{packing}$	σ_{total}	Gong [19]
Width	$82.1\mu m$	$13.9\mu m$	$6.5\mu m$	$15.4\mu m$	$91.8\mu m$
Height	$38.7\mu m$	$4.6\mu m$	$6.6\mu m$	$8.0\mu m$	$36.7\mu m$

the combination of the input and packing PDFs, a 90% confidence interval is calculated and plotted in Figures 3.35 and 3.36. As can be seen, both measurements from Gong fall within the 90% confidence interval. Similarly to the stainless steel cases, however, uncertainties in the simulation results are large due mainly to uncertainties in emissivity and, for the powder case, packing. A measurement of emissivity conducted prior to each experiment and multiple experimental runs would need to be conducted to enable to better

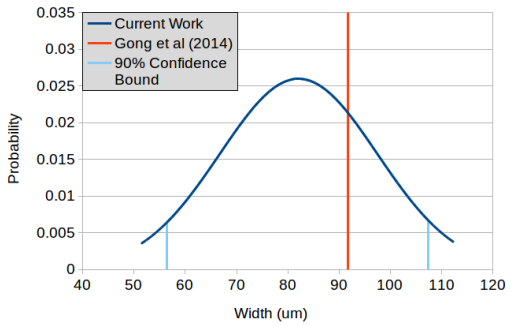

Figure 3.35: PDF of Predicted Melt Track Width for Titanium Powder

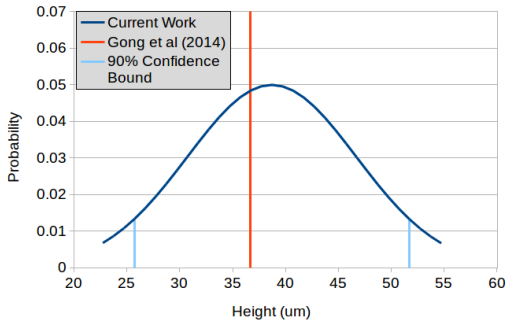

Figure 3.36: PDF of Predicted Melt Track Height for Titanium Powder

comparison between model and experiment.

3.3.5.4 Calculation of Temperature-Melt Fraction Curves

In order to demonstrate how a temperature-melt fraction curve can be calculated from the results of a powder melting simulation, a simulation is run with a 40 μm layer of powder. A 316L stainless steel powder is assumed. The particle diameter distribution is assumed to be Gaussian, with a mean of 27 μm and a standard deviation of 4.25 μm. The powder is placed on top of a 316L stainless steel substrate scanned with a 175 W laser at 2 m/s. Figure 3.37 shows the evolution of the material as it melts and re-solidifies.

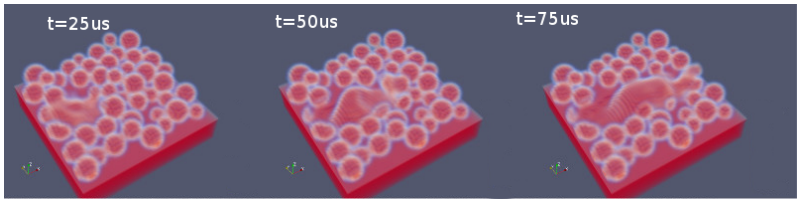

Figure 3.37: Melt Pool Evolution for Stainless Steel 175 W, 2 m/s

From the simulation results, a cubic domain element one layer thickness (40μm) on a side located in the center of the domain is considered. The temperatures of all the cells making up the element are volume averaged together to create an average temperature for the element at each time step. Similarly, the fraction of solid, un-melted material remaining $(1 - \frac{\beta}{\beta_0})$ is averaged over each cell in the element to create an average melt fraction for the element at each time step. The resulting curve is shown in Figure 3.38 along with the temperature-melt fraction curve of pure solid stainless steel.

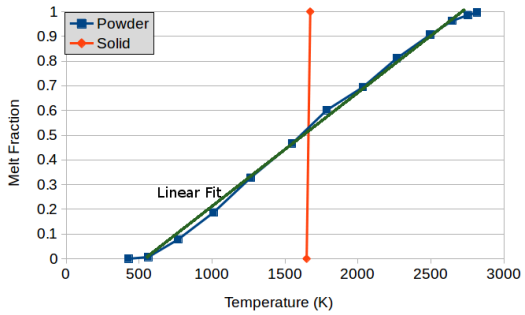

Figure 3.38: Average Melt Fraction vs Average Temperature for Solid and Powdered Material

For the bulk solid (red curve in Figure 3.38), the melt fraction-temperature curve is a straight line between the solidus and liquidus temperatures listed in Table 3.9. However, the powder behaves very differently. Since the powder heats up unevenly due to the laser, small amounts of melt form at very low average temperatures, as only the very top of the material has reached the melt temperature while the material below is significantly cooler. The melting process also takes much longer to occur as the melt forming at the top shields the remaining material from the laser heat. Thus, it can be seen that approximating the temperature-melt fraction curve of a powder with a simple linear relationship between the solidus and liquidus temperatures of the bulk solid material, as done in [14, 23], for example, would introduce significant errors in the melting behavior. For ease of use, we employ a linear fit to the average temperature-average melt fraction data from the powder melting calculation. This fit is shown on Figure 3.38. Comparing the linear fit to the melting calculation data gives a maximum fitting error committed of 4%.

However, a temperature-melt fraction curve calculated in this way will not necessarily be a constant material property of the powder. In addition to the material properties of bulk stainless steel, the curve may depend on the laser power, scan speed, element orientation relative to the laser path, and powder packing structure. Thus, the effect of variations in all of these parameters will be investigated.

The effect of variations in the distance of the element from the laser path is investigated by shifting the center of the domain element considered by different distances away from the center of the laser scan line. This accounts for the fact that some areas of the powder bed will not fall directly under the center of the laser as it passes by, but will instead be irradiated by a weaker portion of the beam. The difference in calculated melt fraction curves is shown in Figure 3.39 for distances of 5-25 μm. As the 4σ laser diameter is 54 μm, elements further away than 25 μm are not melted significantly. As can be seen,

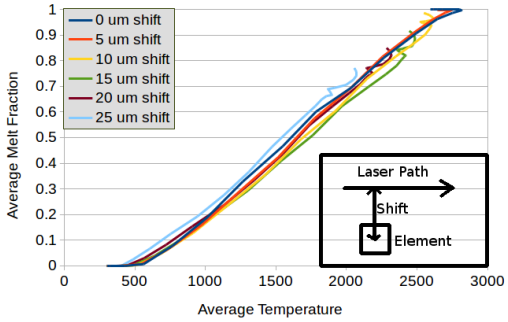

Figure 3.39: Average Melt Fraction vs Average Temperature for Domain Elements Different Distances Away from Laser Path

approximately the same curve is generated regardless of the element's distance

from the laser path, even for elements that do not fully melt. Performing a single linear curve fit on the set of data generated from all of the shifted elements yields a maximum error of 7% when calculating the melt fraction.

The effect of packing structure variation is investigated by running simulations with the same laser and material parameters ten different times with different powder packing structures and then calculating the average temperature-average melt fraction relationship for the same element location in the center of each bed. The difference in calculated curves is shown in Figure 3.40. Larger variations are caused by different packing structures than

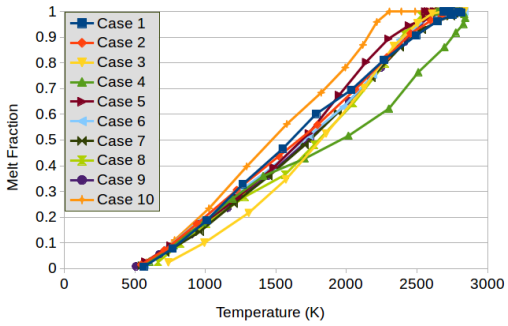

Figure 3.40: Average Melt Fraction vs Average Temperature for the Same Domain Element with Different Packing Structures

by different element positions. Using a single linear curve fit for all packing structures yields a maximum error of 19% when calculating the melt fraction.

The effect of laser power and speed variation is investigated by running simulations with various different laser powers and speeds on the same powder bed and calculating the temperature-melt fraction curves for elements directly under the laser path. Powers and speeds are chosen to cover a board range of

processing parameters that might be used in a single build. The difference in calculated curves is shown in Figures 3.41 and 3.42. Changing laser param-

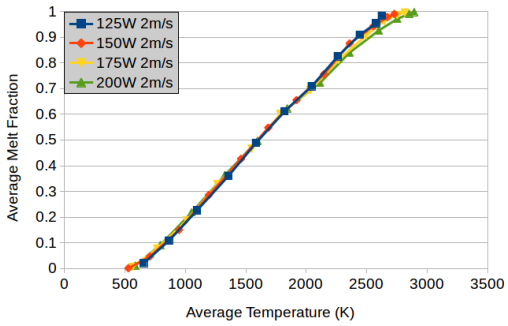

Figure 3.41: Average Melt Fraction vs Average Temperature for the Same Domain Element with Different Laser Powers

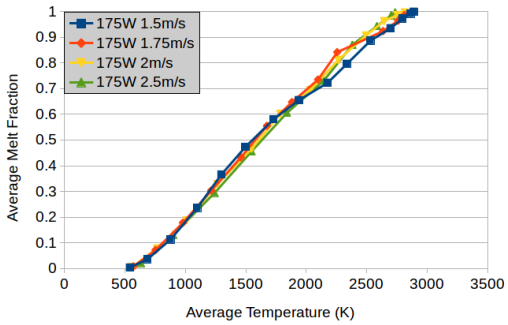

Figure 3.42: Average Melt Fraction vs Average Temperature for the Same Domain Element with Different Laser Speeds

eters causes a smaller variation in the melt fraction curves than changing the packing structure, and about the same level of variation as caused by distance away from the laser path. Using a single linear curve fit for all combinations of laser power and speed tested (125, 150, 175, and 200 W powers with 1.5, 1.75, 2, and 2.5 m/s speeds) gives a maximum error of 8% when calculating

melt fraction. Combining this with the errors due to distance from the laser path and packing structure in quadrature gives a total estimated uncertainty in melt fraction prediction of 22% when using a single curve to calculate melt fraction regardless of laser parameters, element position, or packing structure.

Although the overall uncertainty of 22% could be reduced somewhat by more advanced fitting procedures, it can be seen that the bulk of this uncertainty is due to powder packing structure, which cannot be reduced by better fitting. Thus, this uncertainty in melt fraction provides a way to estimate the uncertainty in bed-scale predictions due to particle effects that are neglected. The developed relationship is given in Equation 3.39.

$$g_p(T) = \frac{T - 520}{2220} \pm 0.22 \tag{3.39}$$

3.3.5.5 Bed-Scale Model Comparisons

As the goal of this work is to examine the effect of the temperature-melt fraction relationship on phase change in a bed-scale SLM model, two bed-scale calculations are done for 316 stainless steel powder with a 175W, 2 m/s, 54μm diameter laser. The results are compared to a particle-scale melting model which provides "ground truth." In the first calculation bed-scale, called the "bed-scale bulk material melting model," bulk material melting is assumed, with melting occurring between the solidus and liquidus temperatures for stainless steel (1648-1673 K) through a linear relationship between the melt fraction and temperature, as done in [60]. In the second bed-scale calculation, referred to as the "bed-scale powder melting model," the linear fit

to the melt fraction-temperature curve obtained from the particle-scale melt model is used. Intercepts with melt fraction equal to 0 and 1 are found, and correspond to temperatures of 520 and 2740 K respectively. The effective thermal conductivity of the powder used for the bed-scale simulations is 0.34 W/m K, calculated using the relation developed by Moser et al. [38]. The effective specific heat used is given by $(1-\epsilon)c_{p,steel} + \epsilon c_{p,air}$, where $c_{p,steel}$ is given in Table 3.9, $c_{p,air}$ is taken as 1005 J/Kg K, and ϵ is the porosity, taken to be 0.5. Material properties for the simulations aside from these are given by Table 3.9.

The bed-scale simulations are performed with a layer thickness of $40\mu m$ on top of a substrate consisting of already consolidated 316 stainless steel using an adaptive mesh. In this way, the area of the powder bed near the laser, where small-scale heat transfer effects are important, are resolved more finely than the substrate which is only undergoing conduction. The total domain size for both bed-scale simulations is 2.5cm x 5cm x 2.5cm with a mesh size varying from 2.56 mm to $20\mu m$ on a side. This is shown in Figure 3.43. The finest mesh size is chosen such that the difference in maximum temperature under the laser calculated in the domain varies by less than 5% with continued refinement ands yields a total of 168453 cells for the domain. The time step is chosen such that the laser moves at most one laser radius during a time step, or $13.5\mu s$ for a $54\mu m$ laser diameter moving at 2 m/s. The bed-scale simulations are run for a single scan line in order to compare to the results of the particle-scale melting model.

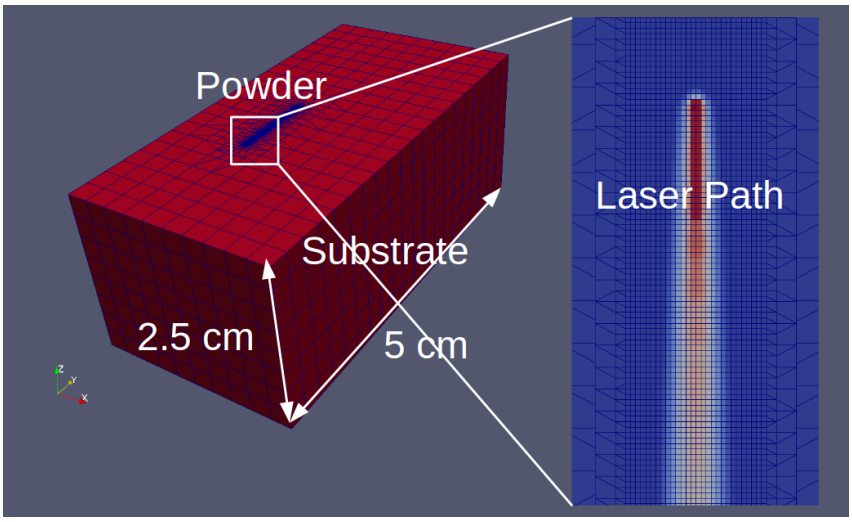

Figure 3.43: Domain for Bed-scale Simulations

These bed-scale simulations are compared with a particle-scale melting model. Particle-scale simulations are run with a $40\mu m$ powder layer of 316 stainless steel deposited using the DEM. The particle diameter distribution is Gaussian, with a mean of $27\mu m$ and a standard deviation of $4.25\mu m$, as used when calculating the temperature-melt fraction relation. The powder is placed on top of a 316L stainless steel substrate in a $200\mu m$ x $200\mu m$ x $100\mu m$ domain and scanned with a 175W, 2 m/s, $54\mu m$ diameter laser for $100\mu s$.

Finally, a $40\mu m$ mesh is superimposed on the results of a particle-scale melting model and the average melt fraction in each cell calculated for comparison to the bed-scale models. This is done for 10 different particle packing structure realizations and the results averaged across realizations. The resulting melt fraction predictions are shown in Figure 3.44. The bed-scale results have been cropped to show the relevant portion of the domain. The

cells marked 1,2 and 3 in Figure 3.44 all have the same centroid locations relative to the laser scan path and the same volume.

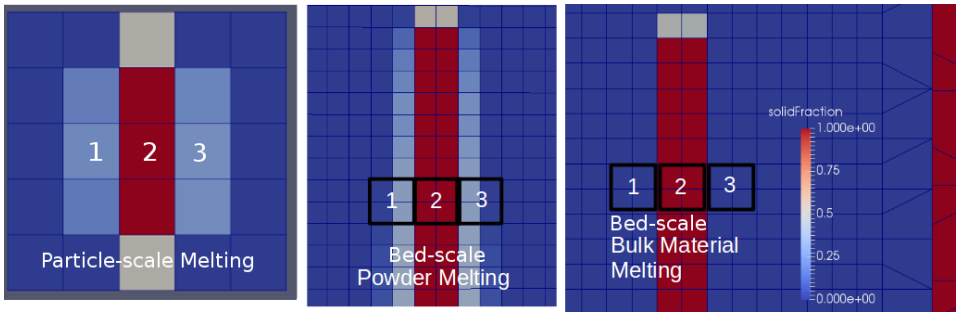

Figure 3.44: Comparison of solid fraction predictions using 1) Particle-scale melting model with mesh super-imposed 2) Bed-scale powder melting model, in which the $g_p(T)$ curve is computed from the particle-scale melt model 3) Bed-scale bulk material melting model, in which $g_p(T)$ assumes a bulk material with melting occurring between solidus and liquidus temperatures

To examine the difference between the approaches to melt prediction quantitatively, the calculated melt fraction for the cells or groups of cells marked as 1, 2, and 3 in Figure 3.44 are shown in Table 3.16. Cells in the center of the domain are chosen to avoid the effects of the domain boundaries and the beginning and end of the laser path. The error in Table 3.16 is defined as the difference between the melt fraction predicted by the particular bed-scale model and that predicted by the ensemble average of the 10 different realizations used in the the particle-scale melting model.

As can be seen, assuming that the melt properties of the powder are the same of that of the bulk leads to an under-estimation of the melt fraction in the cells not directly under the laser path. This is because the bulk melt properties

Table 3.16: Predicted Melt Fractions

Cell #	Particle-scale Model	Bed-scale Bulk	Bed-scale Bulk Error	Bed-scale Powder	Bed-scale Powder Error
1	0.28	0	0.28	0.27	0.01
2	1	1	0	1	0
3	0.25	0	0.25	0.27	0.02

do not properly account for partial melt in the powders since melting can only occur when enough energy has been input to raise all the powder in the cell above the solidus temperature.

On the other hand, using the bed-scale powder melting model allows the uneven melting of the powder to be approximated. The partial melt occurring at low temperatures is representative of the fact that some material closer to the laser may be above the melt temperature even though the average temperature in a cell is not. Using the bed-scale powder melting model, all the bed-scale melt fraction predictions fall well within the expected 0.22 melt fraction uncertainty. Additionally, this uncertainty estimate incorporates powder effects such as packing structure variation and quantifies the uncertainty introduced by these effects. In contrast, bed-scale modeling based solely on bulk material properties provides no clear method by which this can be accomplished.

3.4 Conclusions

Three particle-scale models of the SLM process are developed and implemented using MFiX-DEM and OpenFOAM. In the first, a ray-tracing technique is used to model particle-laser interactions and predict bulk optical properties, extinction and absorption coefficients, from the optical properties of the solid material. Calculated properties are in good agreement with previous computational models and experimental measurements. The variation of the bulk extinction and absorption coefficients with finite bed depth, solid absorptivity, laser spot size, and polydispersity is quantified. The largest variations occur with finite bed depth and solid absorptivity and correlations are developed for these scenarios.

In the second particle-scale model, the existing MFiX-DEM heat transfer modules are enhanced by the addition of a ray-tracing technique for particle-particle and particle-wall radiation. The model is used to calculate thermal conductivity of metal powder beds. Quantification of uncertainties in model inputs as well as bed layout and consolidation is included. The DEM model necessarily assumes beds made up of smooth, spherical particles. For metal powder beds, the assumption is good and calculated results are in good agreement with experimental data without the need for calibration. For ceramics, this is not the case, and calibration is necessary, but good agreement with experimental results is achieved after calibration of contact conduction and particle-fluid-particle models. The variation of the effective thermal conductivity with temperature, Young's modulus, gas conductivity, emissivity, finite

bed depth and polydispersity is quantified. As temperature and gas conductivity are found to have the most impact, a correlation is proposed to calculate the effective thermal conductivity from these two quantities for metal beds in air.

In the last particle-scale model, a melting model of an SLM powder bed is developed and implemented using MFiX-DEM and OpenFOAM. MFiX-DEM is used to generate particle packing structures. These are then converted to a mesh representation and imported into the OpenFOAM finite volume framework in which the model governing equations for fluid flow, heat transfer, and radiation are solved. Results from the model are compared against experimental measurements for stainless steel and titanium plates and powders undergoing laser melting in SLM and good agreement is obtained accounting for uncertainties in model inputs.

The model is then used to calculate effective, powder, temperature-melt fraction curves for stainless steel. The effects of variations in element position, packing structure, and laser parameters on these curves are examined and quantified. It is shown that using the melting properties calculated this way in a bed-scale model leads to better predictions of partial melting.

All particle-scale models provide methods to calculate bulk effective properties for powders that are difficult to obtain otherwise. Correlations for extinction and absorption coefficients, effective thermal conductivities, and temperature-melt fraction relationships are developed for certain materials and will be used in the following chapter in a bed-scale simulation. Just as

importantly, the particle-scale simulations allow the quantification of uncertainty at the particle level due to powder effects that is not possible with other methods.

Chapter 4

Bed-Scale Stress Model

In this chapter, the coupled bed-scale thermal-mechanical model is introduced for the prediction of residual stress in SLM parts. Models for predicting residual stress have been reported in the literature with varying degrees of complexity. Mercelis and Kruth [36] proposed a simple analytical model for predicting the residual stress in rectangular geometries assuming purely elastic deformations. Zaeh and Branner [76] and Li et al. [32] developed computational models for predicting residual stress relying on effective heat sources and effective stress profiles, respectively, neglecting the details of the laser motion in order to make faster predictions. Hodge et al. [23] developed a coupled thermal-mechanical model for the prediction of temperature and stress profiles during an SLM build with fully resolved laser motion using a J2 elastic-plastic material model. However, none of these works presented a quantitative uncertainty analysis and made only qualitative comparisons to experimental data.

The governing differential equations for the thermal model are the same as those used in Chapter 1. The mechanical governing equations for an elastic-plastic medium are developed. An adaptive finite volume discretization scheme is described and implemented in OpenFOAM. Bed-scale effective properties

are calculated using the particle-scale models from Chapter 3. The residual stress in a single layer of consolidated powder is predicted and compared to the experimental data of Yadroitsava et al. [73]. The thermal boundary condition imposed on the bottom boundary of the domain is found to have a large impact on the resulting solution, and a parameter sweep is done to determine an appropriate value for this parameter. Uncertainty quantification is performed based on the expected variability in the powder porosity, which is found to contribute to a large uncertainty on the residual stress prediction.

4.1 Governing Equations

For small strains, total strain can be decomposed into elastic, plastic, and thermal components [41], as shown in Equation 4.1.

$$\boldsymbol{\epsilon} = \boldsymbol{\epsilon}^e + \boldsymbol{\epsilon}^p + \boldsymbol{\epsilon}^t \tag{4.1}$$

Thus, the strain increment, the change in strain over an increment of time, Δt, can also be decomposed, as given by Equation 4.2.

$$\Delta\boldsymbol{\epsilon} = \Delta\boldsymbol{\epsilon}^e + \Delta\boldsymbol{\epsilon}^p + \Delta\boldsymbol{\epsilon}^t \tag{4.2}$$

$\Delta\boldsymbol{\epsilon}^e$ is the elastic strain increment, $\Delta\boldsymbol{\epsilon}^p$ is the plastic strain increment, and $\Delta\boldsymbol{\epsilon}^t$ is the thermal strain increment. The thermal strain increment is given by Equation 4.3 [41].

$$\Delta\boldsymbol{\epsilon}^t = \int_{T_1}^{T_2} \alpha(T) dT \tag{4.3}$$

T_1 and T_2 are the temperatures at the beginning and end of the time increment and α is the coefficient of thermal expansion. $\Delta\boldsymbol{\epsilon}^e$ is related to the incremental

stress through Hooke's law for elastic, isotropic materials as given in Equation 4.4.

$$\Delta\boldsymbol{\sigma} = 2\mu\Delta\boldsymbol{\epsilon}^e + \lambda\boldsymbol{I}tr(\Delta\boldsymbol{\epsilon}^e) \tag{4.4}$$

λ and μ are Lamé's parameters for the material. This in turn can be expressed in terms of the total strain using equation 4.2.

$$\Delta\boldsymbol{\sigma} = 2\mu(\Delta\boldsymbol{\epsilon} - \Delta\boldsymbol{\epsilon}^p - \Delta\boldsymbol{\epsilon}^t) + \lambda\boldsymbol{I}tr(\Delta\boldsymbol{\epsilon} - \Delta\boldsymbol{\epsilon}^p - \Delta\boldsymbol{\epsilon}^t) \tag{4.5}$$

The stress increment is related to the displacement increment through Newton's law.

$$\rho\frac{\partial^2\left(\vec{\Delta u}\right)}{\partial t^2} = \nabla\cdot\Delta\boldsymbol{\sigma} \tag{4.6}$$

For the plastic strain increment, $\Delta\boldsymbol{\epsilon}^p$, a J2 plasticity model is employed. This model is based on the work of von Mises, who suggested that the yielding of metals is governed by the second invariant of the deviatoric stress tensor, denoted J2. The J2 plasticity model has been shown to accurately predict yielding in ductile metals, such as stainless steel. Additionally, it is defined by a smooth yield function that is easily implemented numerically [6]. Hodge et al. [23] implemented a J2 plasticity model in their SLM modeling work and were able to get qualitative agreement with experimental results.

In the J2 plasticity model, $\Delta\boldsymbol{\epsilon}^p$ is calculated by enforcing the inequality that the von Mises equivalent stress not exceed the yield strength.

$$\sqrt{\frac{3}{2}\boldsymbol{s}:\boldsymbol{s}} \leq \sigma_y \tag{4.7}$$

$\boldsymbol{s}$ is the deviatoric of the total stress, $\boldsymbol{\sigma} + \Delta\boldsymbol{\sigma}$, and σ_y is the yield strength of the material.

Finally, the model is closed by relating the strain increment to the displacement increment.

$$\Delta\boldsymbol{\epsilon} = \frac{1}{2}\left(\nabla\vec{\Delta u} + \left(\nabla\vec{\Delta u}\right)^T\right) \tag{4.8}$$

All domain boundaries are taken as zero stress except for the bottom boundary where the powder couples to the baseplate, where a zero displacement condition is used. For the stress model, $\boldsymbol{\sigma}$ is the output quantity of interest, α, λ, and μ are properties of the material and the temperature, T, provides coupling to the thermal model.

4.2 Implementation Details

The elasto-plastic governing equations are implemented into the OpenFOAM finite volume solver. However, due to limitations of the OpenFOAM solver, it is not possible to implement a fully implicit solution to the linear elastic problem. Equations 4.4, 4.6, and 4.8 combine to form an expression for the displacement increment.

$$\rho\frac{\partial^2\left(\vec{\Delta u}\right)}{\partial t^2} = \nabla\cdot\left(\mu\left(\nabla\vec{\Delta u} + \left(\nabla\vec{\Delta u}\right)^T\right) + \lambda\boldsymbol{I}tr\left(\nabla\vec{\Delta u} + \left(\nabla\vec{\Delta u}\right)^T\right)\right) \tag{4.9}$$

While the expression in Equation 4.9 is linear in $\vec{\Delta u}$, the discretization framework in OpenFOAM does not provide a mechanism for resolving all the coupling between the vector components implicitly. Therefore, a partially implicit

formulation is used in which the right hand side of Equation 4.9 is broken down into implicit and explicit parts. The implicit part is given by Equation 4.10 and the explicit part given by 4.11.

$$\nabla \cdot \left((2\mu + \lambda) \nabla \vec{\Delta u} \right) \tag{4.10}$$

$$\nabla \cdot \left(\mu \left(\nabla \vec{\Delta u} + \left(\nabla \vec{\Delta u} \right)^T \right) + \lambda \boldsymbol{I} tr \left(\nabla \vec{\Delta u} + \left(\nabla \vec{\Delta u} \right)^T \right) \right) - \nabla \cdot \left((2\mu + \lambda) \nabla \vec{\Delta u} \right) \tag{4.11}$$

The non-elastic components of the stress model ($\Delta \boldsymbol{\epsilon}^p$ and $\Delta \boldsymbol{\epsilon}^t$) are also handled explicitly. $\Delta \boldsymbol{\epsilon}^t$ does not depend on the displacement increment and is thus simply included as a fixed source term. $\Delta \boldsymbol{\epsilon}^p$, however, is calculated at each iteration using an elastic predictor-plastic corrector method.

First, a trial stress, $\boldsymbol{\sigma}^t$, is computed assuming a fully elastic response ($\Delta \boldsymbol{\epsilon}^p = 0$). Then, the von Mises equivalent stress, σ_e^t, is computed for each cell using Equation 4.7. For cells in which the inequality is not violated, the already computed fully elastic response holds and no update of $\Delta \boldsymbol{\epsilon}^p$ is made. For cells in which the von Mises equivalent stress exceeds the yield strength, a plastic strain increment is calculated to return the equivalent stress to the yield surface. A scalar plastic strain increment, Δp is calculated such that Equation 4.12 is satisfied.

$$\sigma_e^t - 3\mu \Delta p - \sigma_y = 0 \tag{4.12}$$

Then, $\Delta \boldsymbol{\epsilon}^p$ is calculated using Equation 4.13.

$$\Delta \boldsymbol{\epsilon}^p = \frac{3}{2} \Delta p \frac{\boldsymbol{s}^t}{\sigma_e^t} \tag{4.13}$$

Equation 4.5 is then used to update the stress increment for the next iteration and the solution iterated until the relative change in the displacement field with each iteration is below a prescribed tolerance.

The stress model also requires that Lamé's parameters, μ and λ, be specified for the powder and the air when these quantities are only well defined for a solid. To get around this, Lamé's parameters for air and powder are set to be 3 orders of magnitude smaller than the values for the solid material, as it is determined that reducing them further has little impact on the solution and slows down convergence. Thus, air and powder cells provide very little resistance to deformation and allow the solid cells they border to deform freely. Powder and air are also set to have thermal expansion coefficients of zero and arbitrarily large yield strengths so they do not undergo thermal expansion or plastic deformation.

4.3 Discretization

The problem domain is discretized using the same finite volume method as the bed-scale thermal model. However, the size of the spatial and temporal discretizations are controlled dynamically. Resolving the solution in the area of the domain directly under the laser requires a much finer mesh than in areas of the domain not exposed to the laser and simply undergoing conduction and deformation. Similarly, resolving the melt dynamics induced by the laser requires a much smaller time step than when the laser is switched off and the part is just cooling awaiting a layer addition or after build completion.

As the location of the laser in the domain is known beforehand, it is possible to predict where a finer mesh resolution will be required. At specified time intervals, all cells in the domain are checked to see if they will be impacted by the laser during the interval. Those cells that will be impacted are refined one level by dividing the single hexahedral cell into 8 child cells. This process is repeated recursively until all cells that the laser will impact have been refined to a specified finest refinement level. In order to ensure convergence of the solution, a 2:1 refinement rule is enforced in which cells are only allowed to border cells that are at most one level finer or coarser. Thus, refinement of certain cells may trigger additional refinements of cells that are not necessarily impacted by the laser such that the 2:1 rule is enforced.

At the same time, mesh coarsening is performed in regions of the domain not impacted by the laser where the fine-level mesh will no longer be needed. All cells that will not be impacted by the laser during the time interval are considered as candidates for coarsening. Coarsening occurs by re-incorporating 8 child cells back into the original parent cell from which they were split. However, in order to preserve the sharp interface between consolidated powder, loose powder, and air, cells are only allowed to be coarsened if all child cells contain the same material. Thus, a cell that contains 100% consolidated material can only be coarsened if the 7 other cells that were split from the same parent cell also contain 100% consolidated material.

4.4 Results

In order to test the ability of the stress model to accurately predict the residual stresses in parts produced using SLM, model results are compared to the experimental results of Yadroitsava et al. [73]. Yadroitsava measured experimentally the residual stress present in a single layer of 316 stainless steel powder melted onto a stainless steel substrate using SLM. The layer thickness used is $40\mu m$ and the size of the area being melted is 1cm x 1cm. Residual stresses were measured in directions parallel and perpendicular to the laser scan direction in the plane of the powder bed. Measurements are made at the center of the part, both at the bottom of the layer, near the substrate, and at the top, near the free surface [73].

In order to compare to Yadroitsava's results, simulations are conducted using a domain consisting of a single layer of stainless steel powder. The effective thermal conductivity of the powder used for the simulations is 0.34 W/m K, calculated using the relation developed in the particle-scale conductivity model and given by Equation 3.27. The remaining thermal properties for 316 stainless steel are given by Table 3.9 and are volume averaged with those of the background air based on the porosity of the powder bed, ϵ. Thus, the effective specific heat used, for example, is given by $(1-\epsilon)c_{steel} + \epsilon c_{air}$.

Mechanical properties are given by Hodge et al. [23]. As properties such as Young's modulus and yield strength are temperature dependent, polynomial curve fits are applied to Hodge's mechanical property values to create functions that can be used by the simulation. Mechanical properties used in

the simulation are summarized in Table 4.1. Laser parameters used in the simulation are chosen to match those used by Yadroitsava and are summarized in Table 4.2.

Table 4.1: 316 Stainless Steel Mechanical Properties

Property	Value
Young's Modulus	2.304e11 - 9.3795e7T Pa (T in K)
Coefficient of Thermal Expansion	1.2989e-5 + 8.4443e-9T - 2.8339e-12T^2 1/K (T in K)
Yield Strength	4.2094e8 - 6.004e5T + 3.9859e2T^2 - 0.1143T^3 Pa (T in K)
Poisson's Ratio	0.3

Table 4.2: Laser Properties for Stainless Steel Stress Calculations [73]

Property	Case 1
Power	50 W
Speed	10 cm/s
Beam Diameter (FWHM)	70 μm

Similar to the thermal properties, the mechanical properties of stainless steel are volume averaged with those of air using the porosity to calculate the effective mechanical properties for the consolidated powder. However, as the Youngs modulus and yield strength of air are not well defined and thus set to be three orders of magnitude smaller than those of steel, they are essentially zero. Thus, the porosity effectively scales the mechanical properties of steel to calculate the properties of the consolidated powder.

Porosity, however, can vary significantly within a powder bed depending on the packing structure of the underlying particles. In order to assess the possible variations in porosity, fifteen different $200\mu m$ x $200\mu m$ x $40\mu m$ powder beds are randomly generated using the DEM with particles of 27 μm average diameter and a standard deviation of 4.25 μm. The porosity is then measured in a $40\mu m$ cube in the center of each domain. The average porosity calculated across the fifteen different realizations is 0.63, with a standard deviation of 0.05.

The computational domain is meshed using a uniform mesh size of $10\mu m$. This is selected as further mesh refinement results in variations of less than 5% for the maximum value of both the temperature and stress solutions. Time step sizes are controlled based on the laser parameters such that the laser moves a distance of at most its own radius during a time step.

In order to save computational expense, the substrate on which the powder layer is melted is not modeled explicitly. Instead, a zero displacement boundary condition is enforced at the bottom of the powder layer for the stress-displacement solution. This is representative of the fact that the powder is being melted on top of a large, stiff baseplate.

A convective boundary condition is imposed on the bottom boundary for the thermal equation. The convection coefficient used in the boundary condition accounts for the contact resistance between the powder layer and the baseplate, a large thermal sink initially at ambient temperature, as well as the decrease of thermal gradient due to the heating of the plate near the

powder. A depiction of the domain with imposed boundary conditions domain is shown in Figure 4.1.

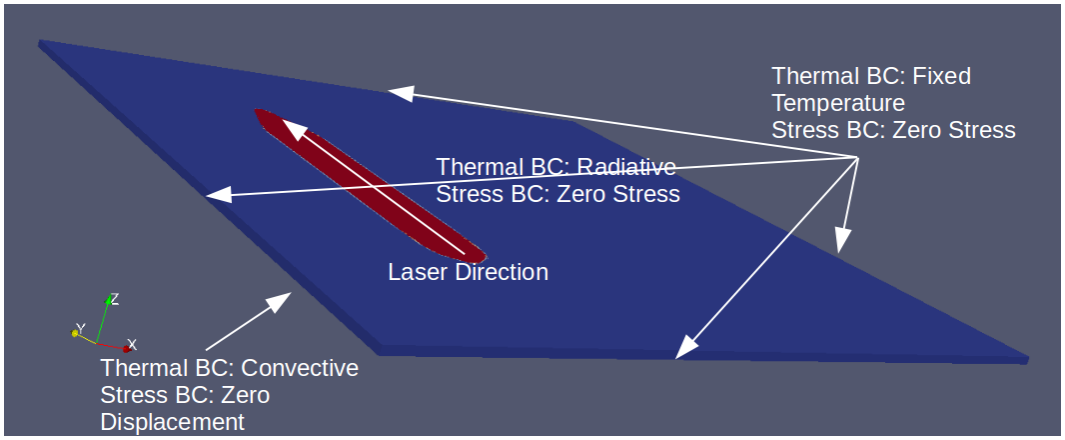

Figure 4.1: Simulation Domain with Boundary Conditions

While the thermal gradients in the baseplate could be modeled by including all or a portion of the plate in the simulation domain, the contact resistance cannot be readily estimated or measured. Thus, the convective coefficient on the bottom of the domain is a simulation parameter that cannot be easily set. Therefore, a parameter sweep is conducted to examine the effect of the convective coefficient on the predicted residual stress in the center of the domain for the nominal powder bed porosity of 0.63. The results are shown in Figure 4.2.

As is expected, changing the convective coefficient ceases to have an impact on the results once it gets above about O(10^8) W/m^2K. This value is high enough, given the mesh size, that the coefficient no longer poses an

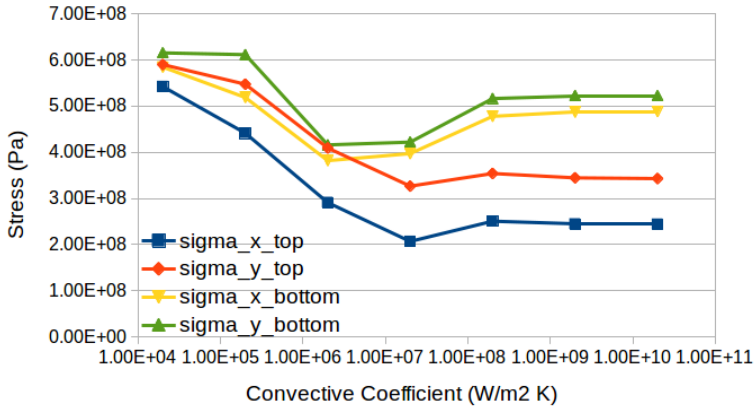

Figure 4.2: Residual Stress Results with Different Values of Convective Coefficient

impediment to heat flow from the boundary and thus no longer has an effect on the temperature solution.

However, prior to this leveling off, increases in the convective heat transfer coefficient lead to a decrease in the residual stress in both directions both at the top and bottom of the powder layer for smaller convective coefficients and an increase in residual stress for larger convective coefficients. This can be explained by examining the effects of the convective coefficient on the temperature profile. Figure 4.3 show the temperature profile of a portion of the domain 0.01 seconds after the laser has completed a scan line for two different convective coefficients. The first is for a coefficient of $2 \times 10^5 W/m^2K$ and the second is for a coefficient of $2 \times 10^6 W/m^2K$. As can be seen from Figure 4.2, in this case the higher convective coefficient leads to lower residual stress. As can be observed in the temperature profiles, a much higher temperature gradient along the surface of the bed exists for the lower convective coefficient. This is

because heat is not drawn out of the bottom of the bed as quickly and thus has an opportunity to diffuse outwards. These larger temperature gradients lead to larger residual stresses as the material deforms unevenly in response to different temperatures, leading to larger unbalanced stresses.

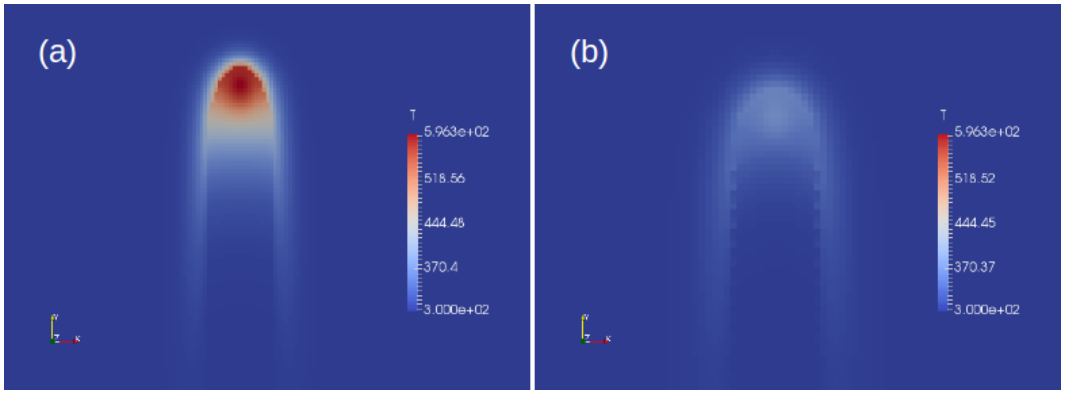

Figure 4.3: Temperature Profiles 0.01 Seconds After the Completion of a Scan Line for Convective Coefficients of (a) $2 \times 10^5 W/m^2K$ (b) $2 \times 10^6 W/m^2K$

Figure 4.4 show the temperature profile of a portion of the domain 0.01 seconds after the laser has completed a scan line for convective coefficients of $2 \times 10^6 W/m^2K$ and $2 \times 10^9 W/m^2K$. Figure 4.2 indicates that in this range, the larger convective coefficient generates larger residual stresses. As can be seen in the profiles, the bed with the higher convective coefficient has cooled faster, yielding lower temperatures at the same point in time. Faster cooling leads to larger residual stresses as the material does not have as much time to deform in order to accommodate the thermal stresses produced during cooling. Thus, the decrease and then increase of residual stress with convective coefficient shown in Figure 4.2 can be explained as a combination of two ef-

fects: higher convective coefficients allowing more heat to escape uniformly out of the bottom of the domain yielding more even cooling, followed by faster cooling not allowing enough time for deformation. Using these result, con-

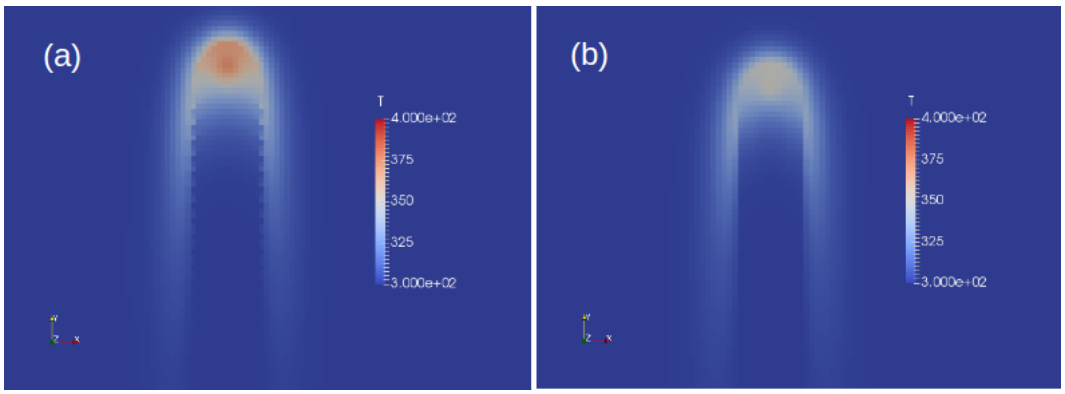

Figure 4.4: Temperature Profiles 0.01 Seconds After the Completion of a Scan Line for Convective Coefficients of (a) $2 \times 10^6 W/m^2K$ (b) $2 \times 10^9 W/m^2K$

vective coefficients on the order of $10^5 W/m^2K$ and $10^6 W/m^2K$ are found to produce residual stresses closest to those measured by Yadroitsava, and thus are selected as the possible boundary values for uncertainty quantification.

Aside from the unknown convective coefficient, significant uncertainties exist in the stress predictions as a result of the porosity variability. Thus, porosity is considered to be a Gaussian random variable with a mean of 0.63 and standard deviation of 0.05, based on the particle packing calculations discussed previously. Figure 4.5 shows how residual stresses vary with porosity over two standard deviations. As is expected, as porosity increases, residual stresses decrease as the consolidated powder effectively becomes less stiff. Additionally, the difference in residual stress between the bottom of the domain,

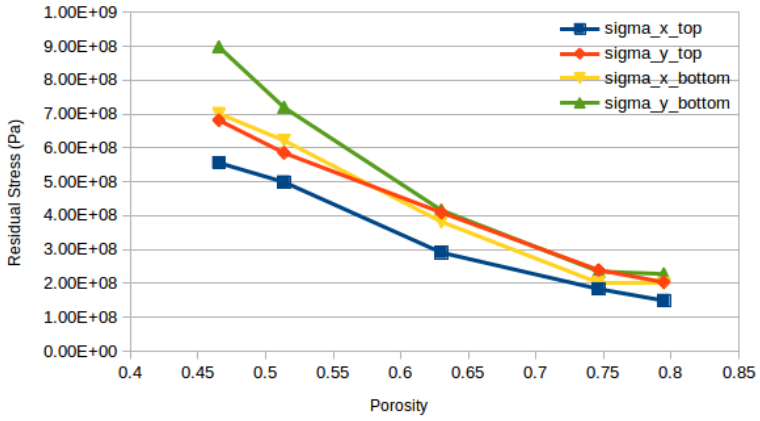

Figure 4.5: Residual Stress Results with Different Values of Porosity for Convective Coefficient of $2 \times 10^6 W/m^2 K$

near the plate, and the top of the domain, near the free surface, also decreases as a less stiff material means less of a stress gradient.

Simulations are conducted to predict the probability density of the residual stresses in the x and y directions both near the bottom and top of the layer at the center of the domain using the polynomial chaos method with a second order polynomial fit. Porosity is considered to be the dominant uncertainty in the system as it scales all of the mechanical properties of the material, causing larger variations than those due to the uncertainty in the mechanical properties of 316 stainless steel. Other parameters, such as thermal and laser input parameters, are held constant as well. Perturbations to these parameters are found to cause changes to the stress solution much smaller than those observed with porosity.

The resulting probability density functions are shown in Figures 4.7,

4.6, 4.9, and 4.8 for both convective coefficients selected. For each density function, 90% confidence intervals are computed using the most likely method in which the density function is integrated from highest probability density to lowest probability density until a total probability of 90% is reached. These confidence intervals are shown on each of the plots as well as the values measured by Yadroitsava for the residual stresses.

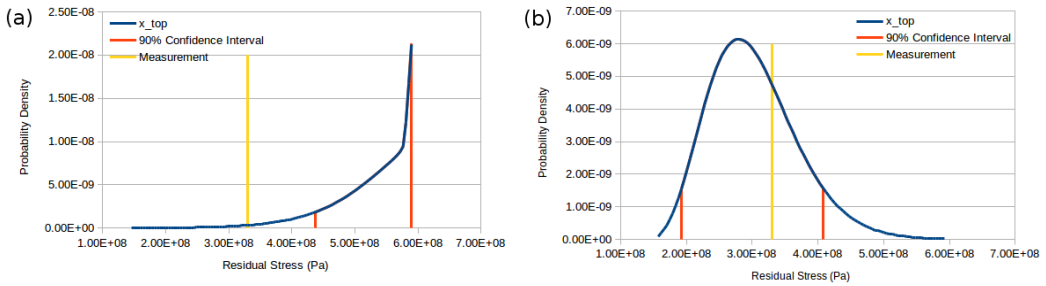

Figure 4.6: Probability Density Function of X-Direction Residual Stress Near Free Surface for Convective Coefficients of (a) $2 \times 10^5 W/m^2K$ (b) $2 \times 10^6 W/m^2K$

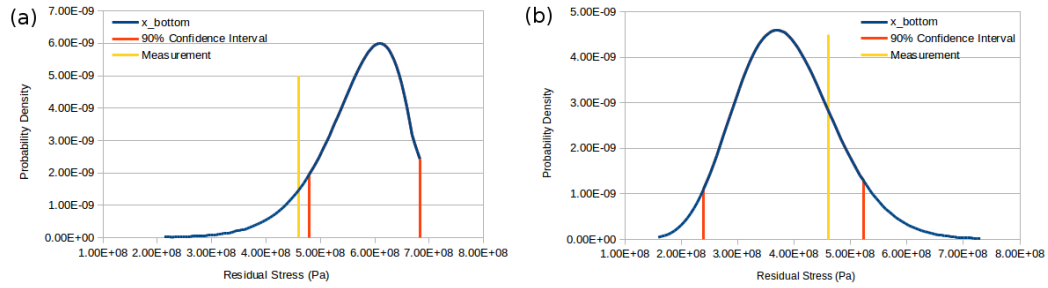

Figure 4.7: Probability Density Function of X-Direction Residual Stress Near Substrate for Convective Coefficients of (a) $2 \times 10^5 W/m^2K$ (b) $2 \times 10^6 W/m^2K$

As can be seen, for the convective coefficient of $2 \times 10^6 W/m^2K$, all the measured values fall within the 90% confidence intervals. On the other

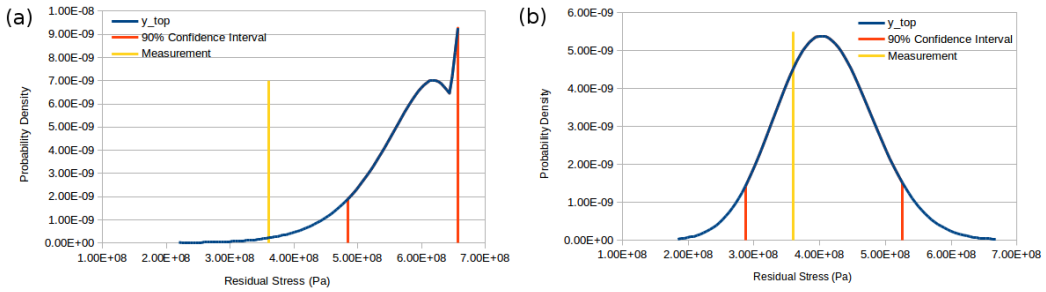

Figure 4.8: Probability Density Function of Y-Direction Residual Stress Near Free Surface for Convective Coefficients of (a) $2 \times 10^5 W/m^2K$ (b) $2 \times 10^6 W/m^2K$

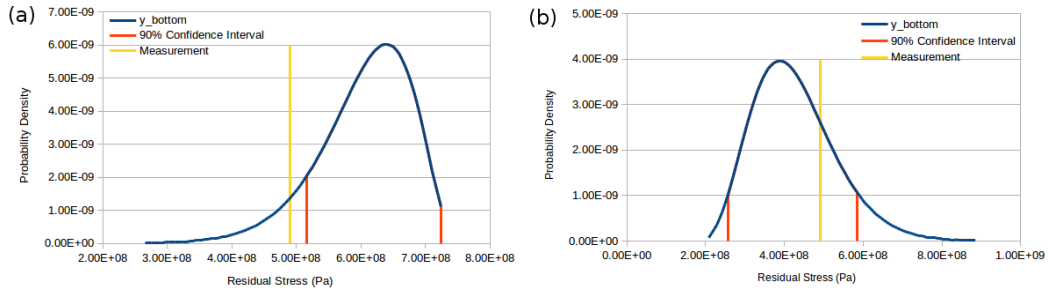

Figure 4.9: Probability Density Function of Y-Direction Residual Stress Near Substrate for Convective Coefficients of (a) $2 \times 10^5 W/m^2K$ (b) $2 \times 10^6 W/m^2K$

hand, a convective coefficient of $2 \times 10^5 W/m^2K$ results in the measurements falling outside the 90% confidence intervals for all cases. This indicates that the choice of convective coefficient has a significant impact on the capability of the model to make predictions in line with experimental data and that a convective coefficient of $2 \times 10^6 W/m^2K$ yields predictions that agree with the experimental results given the expected variability due to porosity. Although a more systematic calibration of the convective coefficient may be possible to bring the predicted means even closer to the experimental data, the large uncertainty due to porosity means that this would mostly be fitting to noise. For both convective coefficients tested, what is evident is the large uncertainty in residual stress that the variation in the porosity causes. The standard deviations of the residual stress predictions are on the order of 50% of the prediction. This indicates that the uncertainty in the porosity, a result of the random nature of the powder bed, introduces a large uncertainty in the stress calculation that makes precise predictions difficult.

Chapter 5

Conclusions and Future Work

Although computational modeling has been advanced as a possible solution to some of the challenges of SLM, particularly for predicting process outcomes as a result of input parameters, most existing models have focused on modeling the processing deterministically, without a quantification of uncertainty. This has precluded previous modeling efforts from making quantitative comparisons to experimental data and also make process variability prediction impossible.

The goal of this thesis was to develop a model of the SLM process that is capable of predicting a temperature and stress history of an SLM part with systematic uncertainty quantification. In order to do this, a multi-scale modeling framework with uncertainty quantification is introduced that applies systematic uncertainty estimation to identify the largest sources of uncertainty in bed-scale models and uses particle-scale modeling to predict and estimate uncertainties on input parameters that have the largest impact. In so doing, this thesis introduces a mechanism for using results and uncertainties from particle-scale models in larger bed-scale models.

5.1 Contributions of the thesis

Multi-scale modeling framework. An important contribution of the thesis is the development of a multiscale framework for the modeling of SLM processes. This multi-scale modeling framework presents a novel way of using detailed, particle-scale simulations to predict effective properties for bed-scale simulations of powder-based additive manufacturing processes. Additionally, it introduces rigorous uncertainty quantification into the SLM modeling process, and provides a means to transmit uncertainties at the particle scale into the bed-scale simulations. Without such a mechanism, no method currently exist with which to estimate the impact of particle-scale variations on the output of a bed-scale model.

Bed-scale thermal model. A preliminary bed-scale thermal model of the process is developed and is shown to contain large uncertainties due to poorly characterized effective powder bulk properties. Therefore, detailed powder-scale models are developed in order to predict these properties.

Particle-scale optical model. The DEM is used to generate random arrangements of spherical powder particles with any desired size distribution. Ray tracing is used to predict detailed laser-powder interactions to calculate effective extinction and absorption coefficients. For the first time, the impact of SLM-specific scenarios such as shallow bed depth, particle size distribution, and packing structure are considered and quantified. Correlations are devel-

oped for these scenarios to allow effective optical properties to be accurately set in bed-scale models. Uncertainties developed for these correlations include particle-scale effects, such as packing structure, thus providing a novel way for uncertainties to be propagated from the particle-scale to the bed-scale.

Particle-scale conductivity model. DEM heat transfer constitutive models are used to predict the effective thermal conductivity of powders. A novel ray-tracing based radiation heat transfer constitutive model is introduced, allowing the effects of high temperature on the effective thermal conductivity to be predicted. Other scenarios common in SLM are also considered for the first time, such as bed height and polydispersity. Correlations with uncertainty are developed, again including particle level effects that allow them to be propagated upwards into bed-scale models.

Particle-scale melting model. A hybrid DEM-continuum model is developed to model the melting behavior of metal powders. For the first time, a systematic uncertainty quantification is done for a detailed melting model, allowing quantitative comparison to experimental results, with which it is shown to agree within the estimated uncertainty. An effective temperature-melt fraction relation is also developed for the first time. The developed relation is shown to be an improvement over existing techniques for capturing the melting of powders at the bed-scale, as it better predicts partial melting. Again, uncertainties are developed for this relation, including particle effects, that can be propagated upwards into bed-scale models.

Bed-scale stress model. A coupled, bed-scale thermal-mechanical model is developed and implemented in OpenFOAM. A calibration parameter, the heat transfer coefficient between the powder bed and the baseplate, is identified as significantly impacting the results of the model. A parameter sweep is conducted to determine where the heat transfer coefficient value is likely to lie based on experimental results. Additionally, the variable porosity of the powder bed is identified as a significant source of uncertainty, resulting in a 50% uncertainty on the residual stress.

5.2 Future Work

Uncertainty Reduction. As powder packing structure has been identified as a significant source of uncertainty, future particle-scale modeling of powder deposition processes could provide further insight into how to characterize powder bed structures and possibly reduce the modeling uncertainty surrounding them.

Physical Model Improvements. The stress model used in this thesis was built around an elasto-plastic material model. This assumes small strains that can be decomposed into elastic, plastic, and thermal components. Additionally, it relies on material properties that are not well known or well defined at high temperatures and when the material is in the liquid phase. An improved, thermodynamic-based material model able to account for large deformations and phase change would improve the accuracy and utility of the stress model.

Improving Computational Time. The builds modeled in this work, even at the bed scale, are small compared to parts that are typically built using these processes, but still consume significant computational resources. In the thermal-mechanical model, solving for the mechanical response consumes most of the computational time. Performance could likely be improved by implementing a coupled block solver mechanism within the finite volume framework for the solution of the elastic-plastic equation. Such a solver could implicitly resolve the coupling between the vector components and remove the need to iterate in order to solve the linear problem. This, combined with a Newton solver to resolve the non-linearities could significantly improve performance. A finite element implementation could be used as well to resolve the vector components implicitly.

Even with this improvement, however, computational time is likely to continue to be a challenge. The main bottleneck is the number of computational grid cells needed to resolve the laser as compared to the overall size of the domain. Even with adaptive meshing, the number of required mesh elements is large and thus computationally expensive. Accurate, reduced-order models are needed for applications such as control and optimization which require many model evaluations.

Multi-scale property prediction. Phenomena such as micro-structure formation, which can have a large influence on part material properties, have not been considered as part of this work but are important considerations in order

to fully understand the possible variability in these processes. The multi-scale modeling framework introduced here could be extended in the future to include micro-structure and mechanical property models at the particle-scale that inform material properties at the bed-scale.

New materials. This thesis has focused on modeling the behavior of metal powders, and the techniques should be applicable to all powders that undergo melting during processing. However, some materials, particularly ceramics, are sintered together as opposed to melted. New particle-scale models that capture this sintering physics as opposed to the melt, flow, and solidification processes considered here would need to be developed to model these materials.

Experimental data. A challenge throughout this thesis has been the scarcity of experimental data. Collecting SLM data is an expensive and challenging process and, often, the data that can be collected is limited to a very small number of quantities of interest. However, recently, researchers have begun outfitting SLM machines with more instruments, including high speed thermal imaging cameras and optical coherence tomography. Such instruments introduce the ability to monitor temperature profiles and melt pool shapes while a build is in progress. Not only does this present opportunities for much more detailed model validation than has previously been possible, but also to use collected data to inform model predictions to increase accuracy and decrease variability.

Micro-SLM. All work done in this thesis has assumed geometric optic effects, meaning that particles are large compared to the wavelength of the lasers being used to process them. This assumption breaks down when particles on the nanometer scale are used to produce microscopic parts. In order to accurately capture the behavior of these powders, wave effects of the laser need to be considered and Maxwell's equations solved to predict how particles respond to laser heating.

Appendices

Appendix A

Terms and Definitions

α	Liquid Volume Fraction
α	Optical Absorptivity
α	Coefficient of Thermal Expansion
β	Extinction Coefficient
β	Volume Fraction of Solid
γ	Volume Fraction of Fluid
δ	Particle Overlap Distance
ϵ	Strain
ϵ	Momentum Sink Constant
ϵ	Emissivity
ϵ	Porosity
ζ	Arbitrary Material Property
$\zeta(\theta)$	Random Variable
θ	Angle
κ	Absorption Coefficient
λ	Lame's Parameter
λ	Laser Wavelength
μ	Mean
μ	Shear Modulus
ν	Poisson Ratio
ρ	Density
σ	Stress Tensor
σ_b	Stefan-Boltzman Constant
σ_s	Scattering Coefficient
σ_y	Yield Stress
τ	Fluid Stress Tensor
ϕ_j	Basis Polynomials
ω	Laser Characteristic Radius
Ω	Domain Boundary

A	Surface Area
a	Attenuation Coefficient
c	Specific Heat
CAD	Computer Aided Design
D_p	Particle Diameter
DEM	Discrete Element Method
E	Young's Modulus
F	Force
F	View Factor
F_s	Surface Tension Force
G	Irradiation Field
g	Gravitational Constant
g(T)	Melt Fraction
gPC	Generalized Polynomial Chaos
H	Enthalpy
I	Radiation Intensity
k	Thermal Conductivity
k	Spring Constant for DEM Spring-Dashpot Model
l_{cond}	Minimum Conduction Distance
L	Latent Heat
n	Normal
P	Laser Power
P	Pressure
PDF	Probability Density Function
PVA	Poly(vinyl alcohol)
$\dot{Q}$	Heat Flux
QoI	Quantity of Interest
R	Particle Radius
R_c	Particle Contact Radius
S	Mass Source
$\mathbf{s}$	Deviatoric of Stress Tensor
s	Direction
SLM	Selective Laser Melting
T	Temperature
t	Time
T_l	Liquidus Temperature
T_s	Solidus Temperature

T_{ref}	Reference Temperature
Ti-6Al-4V	Titanium Alloy
u	Fluid Velocity
u	Direction
u	Displacement
v	Speed
VOF	Volume of Fluid
$X(\theta)$	Quantity of Interest

Appendix B

OpenFOAM Implementation Details

B.1 Melt Model

The implementation of the particle-scale melt model is based on the OpenFOAM v3.0+ interFoam solver for multi-phase flow [43]. The OpenFOAM PIMPLE flow solver is modified to reflect the use of the porosity formulation of the Navier-Stokes equations. First, the formation of the momentum equation matrix is modified to include the coefficient γ, the volume fraction of a cell not occupied by solid, un-melted material.

```
//UEqn.H
//Porosity formulation of the momentum equation
dimensionedScalar odt = 1.0/runTime.deltaT();

surfaceScalarField muf = mixture.muf() *
fvc::interpolate(gamma);
fvVectorMatrix UEqn
(
fvm::ddt(gamma, rho, U) + fvm::div(rhoPhi, U)
- fvm::laplacian(muf, U)
+ fvm::Sp((1-gamma)*(1-gamma) /
max(gamma*gamma*gamma,1e-20)*rho*odt, U)
- (fvc::grad(U) & fvc::grad(muf))
);

UEqn.relax();
```

Next, the OpenFOAM PISO solver is modified to incorporate the γ coefficient into the solution of the pressure equation.

```
//pEqn.H
//Pressure correction modified for porosity formulation
volScalarField rAU("rAU", 1.0/UEqn.A());
surfaceScalarField rAUf("rAUf", fvc::interpolate(rAU));
surfaceScalarField gammaf
(
"gammaf",
fvc::interpolate(gamma)
);
surfaceScalarField gammaf2("gammaf2", gammaf * gammaf);

volVectorField HbyA("HbyA", U);
HbyA = rAU*UEqn.H();

surfaceScalarField phiHbyA
(
"phiHbyA",
(fvc::interpolate(HbyA) & mesh.Sf()) *
fvc::interpolate(gamma)
);

surfaceScalarField phig
(
(
surfaceTension * gammaf
- ghf*fvc::snGrad(rho) * gammaf2
)*rAUf*mesh.magSf()
);

phiHbyA += phig;

while (pimple.correctNonOrthogonal())
{
fvScalarMatrix p_rghEqn
```

```
(
fvm::laplacian(rAUf*gammaf2, p_rgh)
== fvc::div(phiHbyA)
);

p_rghEqn.setReference
(
pRefCell,
getRefCellValue(p_rgh,pRefCell)
);

p_rghEqn.solve
(
mesh.solver(p_rgh.select(pimple.finalInnerIter()))
);

if (pimple.finalNonOrthogonalIter())
{
phi = phiHbyA - p_rghEqn.flux();

U = HbyA + rAU*fvc::reconstruct
(
(
surfaceTension
- ghf*fvc::snGrad(rho) * gammaf
- fvc::snGrad(p_rgh) * gammaf
) * mesh.magSf()
);
U.correctBoundaryConditions();
}
}
```

The VOF solver routines are also modified to include cell porosity. The interFoam solver uses an implicit upwind predictor with an explicit flux corrector in order to propagate the volume fraction field while preserving a

sharp gas-liquid interface. First, the implicit predictor is modified to include the γ coefficient as well as a source term representing the conversion of material from solid to liquid due to melting and re-solidification.

```
//alphaEqn.H
//Modifications to upwind predictor
fvScalarMatrix alpha1Eqn
(
(
LTS
? fv::localEulerDdtScheme<scalar>(mesh).
fvmDdt(gamma, alpha1)
: fv::EulerDdtScheme<scalar>(mesh).
fvmDdt(gamma, alpha1)
)
+ fv::gaussConvectionScheme<scalar>
(
mesh,
phiCN,
upwind<scalar>(mesh, phiCN)
).fvmDiv(phiCN, alpha1) == alphaSource
);

alpha1Eqn.solve();
```

Next, the explicit correction is updated. interFoam uses the OpenFOAM MULES routine to accomplish the correction while bounding the resulting volume fraction field between 0 and 1. The γ field must be provided to the MULES routine.

```
//alphaEqn.H
//Modifications to the explicit corrector
tmp<surfaceScalarField> talphaPhiCorr(talphaPhiUn() -
alphaPhi);
volScalarField alpha10("alpha10", alpha1);
```

```
MULES::correct
(
gamma,
alpha1,
talphaPhiUn(),
talphaPhiCorr(),
zeroField(),
zeroField(),
1,
0
);

// Under-relax the correction for all
// but the 1st corrector
if (aCorr == 0)
{
alphaPhi += talphaPhiCorr();
}
else
{
alpha1 = 0.5*alpha1 + 0.5*alpha10;
alphaPhi += 0.5*talphaPhiCorr();
}
```

Finally, an new module is introduced in order to solve the energy equation. Effective properties are calculated for each cell depending on its volume fraction of solid, liquid and gas. Then, the radiation field is solved for using the OpenFOAM fvDOM module. Last, the enthalpy equation is solved iteratively until the temperature and enthalpy fields converge.

```
//HEqn.H
//Module to solve enthalpy formulation of energy equation
//in order to calculate temperature field
meltModel.calcKeff(keff);
```

```
meltModel.calcCpField(T,dhdT);

surfaceScalarField Tf = fvc::interpolate(hInverse);

meltModel.calcHf(Tf,alphaPhi,phi,Hf);
meltModel.calcCpf(Tf,alphaPhi,phi,dhdTf);
dimensionedScalar dt(runTime.deltaT());

solverPerformance sp;

radiation->correct();

for(int iter=0;iter<maxTIters;iter++)
{

T.storePrevIter();

fvScalarMatrix TEqn
(
fvm::Sp(dhdT/dt,T)
+ fvm::div(dhdTf,T)
+ fvc::div(Hf-dhdTf*fvc::interpolate(hInverse))
+ fvm::Su((H-dhdT*hInverse-H.oldTime())/dt,T)
- fvm::laplacian(keff,T)
==
enthVap
+ radiation->Ru()
- fvm::Sp(radiation->Rp()*pow3(T), T)
);

sp = TEqn.solve();

//update enthalpy field
H += dhdT*(T-hInverse);

//calculate hInverse
meltModel.findTField(H,hInverse);
```

```
//calculate dhdT
meltModel.calcCpField(hInverse,dhdT);
Tf = fvc::interpolate(hInverse);
meltModel.calcHf(Tf,alphaPhi,phi,Hf);
meltModel.calcCpf(Tf,alphaPhi,phi,dhdTf);

if(sp.initialResidual() <= TresidTol) break;
}
```

B.2 Thermo-mechanical Model

The enthalpy model implementation in OpenFOAM for the thermo-mechanical model is similar to that for the melting model. This implementation is simpler however, as it does not contain convective terms in the enthalpy equation and does not require a radiation transport equation solve. Radiation heat losses from the top surface of the powder bed are handled with a volumetric heat source which is split into implicit and explicit components to improve convergence. The volumetric laser heat source does not depend on temperature and so is calculated in advance.

```
meltModel.calcCpField();
meltModel.calcKeff();

dimensionedScalar dt(runTime.deltaT());

scalar residual = 1.0;
solverPerformance sp;

scalarField step(mesh.nCells(), 1.0);
volScalarField res
(
"residual",
```

```
(dhdT*T + H - dhdT*hInverse - H.oldTime())/dt -
fvc::laplacian(keff,T) - implicitHeatSource*T -
explicitHeatSource - laserHeatSource
);

for(int iter=0;iter<maxTIters;iter++)
{
T.storePrevIter();
H.storePrevIter();
res.storePrevIter();
laser.calculateRadHeatSources
(
explicitHeatSource,
implicitHeatSource
);

res =
(dhdT*T + H - dhdT*hInverse - H.oldTime())/dt
- fvc::laplacian(keff,T) - implicitHeatSource*T
- explicitHeatSource - laserHeatSource;

fvScalarMatrix TEqn
(
fvm::Sp(dhdT/dt,T)
+ fvm::Su((H-dhdT*hInverse-H.oldTime())/dt,T)
- fvm::laplacian(keff,T)
- fvm::Sp(implicitHeatSource,T)
==
explicitHeatSource
+ laserHeatSource
);

sp = TEqn.solve();

//decrease Newton step size if residual is not
//being reduced
forAll(res, celli)
```

```
{
if
(
mag(res[celli]) >=
mag(res.prevIter()[celli])
)
{
step[celli] = step[celli] * 0.5;
}
else
{
step[celli] = min
(
step[celli] * 2.0,
1.0
);
}
H[celli] += step[celli]*dhdT[celli]*
(T[celli]-hInverse[celli]);
}

meltModel.boundH();
meltModel.findTField();
meltModel.calcCpField();

residual = sp.initialResidual();

if((residual <= TresidTol) && iter >= 2)
{
T = hInverse;
break;
}
}
```

The mechanical solver is based on the FOAM-extend-3.1 elasticPlasticSolidFoam solver. The incremental form of the linear elastic relations are used

to calculate a trail stress. The main change is the inclusion of the thermal stress term and the temperature dependent material properties term. After the elastic trail stress is computed, the plastic model is called to update the plastic strain increment in cells which are yielding. The FOAM-extend-3.1 aravasMises plasticity stress return method is used for the plastic model.

```
int iCorr = 0;
Foam::SolverPerformance<Foam::vector > solverPerf;
scalar initialResidual = 1.0;
scalar relativeResidual = 1.0;
scalar plasticResidual = 1.0;

//calculate material properties
sModel.calculate();
threeK = E/(1.0 - 2.0*nu);
muf = fvc::interpolate(mu, "mu");
lambdaf = fvc::interpolate(lambda, "lambda");

//Thermal strain
const volScalarField& dT = sModel.dT();
DEpsilonT = alpha*dT;
//effects of temperature dependent
//material properties
DSigmaThermal =
(
2*dMudT*(epsilon - epsilonT*I - epsilonP) +
dLambdadT*I*tr(epsilon - epsilonT*I - epsilonP)
)*dT;

do
{
DU.storePrevIter();

fvVectorMatrix DUEqn
(
```

```
rho*fvm::d2dt2(DU)
==
fvm::laplacian
(
2*muf + lambdaf,
DU,
"laplacian(DDU,DU)"
)
+ fvc::div
(
mu*gradDU.T() + lambda*(I*tr(gradDU))
- (mu + lambda)*gradDU - threeK*DEpsilonT*I,
"div(sigma)"
)
+ fvc::div(DSigmaThermal, "div(sigma)")
- fvc::div(2*muf*(mesh.Sf()
& fvc::interpolate(DEpsilonP)))
);

solverPerf = DUEqn.solve();

if (iCorr == 0)
{
initialResidual =
solverPerf.max().initialResidual();
}

DU.relax();

gradDU = fvc::grad(DU);

#include "calculateRelativeResidual.H"
#include "calculateDEpsilonDSigma.H"

// correct plastic strain increment
plasticModel.correct();
```

```
#include "calculatePlasticResidual.H"
}
while
(
iCorr++ < 2
||
solverPerf.max().initialResidual() >
convergenceTolerance
);

// Update total quantities
U += DU;
epsilon += DEpsilon;
epsilonP += plasticModel.DEpsilonP();
sigma += DSigma;
epsilonT += DEpsilonT;
```

Bibliography

[1] B. M. Adams, M. S. Ebeida, M. S. Eldred, G. Geraci, J. D. Jakeman, K. A. Maupin, J. A. Monschke, L. P. Swiler, J. A. Stephens, D. M. Vigil, and T. M. Wildey. Dakota, A Multilevel Parallel Object-Oriented Framework for Design Optimization, Parameter Estimation, Uncertainty Quantification, and Sensitivity Analysis: Version 6.6 Theory Manual, 2017.

[2] ANSYS. ANSYS Fluent Theory Guide. 15, 2013.

[3] K. Bala, P. R. Pradhan, N. S. Saxena, and M. P. Saksena. Effective thermal conductivity of copper powders. *Journal of Physics D: Applied Physics*, 22(8):1068, 1989.

[4] G. K. Batchelor and R. W. O'Brien. Thermal or Electrical Conduction Through a Granular Material. *Proceedings of the Royal Society of London. A. Mathematical and Physical Sciences*, 355(1682):313–333, jul 1977.

[5] M. Boivineau, C. Cagran, D. Doytier, V. Eyraud, M. H. Nadal, B. Wilthan, and G. Pottlacher. Thermophysical Properties of Solid and Liquid Ti-6Al-4V (TA6V) Alloy. *International Journal of Thermophysics*, 27(2):507–529, 2006.

[6] R. Borja. *Plasticity Modeling & Computation*. Springer-Verlag, New York, NY, 2013.

[7] G. B. M. Cervera and G. Lombera. Numerical prediction of temperature and density distributions in selective laser sintering processes. *Rapid Prototyping Journal*, 5(1):21–26, 1999.

[8] J. C. Chen and S. W. Churchill. Radiant heat transfer in packed beds. *AIChE Journal*, 9(1):35–41, 1963.

[9] S. C. Cheng and R. I. Vachon. Thermal conductivity of packed beds and powder beds. *International Journal of Heat and Mass Transfer*, 12(9):1201–1206, sep 1969.

[10] R. Coquard and D. Baillis. Radiative Characteristics of Opaque Spherical Particles Beds: A New Method of Prediction. *Journal of Thermophysics and Heat Transfer*, 18(2):178–186, apr 2004.

[11] L. Dong, A. Makradi, S. Ahzi, and Y. Remond. Three-dimensional transient finite element analysis of the selective laser sintering process. *Journal of Materials Processing Technology*, 209(2):700–706, jan 2009.

[12] Y. Feng, K. Han, C. Li, and D. Owen. Discrete thermal element modelling of heat conduction in particle systems: Basic formulations. *Journal of Computational Physics*, 227(10):5072–5089, may 2008.

[13] C. Finch, editor. *Polyvinyl alcohol : developments*. Wiley, Chichester, New York, 1992.

[14] A. Foroozmehr, M. Badrossamay, E. Foroozmehr, and S. Golabi. Finite Element Simulation of Selective Laser Melting process considering Optical Penetration Depth of laser in powder bed. *Materials & Design*, 89:255–263, 2016.

[15] W. E. Frazier. Metal Additive Manufacturing: A Review. *Journal of Materials Engineering and Performance*, 23(6):1917–1928, 2014.

[16] B. Ganapathysubramanian and N. Zabaras. Sparse grid collocation schemes for stochastic natural convection problems. *Journal of Computational Physics*, 225(1):652–685, jul 2007.

[17] R. Garg, J. Galvin, T. Li, and S. Pannala. Documentation of open-source MFIXDEM software for gas-solids ows, 2012.

[18] A. S. Glassner, editor. *An Introduction to Ray Tracing*. Academic Press Ltd., London, UK, UK, 1989.

[19] H. Gong, H. Gu, K. Zeng, J. Dilip, D. Pal, B. Stucker, D. Christiansen, J. Beuth, and J. J. Lewandowski. Melt Pool Characterization for Selective Laser Melting of Ti-6Al-4V Pre-alloyed Powder. In *Solid Freeform Fabrication Proceedings*, pages 256–267, 2014.

[20] F.-J. Gürtler, M. Karg, K.-H. Leitz, and M. Schmidt. Simulation of Laser Beam Melting of Steel Powders using the Three-Dimensional Volume of Fluid Method. *Physics Procedia*, 41:881–886, 2013.

[21] A. V. Gusarov, T. Laoui, L. Froyen, and V. I. Titov. Contact thermal conductivity of a powder bed in selective laser sintering. *International Journal of Heat and Mass Transfer*, 46(6):1103–1109, mar 2003.

[22] A. V. Gusarov, I. Yadroitsev, P. Bertrand, and I. Smurov. Model of Radiation and Heat Transfer in Laser-Powder Interaction Zone at Selective Laser Melting. *Journal of Heat Transfer*, 131(7):72101, may 2009.

[23] N. E. Hodge, R. M. Ferencz, and J. M. Solberg. Implementation of a thermomechanical model for the simulation of selective laser melting. *Computational Mechanics*, 54(1):33–51, 2014.

[24] M. Hunt. PRISM Uncertainty Quantification Documentation, 2014.

[25] N. Iqbal and C. Rauh. Coupling of discrete element model (DEM) with computational fluid mechanics (CFD): A validation study. *Applied Mathematics and Computation*, 277:154–163, 2016.

[26] K. Kamiuto and S. San Yee. Correlated radiative transfer through a packed bed of opaque spheres. *International Communications in Heat and Mass Transfer*, 32(12):133–139, jan 2005.

[27] S. A. Khairallah and A. Anderson. Mesoscopic simulation model of selective laser melting of stainless steel powder. *Journal of Materials Processing Technology*, 214(11):2627–2636, 2014.

[28] S. A. Khairallah, A. T. Anderson, A. Rubenchik, and W. E. King. Laser powder-bed fusion additive manufacturing: Physics of complex melt flow

and formation mechanisms of pores, spatter, and denudation zones. *Acta Materialia*, 108:36–45, 2016.

[29] W. E. King, A. T. Anderson, R. M. Ferencz, N. E. Hodge, C. Kamath, S. A. Khairallah, and A. M. Rubenchik. Laser powder bed fusion additive manufacturing of metals; physics, computational, and materials challenges. *Applied Physics Reviews*, 2(4):41304, dec 2015.

[30] S. Kolossov, E. Boillat, R. Glardon, P. Fischer, and M. Locher. 3D FE simulation for temperature evolution in the selective laser sintering process. *International Journal of Machine Tools and Manufacture*, 44(23):117–123, feb 2004.

[31] C. Körner, E. Attar, and P. Heinl. Mesoscopic simulation of selective beam melting processes. *Journal of Materials Processing Technology*, 211(6):978–987, 2011.

[32] C. Li, C. H. Fu, Y. B. Guo, and F. Z. Fang. A multiscale modeling approach for fast prediction of part distortion in selective laser melting. *Journal of Materials Processing Technology*, 229:703–712, mar 2016.

[33] J. E. Mark, editor. *Physical Properties of Polymers Handbook*. New York, 2 edition, 2007.

[34] G. Marsaglia. Choosing a Point from the Surface of a Sphere. *The Annals of Mathematical Statistics*, 43(2):645–646 CR – Copyright © 1972 Institute of Ma, apr 1972.

[35] S. Masamune and J. M. Smith. Thermal Conductivity of Beds of Spherical Particles. *Industrial & Engineering Chemistry Fundamentals*, 2(2):136–143, may 1963.

[36] P. Mercelis and J. Kruth. Residual stresses in selective laser sintering and selective laser melting. *Rapid Prototyping Journal*, 12(5):254–265, oct 2006.

[37] D. Moser, S. Fish, J. Beaman, and J. Y. Murthy. Multi-Layer Computational Modeling of Selective Laser Sintering Processes. In *Proceedings of the ASME 2014 International Mechanical Engineering Congress & Exposition*.

[38] D. Moser, S. Pannala, and J. Murthy. Computation of Effective Thermal Conductivity of Powders for Selective Laser Sintering Simulations. *Journal of Heat Transfer*, 138(8):82002, may 2016.

[39] J. Y. Murthy and S. R. Mathur. Finite Volume Method for Radiative Heat Transfer Using Unstructured Meshes. *Journal of Thermophysics and Heat Transfer*, 12(3):313–321, jul 1998.

[40] J. M. H. Musser. *Modeling of Heat Transfer and Reactive Chemistry for Particles in Gas-Solid Flow Utilizing Continuum-Discrete Methodology (CDM)*. PhD thesis, West Virginia University, 2011.

[41] M. Negahban. *The Mechanical and Thermodynamical Theory of Plasticity*. Boca Raton, FL, 1 edition, 2012.

[42] J. C. Nelson, S. Xue, J. W. Barlow, J. J. Beaman, H. L. Marcus, and D. L. Bourell. Model of the selective laser sintering of bisphenol-A polycarbonate. *Industrial & Engineering Chemistry Research*, 32(10):2305–2317, oct 1993.

[43] OpenFOAM Foundation. OpenFOAM User Guide, 2016.

[44] B. Partee, S. J. Hollister, and S. Das. Selective Laser Sintering Process Optimization for Layered Manufacturing of CAPA® 6501 Polycaprolactone Bone Tissue Engineering Scaffolds. *Journal of Manufacturing Science and Engineering*, 128(2):531–540, sep 2005.

[45] R. B. Patil and V. Yadava. Finite element analysis of temperature distribution in single metallic powder layer during metal laser sintering. *International Journal of Machine Tools and Manufacture*, 47(78):1069–1080, jun 2007.

[46] M. J. D. Powell. An efficient method for finding the minimum of a function of several variables without calculating derivatives. *The Computer Journal*, 7(2):155–162, jan 1964.

[47] W. H. Press, B. P. Flannery, S. A. Teukolsky, and W. T. Vetterling. *Numerical Recipes in C: The Art of Scientific Computing*. 2 edition, 1992.

[48] D. Rong and M. Horio. DEM simulation of char combustion in a fluidized bed. In *Second Internation Conference on CFD in the Minerals and*

Process Industries, pages 65–70, Melbourne, 1999.

[49] W. Shyy, M. Garbey, A. Appukuttan, and J. Wu. Evaluation of Richardson Extrapolation in Computational Fluid Dynamics. *Numerical Heat Transfer, Part B: Fundamentals*, 41(2):139–164, feb 2002.

[50] S. S. Sih. *The thermal and optical properties of powders in selective laser sintering*. PhD thesis, Ann Arbor, 1996.

[51] A. Singh and R. S. Prakash. Response surface-based simulation modeling for selective laser sintering process. *Rapid Prototyping Journal*, 16(6):441–449, 2010.

[52] B. P. Singh and M. Kaviany. Modelling radiative heat transfer in packed beds. *International Journal of Heat and Mass Transfer*, 35(6):1397–1405, jun 1992.

[53] A. J. Slavin, V. Arcas, C. A. Greenhalgh, E. R. Irvine, and D. B. Marshall. Theoretical model for the thermal conductivity of a packed bed of solid spheroids in the presence of a static gas, with no adjustable parameters except at low pressure and temperature. *International Journal of Heat and Mass Transfer*, 45(20):4151–4161, sep 2002.

[54] A. J. Slavin, F. A. Londry, and J. Harrison. A new model for the effective thermal conductivity of packed beds of solid spheroids: alumina in helium between 100 and 500C. *International Journal of Heat and Mass Transfer*, 43(12):2059–2073, jun 2000.

[55] S. A. Smolyak. Quadrature and interpolation formulas for tensor products of certain classes of functions. *Soviet Mathematics, Doklady*, 4:240–243, 1963.

[56] T. G. Spears and S. A. Gold. In-process sensing in selective laser melting (SLM) additive manufacturing. *Integrating Materials and Manufacturing Innovation*, 5(1):2, 2016.

[57] M.-s. M. Sun and J. J. Beaman. A Three Dimensional Model for Selective Laser Sintering. In *Proceedings of Solid Freeform Fabrication Symposium*, pages 102–109, Austin, TX, 1991.

[58] S. Sun, L. Zheng, Y. Liu, J. Liu, and H. Zhang. Selective laser melting of Al-Fe-V-Si heat-resistant aluminum alloy powder: modeling and experiments. *The International Journal of Advanced Manufacturing Technology*, 80(9):1787–1797, 2015.

[59] X. Sun and M. Sakai. Three-dimensional simulation of gassolidliquid flows using the DEMVOF method. *Chemical Engineering Science*, 134:531–548, sep 2015.

[60] C. R. Swaminathan and V. R. Voller. A general enthalpy method for modeling solidification processes. *Metallurgical Transactions B*, 23(5):651–664, 1992.

[61] A. E. Tontowi and T. Childs. Density prediction of crystalline polymer sintered parts at various powder bed temperatures. *Rapid Prototyping*

Journal, 7(3):180–184, 2001.

[62] T. Tsory, N. Ben-Jacob, T. Brosh, and A. Levy. Thermal DEMCFD modeling and simulation of heat transfer through packed bed. *Powder Technology*, 244:52–60, aug 2013.

[63] W. van Antwerpen, C. G. du Toit, and P. G. Rousseau. A review of correlations to model the packing structure and effective thermal conductivity in packed beds of mono-sized spherical particles. *Nuclear Engineering and Design*, 240(7):1803–1818, jul 2010.

[64] W. L. Vargas and J. J. McCarthy. Conductivity of granular media with stagnant interstitial fluids via thermal particle dynamics simulation. *International Journal of Heat and Mass Transfer*, 45(24):4847–4856, nov 2002.

[65] G. Widenfeld, Y. Weiss, and H. Kalman. The effect of compression and preconsolidation on the effective thermal conductivity of particulate beds. *Powder Technology*, 133(1-3):15–22, jul 2003.

[66] J. D. Williams and C. R. Deckard. Advances in modeling the effects of selected parameters on the SLS process. *Rapid Prototyping Journal*, 4(2):90–100, 1998.

[67] F. E. Wiria, K. F. Leong, and C. K. Chua. Modeling of powder particle heat transfer process in selective laser sintering for fabricating tissue engineering scaffolds. *Rapid Prototyping Journal*, 16(6):400–410, 2010.

[68] D. Xiu and J. Hesthaven. High-Order Collocation Methods for Differential Equations with Random Inputs. *SIAM Journal on Scientific Computing*, 27(3):1118–1139, jan 2005.

[69] D. Xiu and G. Karniadakis. The Wiener–Askey Polynomial Chaos for Stochastic Differential Equations. *SIAM Journal on Scientific Computing*, 24(2):619–644, jan 2002.

[70] D. Xiu and G. E. Karniadakis. A new stochastic approach to transient heat conduction modeling with uncertainty. *International Journal of Heat and Mass Transfer*, 46(24):4681–4693, nov 2003.

[71] S. Xue and J. W. Barlow. Thermal Properties of Powders. In *Solid Freeform Fabrication Proceedings*, pages 179–185, Austin, TX, 1990.

[72] S. Xue and J. W. Barlow. Models for the Prediction of the Thermal Conductivities of Powders. In *Solid Freeform Fabrication Proceedings*, pages 62–69, Austin, TX, 1991.

[73] I. Yadroitsava and I. Yadroitsev. Residual Stress in Metal Specimens Produced by Direct Metal Laser Sintering. In *Proceedings of Solid Freeform Fabrication Symposium*, pages 614–626, 2015.

[74] Y. S. Yang. *Heat Transfer Through a Randomly Packed Bed of Spheres by the Monte Carlo Method.* PhD thesis, Ann Arbor, 1981.

[75] M. Yuan, T. T. Diller, D. Bourell, and J. Beaman. Thermal conductivity of polyamide 12 powder for use in laser sintering. *Rapid Prototyping Journal*, 19(6):437–445, 2013.

[76] M. F. Zaeh and G. Branner. Investigations on residual stresses and deformations in selective laser melting. *Production Engineering*, 4(1):35–45, 2010.

[77] K. Zeng, D. Pal, H. Gong, N. Patil, and B. Stucker. Comparison of 3DSIM thermal modelling of selective laser melting using new dynamic meshing method to ANSYS. *Materials Science and Technology*, 31(8):945–956, 2015.

[78] H. Zhang, Q. Zhou, H. Xing, and H. Muhlhaus. A DEM study on the effective thermal conductivity of granular assemblies. *Powder Technology*, 205(1-3):172–183, jan 2011.

[79] J. Zhou, Y. Zhang, and J. K. Chen. Numerical simulation of laser irradiation to a randomly packed bimodal powder bed. *International Journal of Heat and Mass Transfer*, 52(1314):3137–3146, jun 2009.